February 2021

**Ph.D. Dissertation**

# Synthesis and Applications of Sequential Dip-Coating Processed Perovskite Materials

**Graduate School of Chosun University**

**Department of Chemistry**

**Muhammad Adnan**

# Synthesis and Applications of Sequential Dip-Coating Processed Perovskite Materials

## 연속딥코팅 공정을 이용한 페로브스카이트 재료의 합성과 응용

**February 25, 2021**

**Graduate School of Chosun University**

**Department of Chemistry**

**Muhammad Adnan**

# Synthesis and Applications of Sequential Dip-Coating Processed Perovskite Materials

**Advisor: Prof. Jae Kwan Lee**

*This dissertation is submitted to the Graduate School of Chosun University in partial fulfillment of the requirements for the degree of Doctor of Philosophy in Science*

**October 2020**

**Graduate School of Chosun University**

**Department of Chemistry**

**Muhammad Adnan**

**This is to certify that the Ph.D. dissertation of Muhammad Adnan has successfully met the dissertation requirements of Chosun University.**

위원장 조선대학교 교수 손 홍 래 (인)

위 원 조선대학교 교수 고 문 주 (인)

위 원 조선대학교 교수 김 호 중 (인)

위 원 조선대학교 교수 이 재 관 (인)

위 원 전남대학교 교수 조 성 (인)

**December 2020**

**Graduate School of Chosun University**

# CONTENTS

# ABBREVIATIONS

PV: Photovoltaic PCE: power conversion efficiency

VOC: Open-circuit voltage JSC short-circuit current density

FF: Fill factor DSSC: dye-sensitized solar cell

ETL: Electron-transporting layer

HTL: Hole-transporting layer

MA: Methylammonium

FA: Formamidinium

FTO: Fluorine-doped tin oxide NC: nanocrystal

HTM: Hole-transporting material

FWHM: Full width at half maximum

PL: Photoluminescence

DMF: N,N-dimethylformamide

DMSO: Dimethyl sulfoxide

CB: Conduction band

VB: Valence band

XRD: X-ray diffraction

AFM: Atomic force microscopy

TEM: Transmission electron microscopy

XPS: X-ray photoelectron spectroscopy

EF: Fermi level

Eg: Band-gap

q: Elementary charge

τ: Carrier lifetime

WSC: Width of space charge region

Rs: Series resistance

R rec: Recombination resistance

# LIST OF FIGURES

**CHAPTER 1**

**CHAPTER 2**



**CHAPTER 3**

# Abstract

## Synthesis and Applications of Sequential Dip Coated Processed Perovskite Materials

Muhammad Adnan

Advisor: Prof Jae Kwan Lee

Department of Chemistry

Graduate School of Chosun University

Recently, organic-inorganic lead halide perovskite solar cells (PrSCs) have received intense attention from the scientific community because of their marvelous breakthrough power conversion efficiencies (PCEs), making them propitious to conventional silicon-based solar cells. Hence, an intense research has been devoted for the development of an efficient fabrication methods for perovskite material layers in PrSCs research. In principally, the crystallinity, the surface coverages and uniformity of perovskite materials, particularly alkylammonium lead halide ($RNH_3$)$PbX_3$ (R= alkyl, X= Cl, Br, I), on the substrate are censorious for boosting the PCEs of the PrSCs devices. But, the fabricated PrSCs frequently possessed small active areas and suffered from the substrate size limitation by the spin-casting technique. Herein, we will present a facile, cost effective and environmentally benign approach to prepare efficient perovskite materials by simple dip-coating deposition. This study will readily demonstrate by all sequentially dipping of a ZnO covered $TiO_2$ film in an aqueous Pb precursor solution and then in MAI or mixed halide MAI/MACl solution. This process is in contrast to the conventional spin-casting approach with detrimental organic solvents such as DMSO and DMF. We suspect that the perovskite

materials fabricated from this process will exhibit a superior crystallinity, morphology and surface coverages even in large surface area substrates, which might be a step forward towards the commercialization of PrSCs materials. Also, the $MAPbI_3$ or any other mixed halide perovskites formed by a $Pb(NO_3)_2$ and $PbI_2$ may undergoes additional ion-exchange reactions with un-reacted $Pb(NO_3)_2$, even in the solid state, resulting in decomposition into the $PbI_2$. We hope that by controlling all sequential dipping conditions, we will achieve a notable PCE for the PrSCs fabricated by using an aqueous halide-free lead precursor solution without spin-coating process, ensuring an environmentally friendly and low-cost manufacturing processes.

# 초록

## 연속딥코팅 공정을 이용한 페로브스카이트 재료의 합성과 응용

박사과정: 무 하 마 드 아 드 난

지도교수: 이 재 관

조 선 대 학 교 화 학 교 육

최근, 유기-무기 혼성 할로젠화 납 페로브스카이트 태양전지가 기존의 실리콘태양전지에 버금가는 광전변환효율을 보여주면서 많은 주목을 받고 있다. 이런 효율은 페로브스카이트 태양전지 연구에서 보다 우수한 페로브스카이트 재료 박막을 형성하는 효과적인 제조방법을 통해 구현될 수 있었으며, 주로 페로브스카이트 재료의 결정성, 표면 커버리지와 균일성을 조절하고, 제어함으로써 디바이스 성능을 향상시켜 왔다. 특히 alkylammonium lead halide $(RNH_3)PbX_3$ (R= alkyl, X= Cl, Br, I)는 페로브스카이트의 효율을 향상시키는 주요 재료로 활용되고 있다. 그러나, 현재 페로브스카이트 재료 박막형성 방법은 스핀-코팅법이 적용되고 있으며, 균일하고 우수한 박막층을 제조하는데 효과적이지만, 제한적인 기판크기로 인해 상용화기술에 난점을 나타낸다. 또한, $(RNH_3)PbX_3$을 합성하기 위해 $PbX_2$ 전구체를 이용하는데, 일반적인 유기용매에 난용성을 가지고 있어, DMSO나 DMF와 같은 인체 유해하고 독성이 있는 용매를 사용해야만 하는 문제점을 가지고 있다. 본 학위 논문에서는 이러한 문제점들을 극복하기위해 보다 쉽고, 효과적인 딥-코팅 흡착공정을 적용해 페로브스카이트 재료 박막을 형성시키고자 하였고, 유기용매 대신 물을 사용하여 보다 환경친화적인 재료합성을 수행하였다. 물에 녹는 납 전구체로 $Pb(NO_3)_2$를 이용하였으며, ZnO

표면에 전구체의 딥코칭 흡착이 성공적으로 이루어졌다. 이를 통해 결정성이 높고, 표면 커버리지가 높은 $(RNH_3)PbX_3$ 페로브스카이트 재료 박막을 합성할 수 있었다. 이러한 연구 과정에서 Successive Solid-state Ion-Exchange and Reaction (SSIER)의 새로운 개념을 제안할 수 있었으며, 이를 적용하여 대면적의 페로브스카이트 재료 박막 합성 및 고효율의 페로브스카이트 태양전지를 구현할 수 있었다.

# Chapter 1 – Introduction

## *Background*

### 1.1 Energy

Energy is the backbone for the survival of human civilization in this planet. The energy consumption and its need are growing day by day and is closely correlated with the progress of human development. The energy requires to consume per capita can quantitatively define the expansion of population in terms of technology.

This energy depletion includes total energy exploit by every energy origin from every technological sector across the globe accept energy utilize from food and directly from biomass burning [1-2]. But the demanding part is that with the progress of human advancement there is a rapid increase in need for various energy sources. Majority of non-sustainable energy sectors (such as oil, natural gas, coal etc.) have limited capacity. Furthermore, few of them have a serious hazardous effect on environment. So, there is a continuous search for suitable energy sources which are sustainable and are environmentally friendly. Renewable energy sources could be an alternate solution for this issue although, the generation costs of energy from these provenances are still much higher.

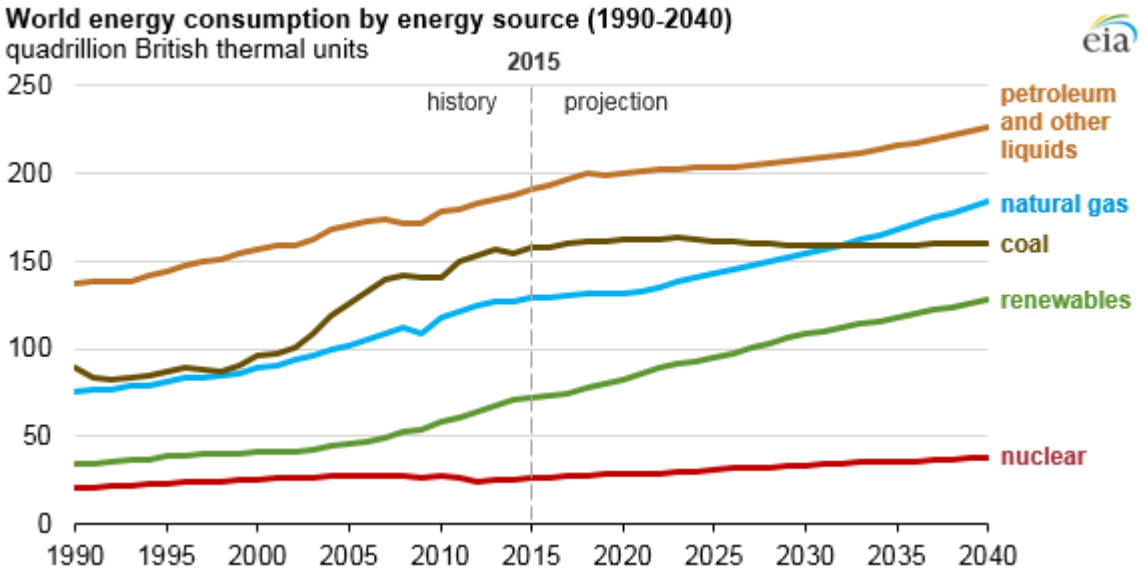


**Figure 1:** Worlds energy consumption map

### 1.2 Renewable Energy

Renewable energy is the latest hot issue for the globe and is obtained from various renewable energy resources such as wind, sun-light, tides, waves, geothermal heat etc. [3]. These

renewable energy sources considered most sustainable and are environmentally friendly. Renewable sources have potential to provide long-term energy solutions in the future. In 2012, the renewable energy sources produced just 19% of the world's total energy consumption, and rest of 81% was coming from combination of non-renewable sources such as petroleum, coal, natural gas and nuclear energy.

The main purpose to get energy from these non-renewable sources is the ease of getting energy from these sources. More to that these sources could be stored for long terms and can be shipped from one place to another with any type of transportation. But majority of these sources are proved hazardous and are not environmentally friendly. For instance, burning coal produces many toxic gases and pollutants in to the atmosphere. Coal mining is also considered one of the most dangerous job in the world and have already caused very serious accidents [4]. Importantly, these non-renewable sources are depleting day by day very rapidly and are very limited and there is a threat that these will be finished soon. Therefore, the search for renewable energy sources are getting great attention, now a days.

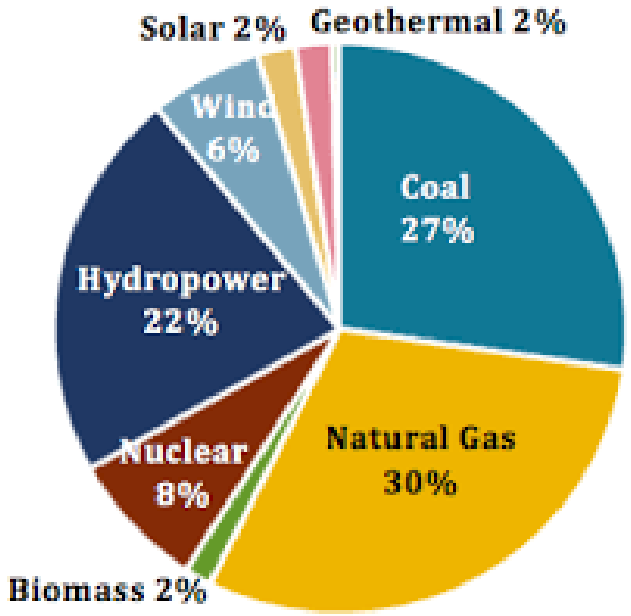


**Figure 2:** Renewable energy consumption report

In our universe, we have a plenty of renewable energy sources such as wind, sunlight, tides, waves, geothermal heat etc. Because of this, there is a rapid increase in search for more and more renewable energy sources [5]. In the past decades, hydro and wind sources are the hottest ones and these are dominatingly used as compared to others, but, due to rapidly increasing

demand of energy scientist now moving to solar PVs also to overcome the world's energy crises.

### 1.3 Solar Energy

The source of solar energy came from sun via the electromagnetic rays. It is important to know that only a very small fraction of solar energy arrives to the earth from sun, but, that is enough to fulfill the all energy need of this globe. Solar energy is considered as one of the most promising sources of renewable energy and have already showed its worth to be a great prime source of energy in the future. The solar energy has the following various advantages:

- Solar energy is abundant in nature.
- Solae energy is mostly environmentally friendly.
- The production and continuation cost of solar panels is very low as compared with other technologies.
- This technology can have almost no noise pollution.
- It provides a very reliable source of energy.
- Solar power also provides energy security.
- Solar energy is also considered as a most durable and convenient source of energy.

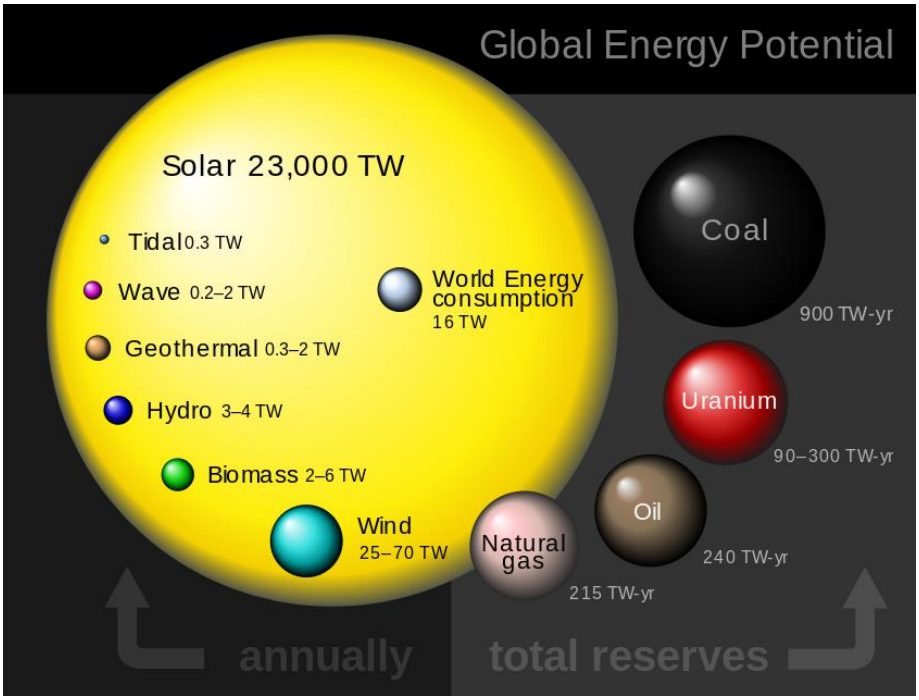


**Figure 3:** Global energy potential

The possible maximum potential of solar energy has been shown in figure 3. The possible power that could be generated from solar energy is about 2300 TW/year that is very high as compared to any other sources of energy. The consumption history of mankind shows that we consume around 16 TW/year. Therefore, there is a specific need to get more and more power from the sun to fulfill the basic needs of mankind. It is estimated that around 76% of total energy was mainly originating from various non-renewable energy sources, while, the rest 24% was coming from various renewable energy sources. And from this 24% which came from renewable energy sources, we can sum up that only about 1.2% was primarily obtained from solar modules [6-7].

Therefore, it is well realized that Solar PV is the future of clean and renewable energy and has tremendous potential to meet with the global energy consumption, but there is couple of hurdles to operate Solar PV as the primary source of energy. The possible reason for this is high cost and lower PCE, this lower PCE is a threat to increase the cost per unit area as compared with other different energy sources [8].

For a provided solar module, the electricity producing power of a solar panel mainly depends on the materials overall PCE and the surface area of the module. Because of this, the panels with lower PCE needs larger surface areas to meet up with the requirements. Such type of solar modules considered most expensive and is not the interested ones for the society. There may also be a hurdle in producing demanding power from the solar panels is the cloudy environment where panels unable to receive enough power from sun to convert that into electricity. Therefore, a sufficient source of storage is required to overcome such type of problems for the bad days and the production of highly smart solar panels is the main requirement of the system.

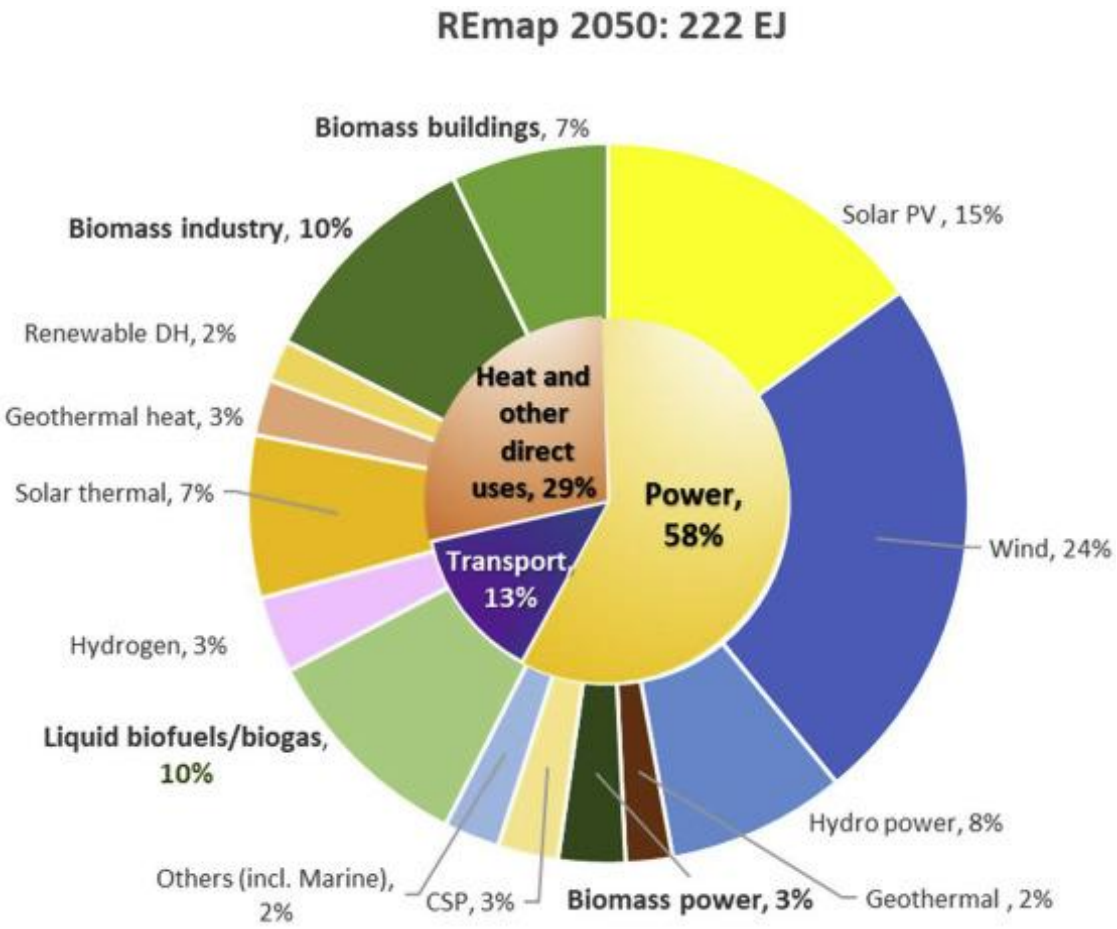


**Figure 4**: Renewable energy share from renewable sources in global energy consumption in 2020

But the encouraging sign for Solar PV is that the cost per unit power is going down exponentially over the years (Figure 4) [9]. Figure 4 presented the comparison of solar technology with others and convinced us that if move on with this research by 2030 then we can assume that the future is on the shoulders of solar photovoltaics due to their outstanding results, best fitted for the economy and the environment, respectively.

### 1.4 Photovoltaics

The development required to convert solar power into electric power is known as photovoltaics. This approach could not be completed without the employment of various SCs panels [10]. This phenomenon is the main backbone of solar power generation. Importantly, people (Bell lab) get started this phenomenon in 19$^{th}$ century by developing a first solar device in early 1950s. It has seen a real boost in R&D of photovoltaics technology, mainly in space

applications. But, such type of panels has several draw backs and also quite expensive. SCs research for silicon-based photovoltaics got a great attention in 1980s and scientists abled to produce above 20% PCE of the devices. Afterwards, an intense research has been devoted for thin films and multi-junction SCs and their demand increasing day by day because of their promising advantages for the solar cells industry [11].

### 1.5 Solar cell overview

A solar cell is a device which can convert solar energy directly into electricity. Since the first discovery of the photovoltaic (PV) act by Edmond Becquerel in 1839 [12] and the first production of a 6% crystalline silicon solar cell by Chapin et al. in 1954 [13], this technology has been greatly developed. Now crystalline silicon-based PV technology is very mature and widely commercialized. By the end of 2016, the global installed PV power capacity has increased to 315GW, and is predicted to double by 2019 [14]. The development of solar cell technology has gone through three stages, which are known as three generations, as shown in figure 5.

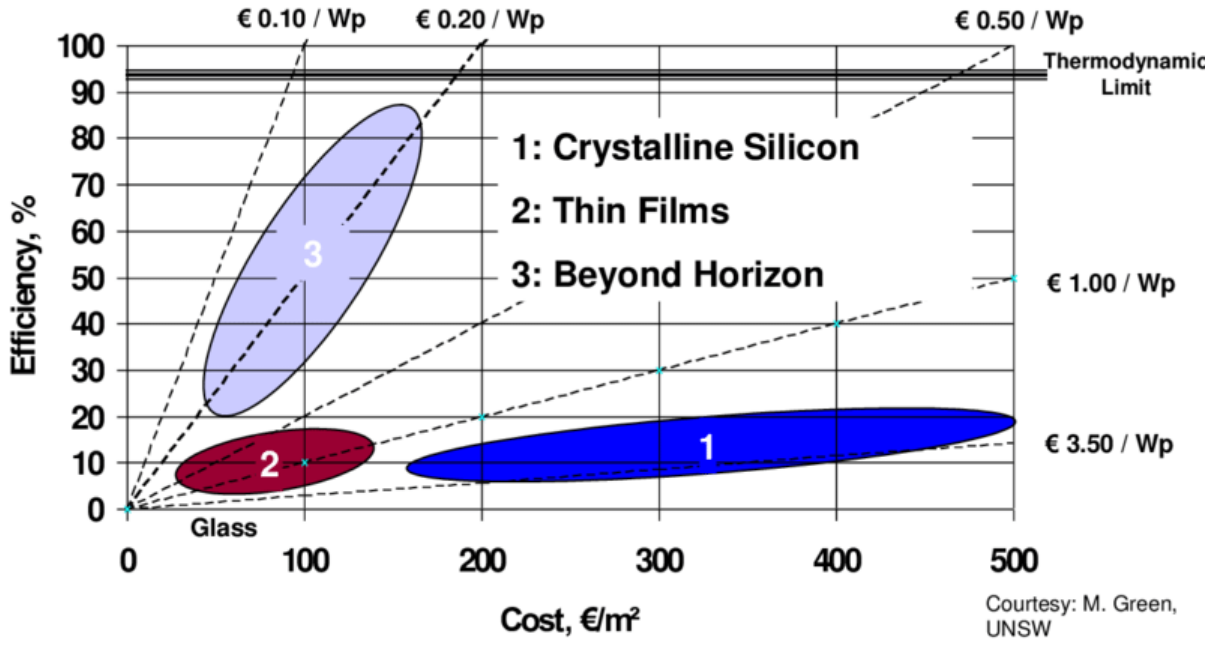


**Figure 5**: Diagram depicting the solar cells efficiencies and costs for three generations of PV technologies

### 1.5.1 First generation solar cells

Traditional solar cells are made from silicon, are presently the utmost desirable SCs available for the commercial use and account for around 80% of solar panels being sold in the world. Generally, silicon-based SCs are highly effective and long-lasting than non-silicon-based cells. However, they are more at risk to lose some of their efficiency at higher temperatures (hot sunny days), than thin-film solar cells [16-18].

For commercial purposes, there are four various kinds of silicon-based panel are being used. Mainly, such type of panels is based on the type of silicon incorporated there.

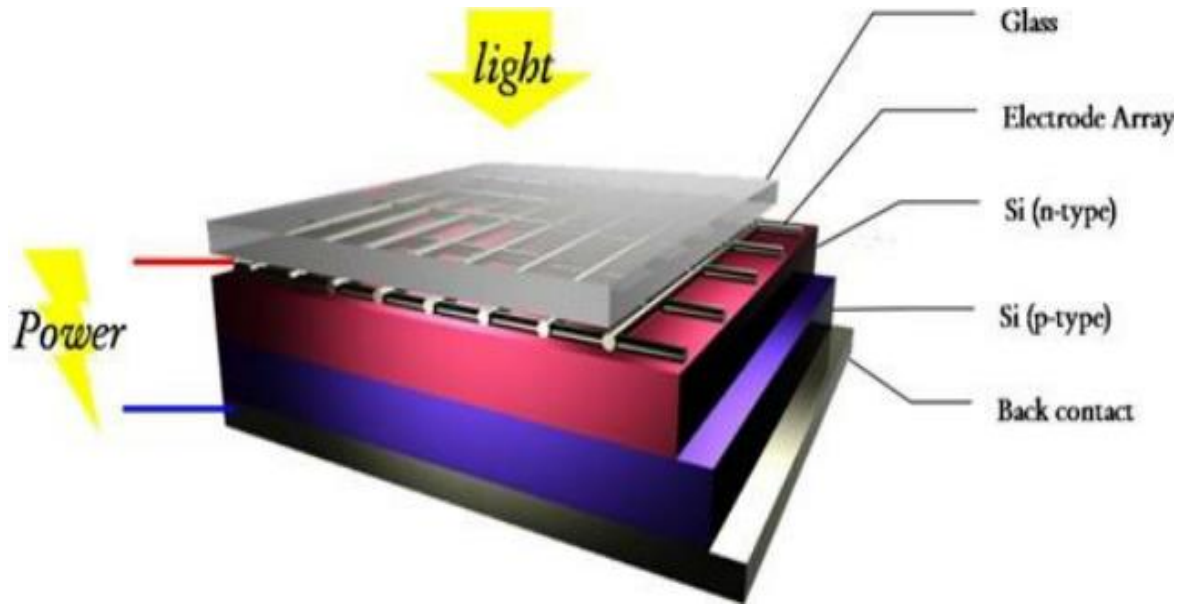


**Figure 6**: Schematic diagram of first-generation solar cells

#### 1.5.1.1 Monocrystalline silicon cells

The oldest solar cell technology and still the most popular and efficient are solar cells made from thin wafers of silicon. These are called monocrystalline solar cells because the cells are sliced from large single crystals that have been painstakingly grown under carefully controlled conditions. Typically, the cells are a few inches across, and a number of cells are laid out in a grid to create a panel.

Relative to the other types of cells, they presented an efficient PCE (up to 24.2%), meaning you will obtain more electricity from a given area of panel. This is useful if you only have a limited area for mounting your panels, or want to keep the installation small for aesthetic reasons. However, growing large crystals of pure silicon is a difficult and very energy-intensive process, so the production costs for this type of panel have historically are the highest of all the solar panel types.

Production methods have improved though, and prices for raw silicon as well as to build panels from monocrystalline solar cells have fallen a great deal over the years, partly driven by competition as other types of panel have been produced.

Another issue to keep in mind about panels made from monocrystalline silicon cells is that they lose their efficiency as the temperature increases about 25˚C, so they need to be installed in such a way as to permit the air to circulate over and under the panels to improve their efficiency.

#### 1.5.1.2 Polycrystalline solar cells

It is quite inexpensive to produce silicon-wafers in molds from multi-silicon crystals rather than from a single crystal as the conditions for growth do not need to be as tightly controlled. In this form, a number of interlocking silicon crystals grow together. Panels based on these cells are cheaper per unit area than monocrystalline panels - but they are also somewhat less competent (up to 19.3%).

#### 1.5.1.3 Amorphous silicon cells

You probably never thought about it before, but most solar cells used in calculators and many small electronic devices are made from amorphous silicon cells.

Instead of growing silicon crystals as is done in making the two previous types of solar cells, silicon is deposited in a very thin layer on to a backing substrate – such as metal, glass or even plastic. Sometimes several layers of silicon, doped in slightly different ways to respond to different wavelengths of light, are laid on top of one another to improve the efficiency. The

production methods are complex, but less energy intensive than crystalline panels, and prices have been coming down as panels are mass-produced using this process.

One advantage of using very thin layers of silicon is that the panels can be made flexible. The disadvantage of amorphous panels is that they are considerably less effective per-unit area (up to 10%) and are generally not suitable for roof installations you would typically need nearly double the panel area for the same power output. Having said that, for a given power rating, they do perform better at low light levels than crystalline panels - which is worth having on a dismal winter's day, and are less likely to lose their efficiency as the temperature climbs.

However, there flexibility makes them an excellent choice for use in making building integrated PV (e.g., roofing shingles), for use on curved surfaces, or even attached to a flexible backing sheet so that they can even be rolled up and used when going camping / backpacking, or put away when they are not needed.

#### 1.5.1.4 Hybrid solar cells

One recent trend in the industry is the emergence of hybrid silicon cells and several companies are now investigating ways of mixing numerous materials to make SCs with improved efficiency, longer life, and at reduced costs.

Recently, Sanyo introduced a hybrid HIT cell whereby a layer of amorphous silicon is deposited on top of single crystal wafers. The result is an efficient solar cell that performs well in terms of indirect light and is much less likely to lose efficiency as the temperature climbs.

### 1.5.2 Second generation solar cells

Second-generation SCs are generally known as thin-film SCs because of their construction, as their layers are made up of few micrometers thick compared with multi-layered crystalline silicon-based cells. The specific combination of low-cost materials and ease in fabrication made this technology more attractive for the researcher community to produce inexpensive large area devices for commercial purposes.

There are mainly three different categories of SCs namely; amorphous silicon, and two that are made from non-silicon materials as cadmium-telluride (CdTe), and copper indium gallium di-selenide (CIGS). These technologies combinly produced about 16.8% of SCs panels being sold in 2009 [19-21].

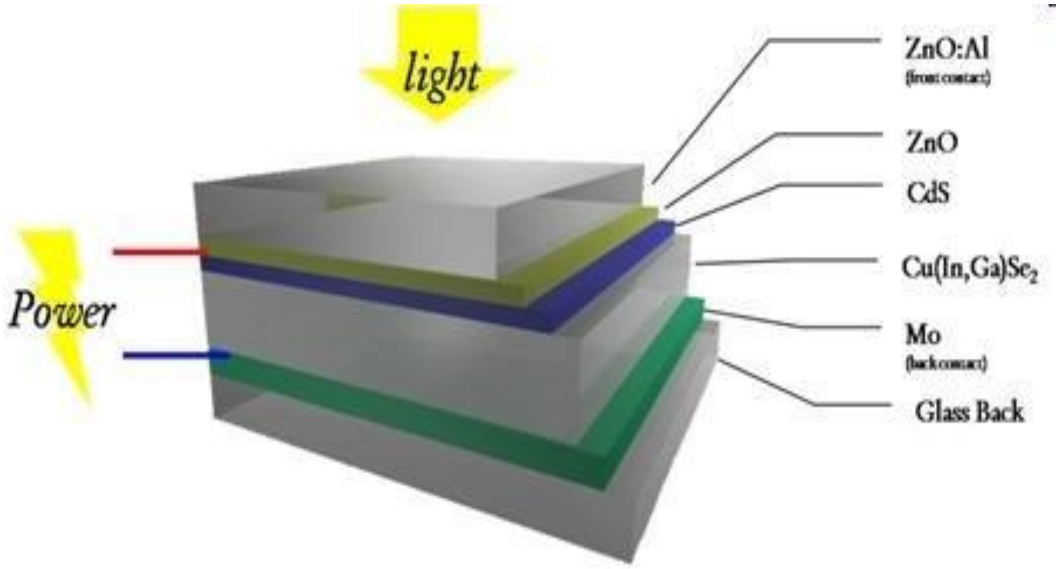


**Figure 7**: Schematic diagram of second-generation solar cells

First Solar, the number one producer and seller of solar panels in the world currently makes their solar cells using cadmium telluride. The big appeal of these type of solar cells is that they are inexpensive (currently below $1.00 / watt to produce and heading towards $0.70 / watt). However, as we discuss in the accompanying articles about cadmium telluride (CdTe) and First Solar – there are some concerns about this technology.

Venture capitalists love CIGS solar cells (or at least used to – as they have invested over $2.3 billion into companies developing these cells but have yet to see them be a commercial success) – as they have been able to reach efficiency levels of 20% in the laboratory. Unfortunately, it has turned out to be much more difficult to produce CIGS solar cells in mass quantities at competitive prices with anywhere near than efficiency level, so the jury is still out on this technology.

### 1.5.3 Third generation solar cells

Currently there is a lot of solar research going on in what is being referred to in the in the industry as Third-generation solar cells. In fact, according to the number of patents filed last year in the United States – solar research ranks second only to research in the area of fuel cells.

This is the hottest generation of SCs and being under an intense research. Here, a variety of materials have been employed (nano-tubes, organic dyes, silicon wires, and conductive plastics) except silicon to fabricate highly efficient SCs devices. The goal of course is to improve on the solar cells already commercially available – by making solar energy more efficient over a wider band of solar energy (e.g., including infrared), less expensive so it can be used by more and more people, and to develop more and different uses.

Currently, most of the work on third generation solar cells is being done in the laboratory, and being developed by new companies and for the most part is not commercially available. To date, PSCs reported PCE of 25.2% [22].

#### 1.5.3.1 Organic solar cells

In organic solar cells, organic polymers or small organic molecules are used for light absorption and charge transport. Organic materials are normally flexible and lightweight, allowing organic solar cells to be the same. In addition, molecular engineering makes the band-gap of organic materials tunable, and the thickness can be reduced to _ 100 nm due to optical absorption coefficients as high as $10^5$ $cm^{-1}$. [23] However, since the bandgap of most organic materials are large (above 2 eV for many cases), the harvesting of the incident light can be quite limited [24], which makes organic solar cells less efficient. The highest record efficiency for organic solar cells is still only 11% [25]. Apart from low efficiency, poor stability is another problem for organic solar cells. Photo-oxidation or degradation can easily occur under illumination and continuous exposure to oxygen or moisture, which results in the short lifetime of the organic

solar devices and hinders their practical application [14].

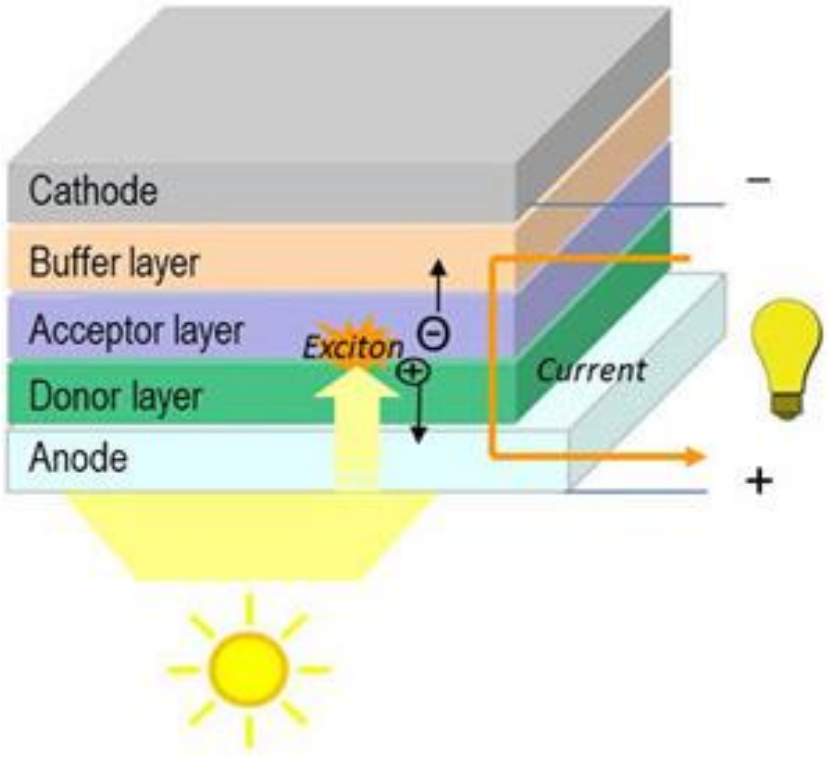


**Figure 8**: Schematic diagram of organic solar cells

### 1.5.3.2 Quantum dots solar cells

Quantum dots are nanocrystals of semiconducting materials. The diameter of the quantum dots is typically a few nanometers, which is so small that electrons are confined in all three dimensions due to the quantum confinement effect. The band-gap of quantum dots can be tuned simply by changing the dots size. As a result, photons with different wavelengths can be harvested at the same time using mixtures of quantum dots with
different sizes, which can potentially make multi-junctional solar cells. Using CsPbI3 perovskite quantum dots (coated with formamidinium iodide (FAI) to enhance the carrier mobility) as the absorbing material, a solar cell with a certified efficiency of 13.4% has been achieved, and a high open-circuit voltage ($V_{OC}$) of 1.2 V has been obtained [26].
Semiconductor nanocrystals (NCs) or quantum dots (QDs) have emerged in the last 25 years as a new class of fluorescence nanomaterial with unique properties. Much is now known about

how to control the size, shape, composition and surface chemistry of II–VI and III–V QD materials, allowing fine control of their photophysical and electronic properties. These insights have paved the way for application in a wide range of areas including biological imaging, solar cells, light emitting devices, phosphors and field-effect transistors.

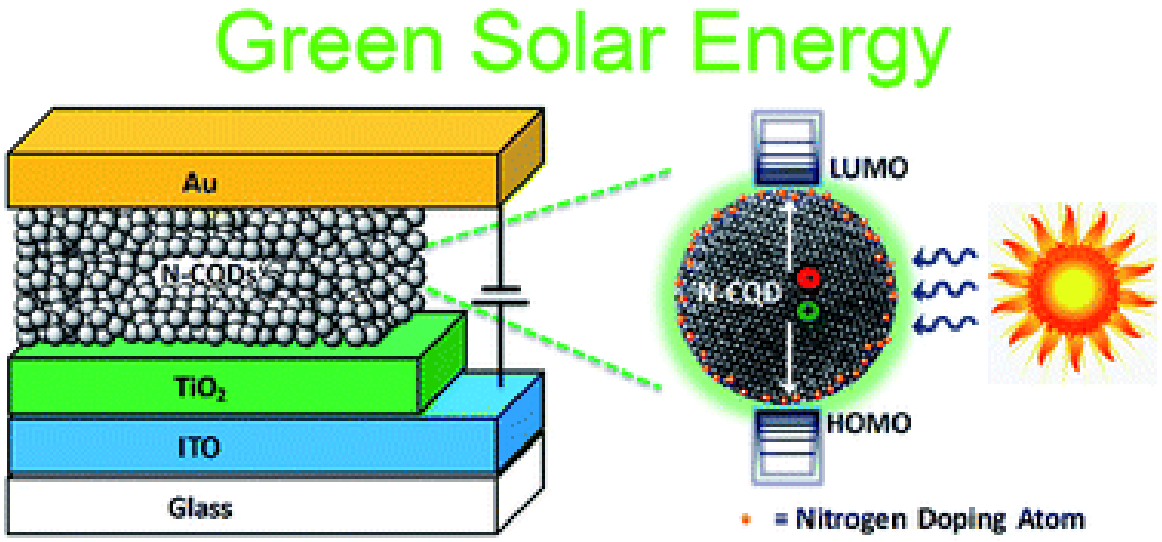


**Figure 9**: Schematic diagram of quantum dots solar cells

### 1.5.3.3 Dye-sensitized solar cells

A DSSC is based on a 5-20 µm layer of a mesoporous oxide (normally TiO2) formed between an anode and an electrolyte as shown in Fig. 10 [27]. The wide band-gap of TiO2 nanoparticles (3.2 eV) means they can only absorb light in ultraviolet region [28]. Therefore, in DSSCs, to enable the absorption towards sunlight in the visible region, a dye monolayer is adsorbed on the mesoporous TiO2 layer. Photo-generated electrons in the dye molecules are rapidly injected into the conduction band of TiO2 and then collected by the anode. The oxidised dye is then regenerated by a redox couple, normally the iodide /triiodide couple in the organic electrolyte which is further regenerated at the cathode. Overall, the device generates electric power from sunlight continuously without consuming the electrode materials or the electrolyte.

Since the report of the first highly efficient DSSC by Brian O'Regan and Michael Gratzel in 1991 with an efficiency of 7.1-7.9% [29], the efficiency has reached 13% in 2014[30]. Though the efficiency is still relatively low compared with silicon-based solar cells, DSSCs do show some advantages [31]. They can be produced using low-energy-consuming roll to- roll

techniques, on flexible substrates. They can also work under low light intensity condition due to the scattering effect of the mesoporous TiO2 nanoparticles in the film. The main problem hindering the application of DSSCs is their instability, mainly arising from the leaking of the liquid electrolyte [32-33]. The electrolyte solution is made up of volatile organic solvents which are hazardous to human health and the environment, and the corrosive nature of the redox couple to plastic sealants also makes the sealing of the electrolyte a big challenge. Alternatively, a solid p-type organic semiconductor with hole-transporting property is used to replace the liquid electrolyte, providing a solid-state DSSC. The most commonly used hole transporting material is Spiro-OMeTAD [20-33]. However, since the optimal film thickness of the mesoporous TiO2 layer is 2-3 _m which is not sufficient for efficient optical absorption [24], it ended up with no big improvement in the efficiency [34], until perovskite materials replaced dyes as the sensitizer.

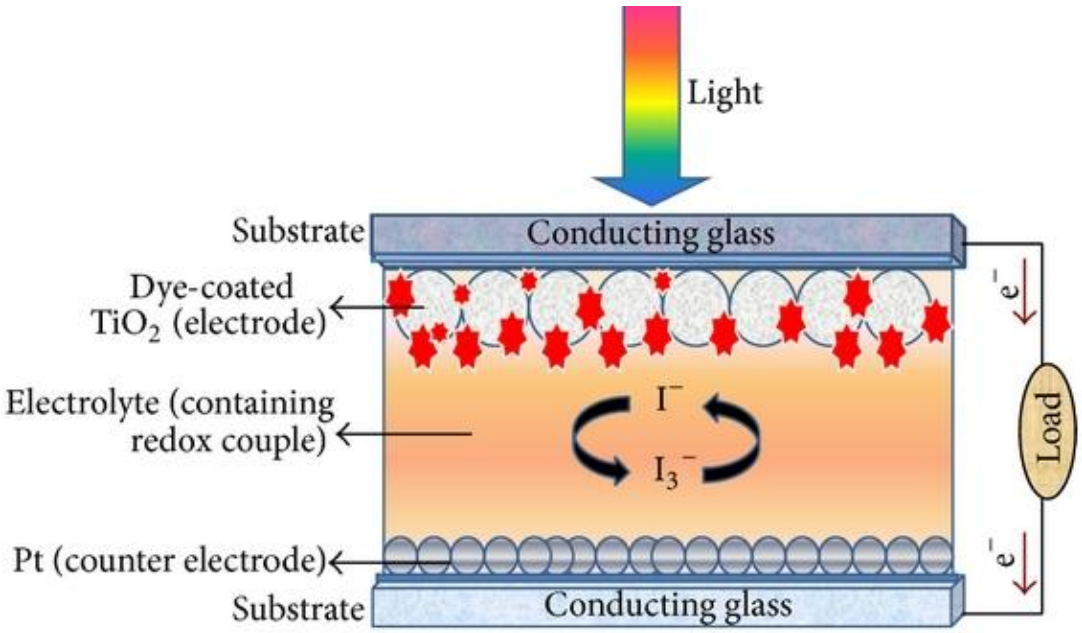


**Figure 10**: Schematic diagram of dye-sensitized solar cells

### 1.6 Perovskite solar cells

Since, the first use of perovskite in solar cells in 2009 [26], the efficiency of perovskite based solar cells has rocketed from 3.81% to 25.2 % [22]. Their development was so quick that they were named as a new type of solar cells - ‘perovskite solar cells’ (PSCs).

### 1.6.1 Structure of perovskite

Perovskite refers to a crystal structure originally found for CaTiO3. Compounds with perovskite structure normally have a generic chemical formula of ABX3, in which an A cation resides at the eight corners of the cubic cell and the B cation is located at the body center, surrounded by six X anions (located at the face centers), forming a BX6 octahedron, as shown in Fig. 11. Typically, the A cation can be Ca2+, Cs+, organo-ammonium ions such as methylammonium (MA) and formamidinium (FA), etc., the B site cation, which is smaller than the A cation, could be Ti 4+, Pb2+, Sn2+, etc., and the C anion could be halide ions or oxygen. To form a stable cubic perovskite structure, the size of the ions should meet some certain requirement [35-36].

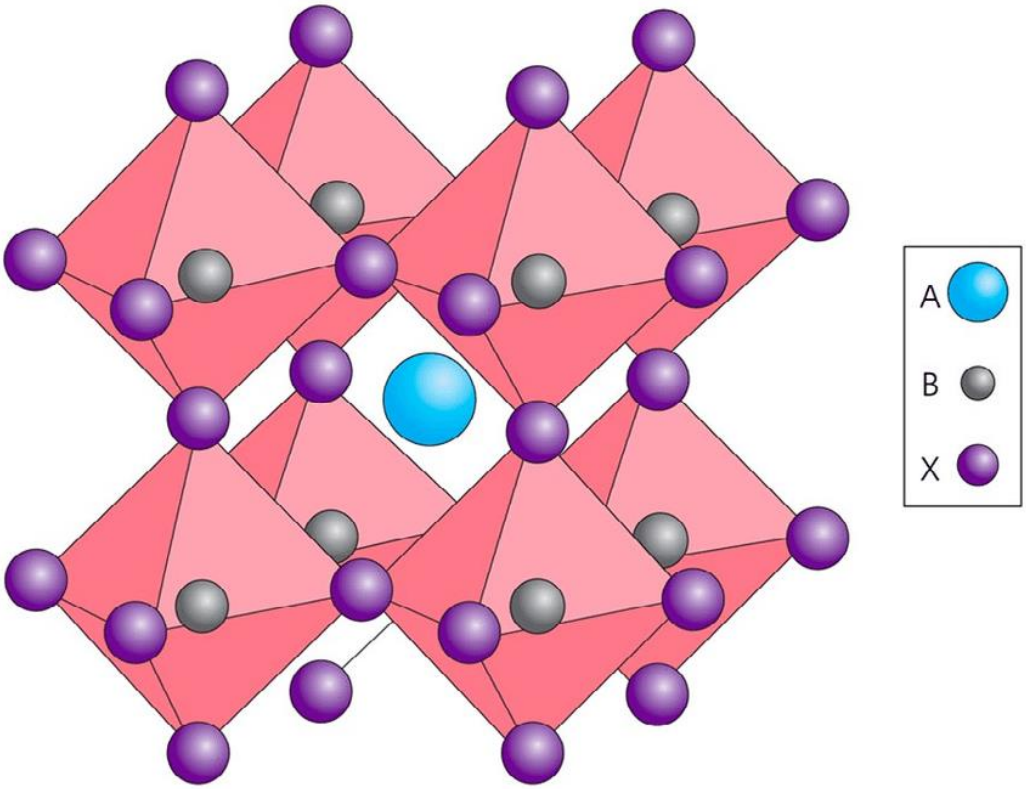


**Figure 11**: Crystal Structure of perovskite $ABX_3$ (A= cation, B= cation, X= anion)

### 1.6.2 History of Perovskite solar cells

Studies of perovskite solar cells first appeared in 2009 and evolved from DSSC technology. In DSSCs, the normal dyes only form a monolayer, thus the thickness of the mesoporous layer has to be around 10 _m in order for sufficient light absorption [37]. To enhance the light-absorbing ability, people were trying to develop alternative sensitizers. In 2009, Miyasaka and

coworkers [38] reported the utilization of MAPbI3 and MAPbBr3 perovskites as sensitizers in a DSSC with solution electrolyte. The perovskite materials absorbed light strongly and broadly in the visible range, so that complete light absorption can be achieved in films even as thin as 500 nm [39]. An efficiency as high as 3.81% was achieved for the MAPbI3 based cell, and a high photovoltage of 0.96V was obtained for the MAPbBr3 based device. N.G. Park and co-workers [40] optimized the TiO2 thickness, perovskite precursor concentration and TiO2 surface in 2011 based on a similar device structure, and further improved the efficiency to 6.54% with 3.6 nm-thick TiO2 films. However, the instability of perovskite in liquid electrolyte is fatal for these electrolyte-based cells. 80% degradation occurred in about 10 min under continuous illumination as the MAPbI3 perovskite was dissolved gradually by the redox electrolyte.

A breakthrough in the efficiency and stability of perovskite solar cells came with the use of solid-state hole transporting material (HTM) 2,2,7,7-tetrakis(N, N-p-dimethoxyphenylamino)-9,90-spirobifluorene (spiro-OMeTAD) in 2012. Park, Gr¨atzel and coworkers [ 41] reported a solid-state perovskite solar cell with MAPbI3 on a 0.6 _m m-TiO2 layer and spiro-MeOTAD as HTM, which showed a power conversion efficiency (PCE) of 9.7%. The use of spiro-OMeTAD also greatly improved the device stability compared to liquid electrolyte-based cells. Long-term stability for over 500 h was achieved, with the devices being stored in air without encapsulation. At a similar time, Snaith and coworkers [ 42] reported a mixed-halide MAPbI3-xClx perovskite solar cells with the same device structure, as shown in Fig. 1.6, delivering a PCE of 8%. They also replaced the mesoporous n-type TiO2 with mesoporous Al2O3. Al2O3 is an insulator (band-gap 7-9 eV), and cannot transport electrons. Surprisingly the device still worked and the electron transport in the Al2O3-based device was even much faster than in the TiO2-based device, and the VOC was also increased by a few hundred millivolts with the insulating Al2O3 scaffold, leading to a PCE of 10.9%. Even a planar junction device FTO/c-TiO2/MAPbI2Cl/spiro- OMeTAD/Ag without a mesoporous layer also exhibited an efficiency of 1.8%. These results mean that the perovskite layer can not only absorb light but also transport electrons out of the device. Since then, an explosion of research activities was triggered, and a variety of device configurations, deposition methods and material sets have been employed.

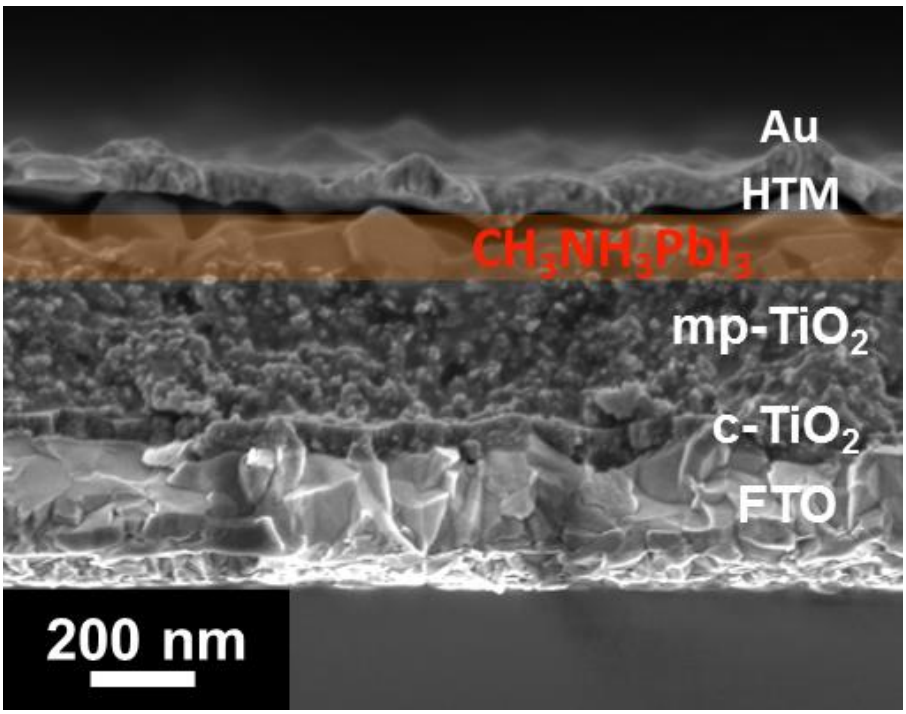


**Figure 12**: SEM cross-sectional image of a mesoscopic structured perovskite solar cell.

Gratzel and coworkers [43] investigated a mesoscopic MAPbI3/TiO2 heterojunction solar cell without an HTM layer, which still showed remarkable photovoltaic performance. An PCE of 5.5% was obtained with a short-circuit current density (JSC) of 16.1 $mAcm^{-2}$, a $V_{OC}$ of 0.63V, and a fill factor (FF) of 0.57. It shows that MAPbI3 can also work as the HTM in a heterojunction solar cell. Snaith [44] configured a planar FTO/c-TiO2/MAPbI3-xClx/spiro-OMeTAD/Ag device without a mesoporous layer utilizing a highly uniform MAPbI3-xClx layer synthesized via a dual-source vapour deposition route. The perovskite films showed extreme uniformity without pinholes, and thus avoided direct contacts between the spiro-OMeTAD and c-
TiO2 layers which could form shunting paths lowering the cell performance. An efficiency of over 15% was achieved, with an VOC of 1.07V. Generally, mixed halide perovskite MAPbI3-xClx showed better performance than pure iodide perovskite MAPbI3 [45–47], though no significant content of chloride in the lattice had been detected experimentally. The introduction of chloride is believed to improve the uniformity of perovskite films, as well as increase the carrier lifetime and diffusing length. Gratzel's group reported a mixed-cation perovskite [48]

based on mixed organic cations of MA and FA. It was found that the band-gap of perovskite (MA)x(FA)1-xPbI3 can be tuned by changing the FA content in the composition. The increase of FA content resulted in a red shift of absorption onset which means a smaller optical band-gap, while the light absorbing ability was decreased. Optimal absorption was obtained from MA0.6FA0.4PbI3, with a best efficiency of 14.9%. Saliba and coworkers further added a small amount of Cs into the binary mixed cations [49], forming a triple cation configuration Csx (MA0.17FA0.83) (100-x) Pb(I0.83Br0.17)3. The triple cation cells delivered stabilized PCEs up to 21.1%, and an PCE of 18% was still retained even after continuous aging for 250 hours under operational conditions. The triple cation configuration is now still giving the highest efficiency in perovskite family. F. Hao and M. G. Kanatzidis et al. [50] substituted lead with tin, and found that the band-gap of MASn1-xPbxI3 can also be tuned by changing the content of Sn. For MASn0.5Pb0.5I3, the smallest band-gap of 1.17 eV was obtained, smaller than both MAPbI3 (1.55 eV) and MASnI3 (1.3 eV), showing an PCE of 7.27%.

### 1.6.3 Deposition methods of perovskite films

As the key absorber material for perovskite solar cells, the quality of the perovskite layer is vital for the device performance. The deposition of the perovskite films is mainly based on the reaction of the organic ammonium MAX and the inorganic lead halide PbX2 components, where X= I, Cl, Br.

$$PbX_2 + MAX \rightarrow MAPbX_3 \quad (1)$$

Up to now, various deposition processes have been investigated for the fabrication of organometal halide perovskite films, which are mainly classified as one-step methods and two-step methods through solution processes, vapour processes, or a combination thereof.

#### 1.6.3.1 One-step methods

One-step methods are based on the co-deposition of both the organic and inorganic precursors through a solution process or a vapour process. Initially, most MAPbI3 or MAPbI3-xClx perovskite films were deposited by spin-coating a mixed solution of PbX2 (X=I, Cl) and MAI in organic solvents (DMF, DMSO, GBL), followed by thermal annealing. For MAPbI3, stoichiometric MAI and PbI2 (1:1) are dissolved in organic solvent for spin-coating deposition [31,51]. While for MAPbI3-xClx, a molar ratio of MAI: PbCl2 of 3:1 is normally used [32,52]. In order to obtain perovskite films with higher surface coverage and better uniformity, much

work has been done to control the crystallization of perovskite. Snaith's group [53] investigated the morphology of MAPbI3-xClx annealed at different temperature, and found that surface coverage dropped as the annealing temperature increased. Coverage of ~93% was obtained for the planar

MAPbI3-xClx film annealed at 90 °C, delivering an improved efficiency of 11.4%. Po-Wei Liang, Alex K.-Y. Jen et al. [54] added 1,8-diiodooctane (DIO) to the perovskite precursor as an additive, and found that the perovskite films prepared with 1 wt% DIO additive were much smoother and better covered than the pristine films, leading to a PCE ~12% in a planar perovskite solar cell. Jeon and Seok et al. developed a solvent engineering technique to improve the film quality [55], by toluene dripping while spin-coating of the perovskite precursor in the mixture of GBL and DMSO. This toluene dripping treatment enabled extremely uniform and dense perovskite layers and achieved a certified 16.2% PCE. Apart from solution processed one-step methods, a vapour based one-step method was also developed for the fabrication of high-quality perovskite films. Snaith and coworkers [34] successfully synthesized a uniform film of MAPbI3-xClx perovskite with a dual source vapour deposition method. MAI and PbCl2 were evaporated simultaneously under vacuum with a molar ratio of 4:1, and deposited on FTO substrates with compact TiO2. Fully crystallized perovskite layers were obtained after annealing. With this vapour-deposition method, efficient perovskite devices with an efficiency of 15.4% were yielded, with a JSC of 21.5mAcm$^{-2}$, a $V_{OC}$ of 1.07V and FF of 0.68.

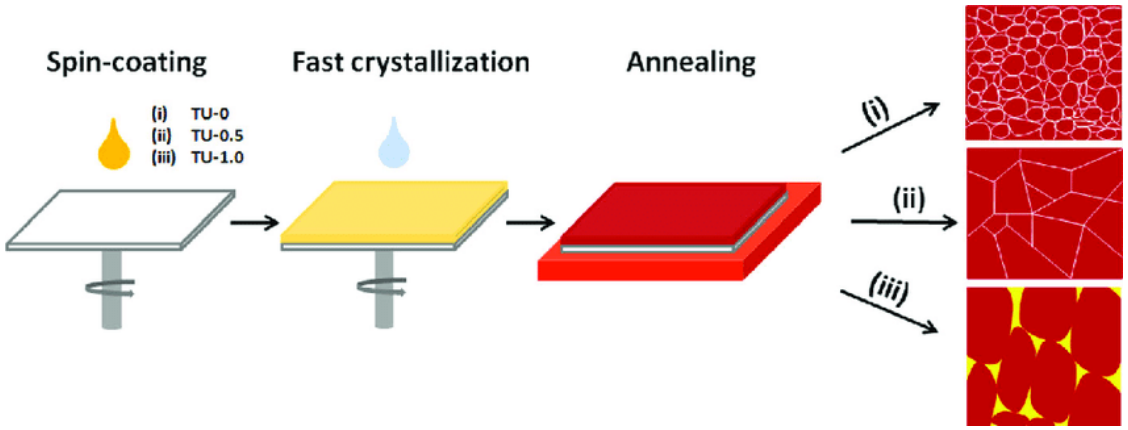


**Figure 13**: Schematic diagram of one-step method for perovskite film preparation

### 1.6.3.2 Two-step methods

Two-step methods, or sequential methods, are based on the formation of PbX2 films, normally by spin-coating, and their subsequent transformation into perovskite films. The transformation process can be done in different ways, as shown in Fig. 1.7: 1) dipping the PbX2 films into MAX solution [46,47]; 2) spin-coating MAX solution on top of the PbX2 films [56,99]; 3) evaporating MAX powder at elevated temperature and exposing the PbX2 films into the vapour [50].

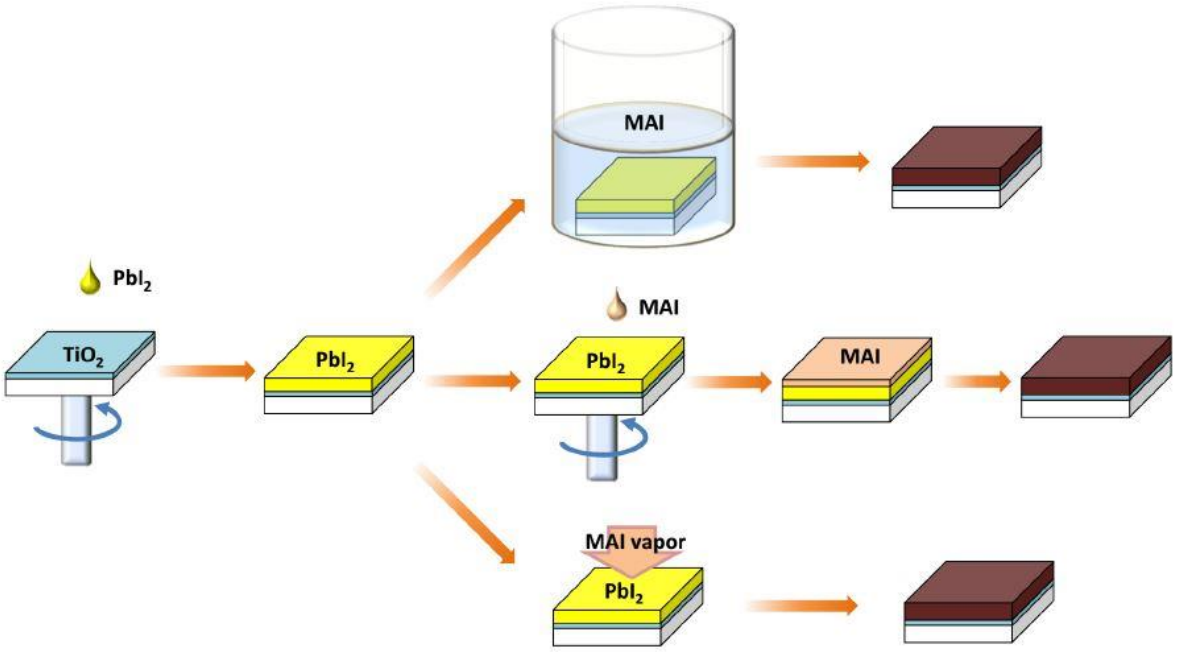


**Figure 14**: Schematic diagram of two-step method for perovskite film preparation

Two-step deposition methods allow for independent control in the deposition conditions of each precursor and hence their reaction thereafter, which eventually enables a better control over the perovskite film formation process. Julian Burschka and Michael Gr¨atzel et al. [56] spin-coated PbI2 film on a 350-nm-thick mesoporous TiO2 layer, and subsequently dipped it in a solution of 10 mg ml□1 MAI in IPA. The conversion of yellow PbI2 into dark brown perovskite occurred within seconds, and resulted in a PCE of approximately
15% with excellent reproducibility. In contrast, it takes much longer for complete conversion

in planar devices, as it is harder for MAI to diffuse into a planar PbI2 film. A dipping duration of approximately 20 min has been reported [60-61], or a higher reaction temperature (70 °C) is needed [62]. Qi Chen and Huanping Zhou et al. developed a vapor-assisted solution process (VASP) [60] for the fabrication of perovskite film, in which PbI2 was first spin-coated from solution and subsequently annealed in MAI vapor to form MAPbI3 films with microscale grain size, highly smooth surface and full coverage. The obtained optimum planar device showed a PCE of 12.1%. Chang-Wen Chen and Hao-Wu Lin et al. [63] prepared MAPbI3-xClx films through a layer-by-layer sequential vacuum deposition process. Extremely smooth PbCl2 films were thermally sublimed onto PEDOT:PSS-coated indium tin oxide (ITO) glass, followed by the sublimation of MAI, which resulted in ultra-smooth MAPbI3-xClx films with full surface coverage. The champion cell performed a high PCE of 15.4%, with a JSC of 20.9mAcm$^{-2}$, an $V_{OC}$ of 1.02 V and a high FF of 0.72.

### 1.6.4 The bright future of perovskite solar cells

The band-gap for MAPbI3 perovskite is ~1.5 eV, corresponding to an absorption onset of 800 nm, which makes it a good absorber over the whole wavelength range of visible light. The high absorption co-efficient of 1:5 104 cm$^{-1}$ at 550 nm and 0:5 104 cm$^{-1}$ at 700 nm allows sufficient absorption even with a small film thickness [29]. And the high carrier mobilities (11.6 cm2 V$^{-1}$ s$^{-1}$ for MAPbI3-xClx and ~8 cm$^2$ V$^{-1}$ s$^{-1}$ for MAPbI3 [64]) along with the long carrier lifetime (hundreds of nanoseconds) result in a long carrier
diffusion length (ranging between 100 nm and 1,000 nm [65]). These together greatly decrease the possibility of recombination within the bulk.

Typically, perovskite solar cells employ a n-i-p or p-i-n junction structure in which a perovskite layer (intrinsic semiconductor layer) is sandwiched between an n-type electron transporting layer (ETL, normally TiO2 or PCBM) and a p-type hole-transporting layer (HTL, normally spiro-OMeTAD, NiOx or PEDOT:PSS). The energy level alignment as shown in Fig. 15 is favorable for charge separation [32]. After excitation, the photoelectrons can be fast injected into the conduction band of TiO2, while the holes are transported into the HOMO of spiro-OMeTAD. In this way the charge carriers are separated and recombination can be alleviated.

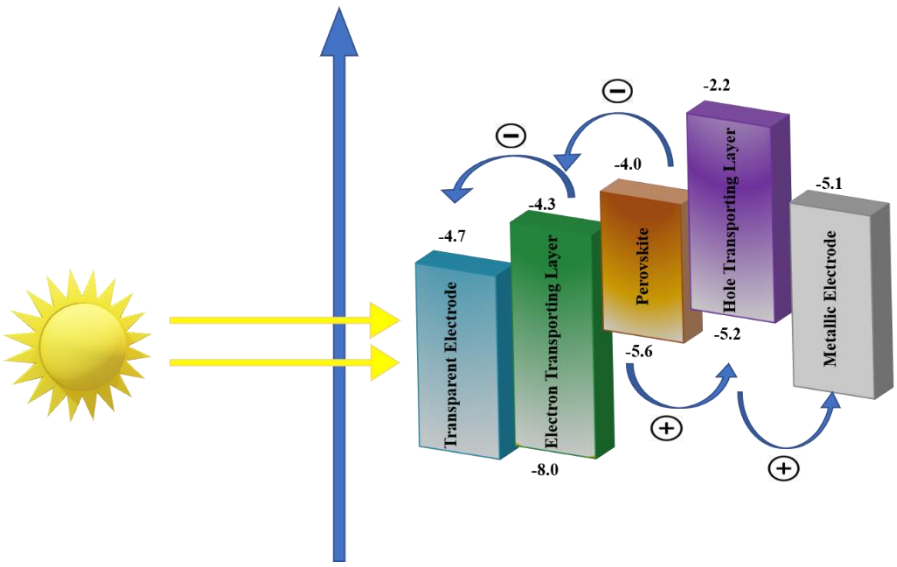


**Figure 15**: Energy level diagram of a typical n-i-p structured perovskite solar cell

The preparation methods of perovskite, both one-step and two-step, are simple, low energy-consuming and capable of producing high quality perovskite films. Roll-to-roll processes such as spray-coating and blade-coating also make the production of perovskite devices easy to scale up. These factors, along with the abundance of raw materials, mean perovskite solar cells have a short energy payback time (EPBT, defined as the ratio of the total primary energy consumption to the annual electricity generation), which is estimated to be 0.3 years, much shorter than silicon-based devices, as shown in Fig. 16 [66].

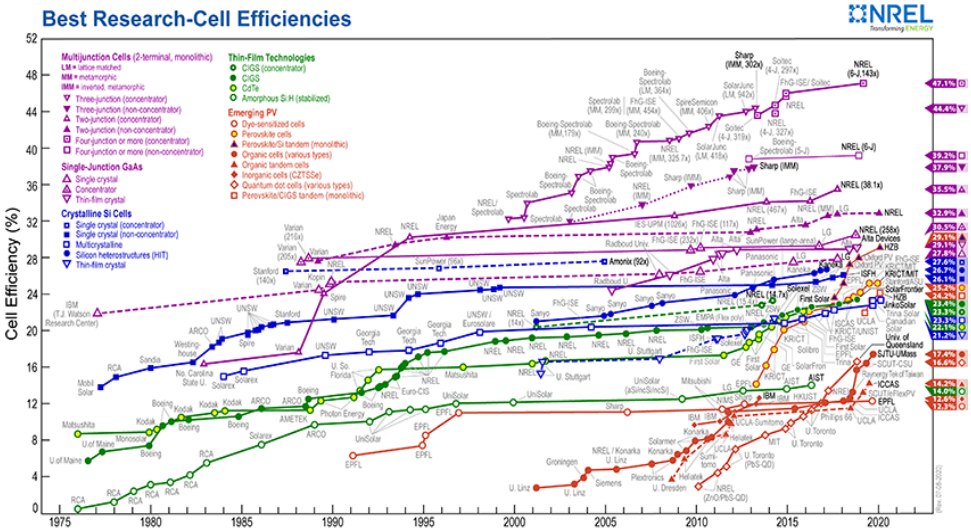


**Figure 16**: Comparison in the energy payback time of typical PV modules

The rapid development of perovskite solar cells has sparked the hope of their practical application. Dar and Gr¨atzel used cheap inorganic CuSCN as HTMs for perovskite solar cells [67], which achieved stabilized PCEs exceeding 20%. By incorporating a reduced graphene oxide interlayer between the CuSCN and gold layers, over 95% of the initial efficiency of the cells was successfully retained after 1000 hours aging at the maximum power point at 60 °C. Nazeeruddin's group [68] developed a 2D/3D (HOOC(CH2)4NH3)2PbI4/MAPbI3 perovskite junction, and fabricated 10 × 10 $cm^2$ solar modules through a fully printable route. The large area modules delivered stable 11.2% efficiency with no efficiency decrease
for over 10000 h. Furthermore, there have been numerous industrial companies worldwide, such as Solar-Tectic, Oxford PV, Frontier Energy Solution and Micro quanta Semiconductor, dedicated to the commercialization of the perovskite technology. Hopefully, perovskite solar cells will find their real applications in the near future.

### 1.6.5 Issues to be addressed

Though organometallic halide perovskite based solar cells have shown many extraordinary properties and promising efficiency, there are still some issues to be addressed before their large-scale application.

#### 1.6.5.1 Hysteresis

Hysteresis is a phenomenon commonly observed during the performance tests of perovskite solar cells. When scanned from different directions during current-voltage behavior tests, different J-V curves can be obtained, as illustrated in Fig.17 [69-70]. The current-voltage curve taken with decreasing voltage (reverse scan) tends to exhibit higher currents at each voltage than the curve taken with increasing voltage (forward scan). As a result, the performance of perovskite devices can be overestimated. Several ideas have been proposed as the cause of this phenomenon, including trap states [70], ferroelectricity [ 71,22] and ion migration [73–76]. The idea that it is caused by ion migration is being accepted by more and more researchers, but more work is still needed for better understanding and the avoidance of hysteresis.

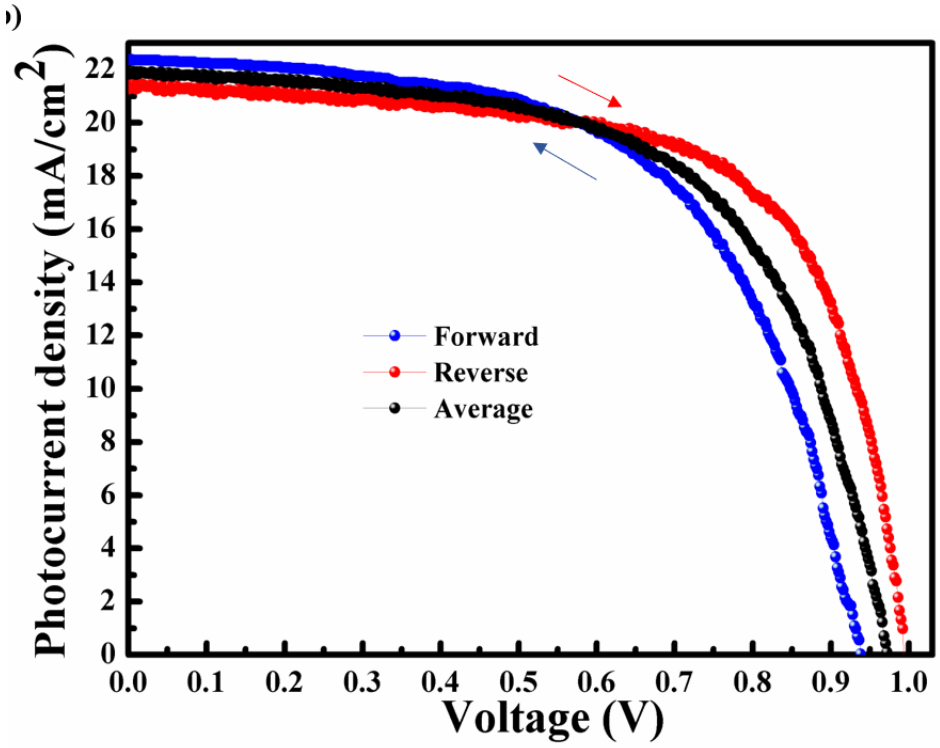


**Figure 17**: J-V curves with forward and reverse scans showing hysteresis and average scan showing best average value

Hysteresis has been found to be much more severe in planar devices than in mesoporous devices, and strongly dependent on the scan speed, light-soaking and pre-biasing conditions [ 77,80], temperature [81], perovskite crystal size [82-85] and contacts used [86-88]. For the accurate measurement of perovskite solar cells, it is generally required to include the data of both forward and reverse J-V curves at various scan rates as well as the steady state photocurrent at voltages near the maximum power point (Pmax) when efficiencies are reported [89].

**1.6.5.2 Stability**

Stability is probably the biggest challenge preventing practical applications of perovskite solar cells. For the decomposition reaction

$$MAPbI_3 \rightleftharpoons PbI_2 + MAI \quad (2)$$

the change in the Gibbs free energy at 300K is Δ G° 300K = 0:16 eV per formula unit [90],

indicating the perovskite structure is chemically stable under standard conditions, but the small magnitude suggests the stability is very fragile and can be shifted easily, especially with the existence of water. Since MAI is highly water soluble, the saturation concentration to suppress the decomposition of MAPbI3 is estimated to be as high as ~8 g=L [88], which means a small amount of water can result in serious decomposition of the perovskite phase. Besides, further decomposition can occur through reaction 1.4 which can be further accelerated by oxygen or UV light due to the consumption of the HI [84] through the reactions illustrated in Equation 1.5 and Equation 1.6, respectively. It was found that MAPbI3 would be degraded completely into PbI2 after 18 h exposure in air with a humidity of 60% at 35°C [84]. As a result, optimized device architecture and proper encapsulation are required for the long-term stability of perovskite solar cells.

$$MAI\ (aq) \rightleftharpoons CH_3NH_2\ (aq) + HI\ (aq) \quad (3)$$

$$4HI\ (aq) + O_2\ (g) \rightleftharpoons 2I_2\ (s) + 2H_2O\ (l) \quad (4)$$

$$2HI\ (aq) \rightleftharpoons H_2\ (g) + I_2\ (s) \quad (5)$$

**1.6.5.3 Toxicity**

Lead compounds are very hazardous for the environment, and the impact of lead-based perovskite devices on the environment is a big concern for their large-scale application. Several researchers have tried to replace Pb with other less toxic elements such as Sn [85,86]. Though MASnI3 also showed good semi-conductive properties with a bandgap of ~1.3 eV, Sn2+ is easily oxidized into Sn4+ which can cause p-type doping to the material [85]. Partial replacement of Pb with Sn has also been investigated to reduce the use of lead [77–79], but the highest PCE so far reported for Sn-Pb alloy-based perovskite solar cell is only 15.2% for MASn0.25Pb0.75I3 [88], and stability is still a problem. So, until now, the most efficient perovskite solar cells still have to be based on lead, but with proper encapsulation and the development of lead recycling processes which is also extremely important for lead acid batteries, the harm of lead content to the environment could be minimized.

# Chapter 2 - Experimental Section

## *Synthesis of Materials*

### 2.1 Synthesis of Methylammonium Iodide

Methylammonium iodide was prepared specially in our own lab by reacting a hydroiodic acid (30 mL, 0.227 mol, 57 wt.% in water, Aldrich) and methylamine (27.8 mL, 0.273 mol, 40% in methanol, TCI) were stirred in the ice bath for 2 h. After stirring at 0°C for 2 h, the resulting solution was evaporated at 50°C for 1 h and produced synthesized chemicals (CH3NH3I). The obtained material powder was washed multiple times with diethyl ether and hot dried under vacuum and have been used without any further purification.

### 2.2 Synthesis of Methylammonium Chloride

Methylammonium chloride was prepared specially in our own lab by reacting a hydrochloric acid (30 mL, 0.227 mol, 37 wt.% in water, Aldrich) and methylamine (27.8 mL, 0.273 mol, 40% in methanol, TCI) were stirred in the ice bath for 2 h. After stirring at 0 °C for 2 h, the resulting solution was evaporated at 50 °C for 1 h and produced synthesized chemicals (CH3NH3I). The obtained material powder was washed three times with diethyl ether and dried under vacuum and used without further purification.

### 2.3 Synthesis of compact Titanium Oxide (c-$TiO_2$)

The synthesis of compact titanium oxide precursor solution was done by reacting titanium source (a titanium(IV) diisopropoxide bis(acetylacetonate), Aldrich 97%) of 0.152 μL in 1.874 mL of 1-Butanol. Stir the precursor solution for about 30 minutes in a sonicator for complete reaction. The resulting solution has a yellow color.

### 2.4 Synthesis of mesoporous Titanium Oxide (mp-$TiO_2$)

The synthesis of mesoporous titanium oxide precursor solution was done by reacting 1.6g of titanium paste of 40 nm size in 10 mL of anhydrous ethanol (99%, Aldrich) and stir the solution for about 12 hrs. at room temperature for complete reaction of the solution. The resulting solution has a whitish color.

### 2.5 Synthesis of Zinc Oxide Sol-Gel Solution (ZnOs-g)

The synthesis of zinc oxide sol-gel precursor solution was done by reacting 1.6 g zinc acetate dihydrate, 0.5 g of ethanol amine and dissolved in 10 mL of 2-methoxy ethanol and stir the solution for about 12 hrs. at room temperature to establish the complete reaction.

### 2.6 Perovskite solar cells device fabrication

The standard procedure was adopted to fabricate planar heterojunction PSCs and it follows the chronological order as seen bellow.

1. Cleaning of FTO substrate
2. Spin-casting of Compact-$TiO_2$ (c-$TiO_2$)
3. Spin-casting of mesoporous -$TiO_2$ (mp-$TiO_2$)
4. Spin-casting of ZnO Sol-Gel. (ZnO s-g)
5. Dip-coating processed $Pb(NO_3)_2$ layer.
6. Dip-Coating processed perovskite layer.
7. Spin-casting of spiro-OMeTAD
8. Thermal evaporation of thin layer of $MoO_3$
9. Thermal evaporation Metallic electrode (Ag, Au)

The glass substrates with attached fluorine doped tin oxide (FTO) were purchased from the company Thin film devices Inc. and were received in squares of 15×15 $mm^2$. The FTO covers 75 % of the glass substrates surface and are 300 nm thick with a sheet resistance of 7 Ω/sq.

### 2.7 Cleaning of FTO substrates

The FTO/glass substrates need to be cleaned before the different layer dispositions can commerce, because even a small dust particle on the surface will affect the final cells performance. This was done in five steps. First to fourth step were done by cleaning in ultrasonic bath for about 30 min for every step. The ultrasonic bath uses high frequency sound waves that induce cavitation bubbles that remove contaminations on the substrates. Between every step the substrates were placed in a new beaker to minimize the mixing of solvents. The first cleaning step was done with Extran MA01 detergent mixed with deionized water in a 1:10 volume ratio. The second cleaning step was done with deionized water, third step was with ethanol and fourth with acetone (Alfa Aesar Chemicals). Fifth and last step was to dry the

substrates in oven of 120 ºC for minimum 2 h. To minimize left over solution on substrates after step four, all substrates were pick up one by one from the beaker and blow dry before placed to dry in oven.

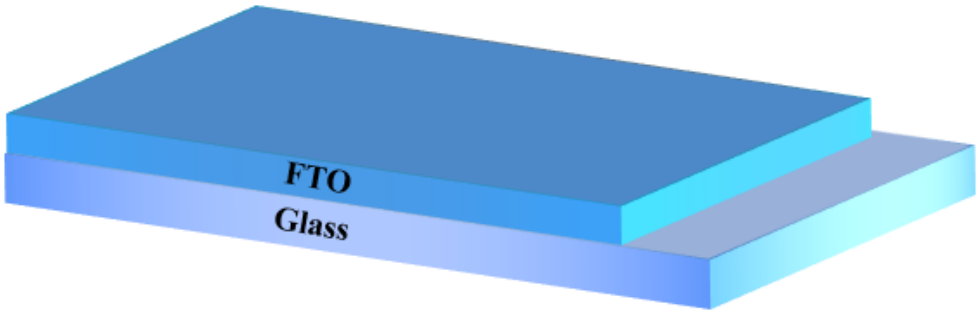


**Figure 1**: Schematic figure of the cleaned glass/FTO substrate

Figure 18 above shows the layers that been cleaned by all above steps and how much approximately the FTO covers the glass surface.

### 2.8 Preparation of compact $TiO_2$ (c-$TiO_2$) layer by spin-casting

The solution used for the c-Tio2 layer was synthesized by reacting titanium source (Titanium diisopropoxide, Aldrich 97%) of 0.152 µL in 1.874 mL of 1-Butanol. Stir the precursor solution for about 30 minutes in a sonicator for complete reaction. The resulting solution has a yellow color.

The cleaned FTO/glass substrate were UV-ozone treated for about 15 minutes and then placed on the spin-coater after masking to keep some of the FTO free from $TiO_2$, not to block the transparent electrode. The specific programme was set in spin-coater machine in three different batches to deposit the c-$TiO_2$ layer smoothly. After depositing c-$TiO_2$ layer on to the FTO substrate, the substrates were transferred into the muffle furnace for annealing at 500°C for 1 hr.

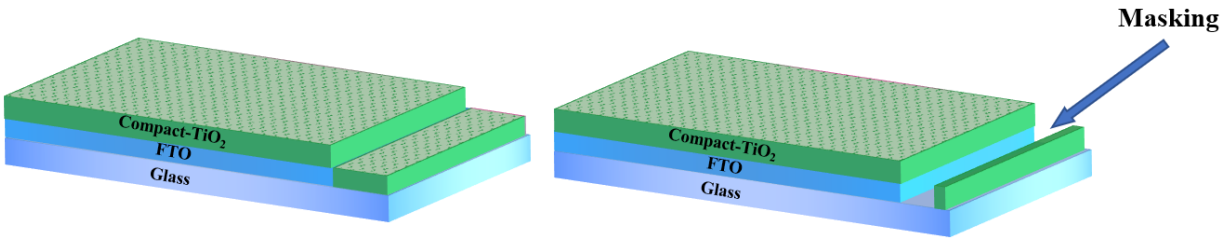


**Figure 2**: Schematic structure when the c-TiO2 layer was deposited on to the FTO substrate and masking of substrate

### 2.9 Preparation of mesoporous $TiO_2$ (mp-$TiO_2$) layer by spin-casting

The solution used for the mp-$TiO_2$ layer was synthesized by reacting 1.6g of titanium paste of 40 nm size in 10 mL of anhydrous ethanol (99%, Aldrich) and stir the solution for about 12 hrs. at room temperature for complete reaction of the solution. The resulting solution has a whitish color.

After depositing c-$TiO_2$ layer, the layer was dried at room temperature for 10 mints and the annealed at 100°C for 10 mints. After cooling down the substrates were transferred on the spin-coater to deposit mp-$TiO_2$ layer. The specific programme was set in spin-coater machine in three different batches to deposit the mp-$TiO_2$ layer smoothly. After depositing mp-$TiO_2$ layer on to the FTO substrate, the substrates were transferred into the muffle furnace for annealing at 500°C for 1 hr.

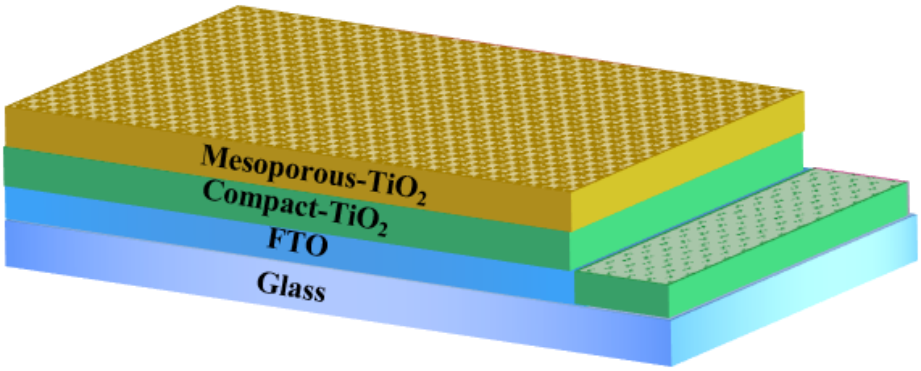


**Figure 3**: Schematic structure of the deposited mp-$TiO_2$ layer over c-$TiO_2$ layer

### 3.0 Preparation of ZnO sol-gel layer by spin-casting

The ZnO sol-gel was synthesized by reacting zinc acetate dihydrate (1.6 g, Sigma Aldrich, 99.9%), ethanolamine (0.5g, Sigma Aldrich, 99.5%) and 2-methoxyethanol (10mL, Sigma Aldrich, 99.8%) for 12 hrs at room temperature. Over the c-$TiO_2$ or mp-$TiO_2$ layer, the ZnO layer was spin-cooted with ZnO sol–gel solutions at 5000 rpm for 30 s. After the ZnO sol-gel were spin-coated, a cotton-swab rinsed in acetone was used to remove the ZnO from the same area that was masked during-$TiO_2$ deposition and annealed the film at 300˚C for 1 hr.

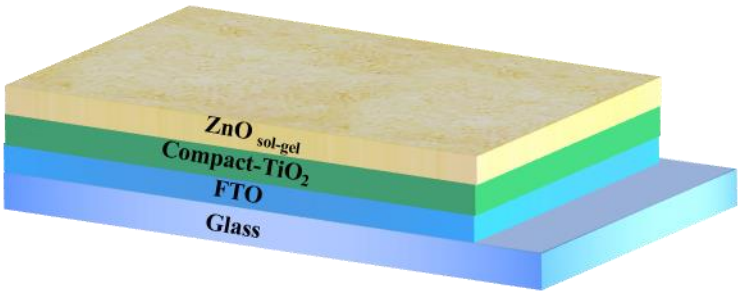


**Figure 4**: Schematic structure when the ZnOs-g layer was deposited on to the c-$TiO_2$/mp-$TiO_2$ layer

### 3.1 Preparation of $Pb(NO_3)_2$ layer by dip-coating method

To avoid the conventional spin-casting process of $PbI_2$, we employed novel $Pb(NO_3)_2$ layer by a simple dip-coating approach to avoid the use of detrimental organic solvents (DMSO and DMF) which is required to dissolve the $PbI_2$ and to produce large area films for industrialization which is not possible with spin-casting approaches. In a typical process, a c/mp$TiO_2$ covered ZnO substrate were first dipped into an aqueous 0.1M of $Pb(NO_3)_2$ (Sigma-Aldrich, 99.9%) precursor solution prepared in ethanol (EtOH)/water (2 : 1, v/v) for 30 sec. The substrate was washed using deionized water and ethanol and then annealed at 120 C for 10 min, resulting in a highly transparent film over the substrate. The $Pb(NO_3)_2$ layer is likely to adsorb over zinc oxide surface.

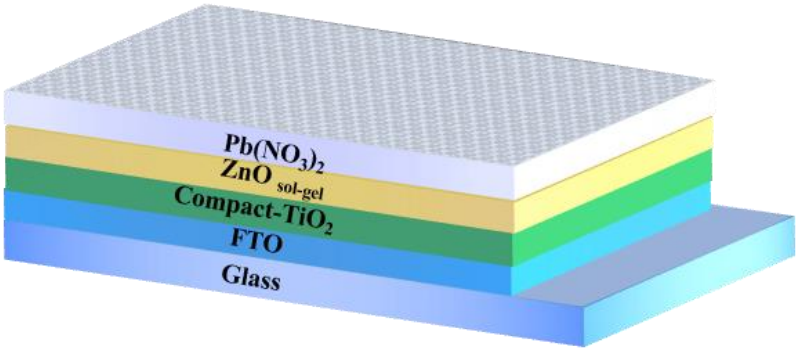


**Figure 5**: Schematic structure of the adsorbed $Pb(NO_3)_2$ layer over ZnO coated substrate

### 3.2 Preparation of Perovskite layer by dip-coating method

To fabricate $MAPbI_3$ and $MAPbI_{3-x}Cl_x$ perovskite films from an aqueous $Pb(NO_3)_2$, we employed a sequential deposition coating (SDC) approach followed by various successive solid-state ion-exchange and reaction SSIER repetitions. The methylammonium iodide (MAI) and methylammonium chloride (MACl) solution was prepared in isopropanol (IPA). The perovskite solution was prepared by adding the 0.1 M MAI into 10mL IPA to prepare $MAPbI_3$ perovskite films, while, to prepare $MAPbI_{3-x}Cl_x$ mixed halide perovskite films, we added different amount of 0.045M, 0.075M and 0.090M MACl in 0.1M of MAI solution, respectively. The substrate was dipped into MAI or MAI/MACl mixed halides dissolved in isopropanol (IPA) for 30 sec. and then washed with chloroform and diethyl ether and annealed at 100°C and at 120°C for 10/60 mints. The above procedure formed one SSIER cycle. These films were subjected to SSIER repetitions to complete the reaction between $Pb(NO_3)_2$ and MAI or MAI/MACl to fabricate most stable and an efficient perovskite film morphology.

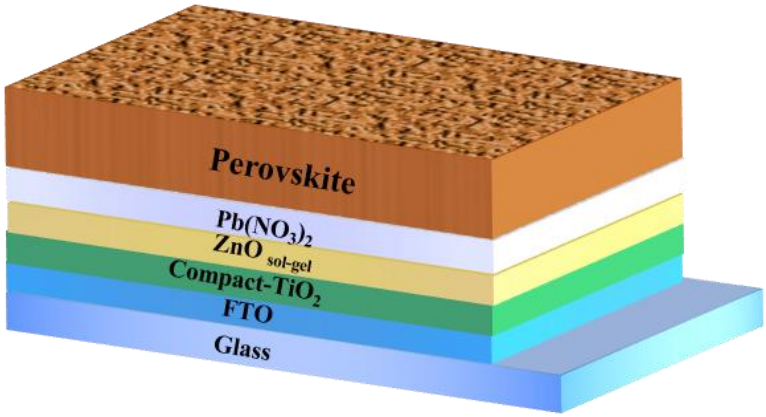


**Figure 6**: Schematic structure of the prepared $MAPbI_3$/ $MAPbI_{3-x}Cl_x$ perovskite layers by a simple dip-coating technique

### 3.3 Spin-coating of spiro-OMeTAD layer

The spiro-OMeTAD was employed as hole transport material (HTM) via spin-coating at 3000 rpm for 30 sec. The HTM solution was prepared by dissolving 29 mg of spiro-OMeTAD, 7 mL of 170 mg mL- Li-TFSI in acetonitrile, and 11 mL of t-BPy to boost the performance of the devices. The perovskite and spiro-OMeTAD were scratched away using a scalpel and wiped with cotton-swabbed rinsed with 2-methoxy ethanol. 2-methoxy ethanol was used because it removes the perovskite and spiro-OMeTAD without reacting to the FTO substrate. This was done on the same area of the substrates that been free of compact and mesoporous $TiO_2$ with the reason to expose the FTO for the cathode contact.

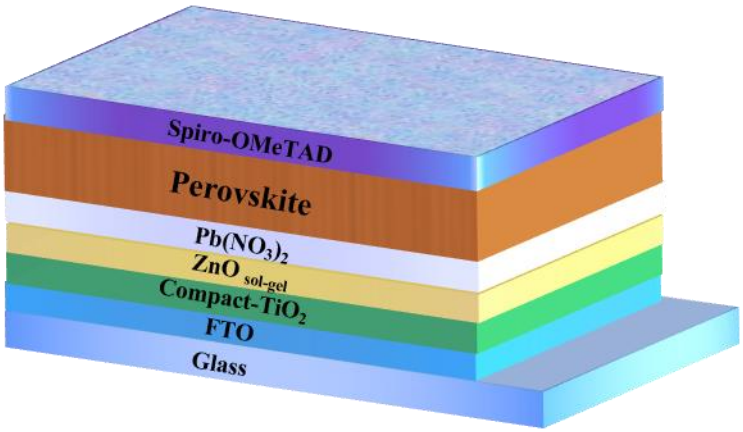


**Figure 7**: Schematic structure of the deposited spiro-OMeTAD layer over $MAPbI_3$/ $MAPbI_{3-x}Cl_x$ perovskite layers

### 3.4 Thermal evaporation of $MoO_3$ and silver (Ag) Electrode

The samples were placed in a masked holder for the substrates to only get evaporated metal on wanted surface area and then placed in the evaporator. The evaporation started by lowering the pressure in the evaporator and when the pressure reached vacuum of $< 3.5\times10^{-6}$ mbar. Finally, device fabrication was completed by thermal evaporation of 10 nm thin MoO3 layer and 100 nm thick Ag electrode on top of the HTM film under reduced pressure (less than $10^{-5}$ Torr).

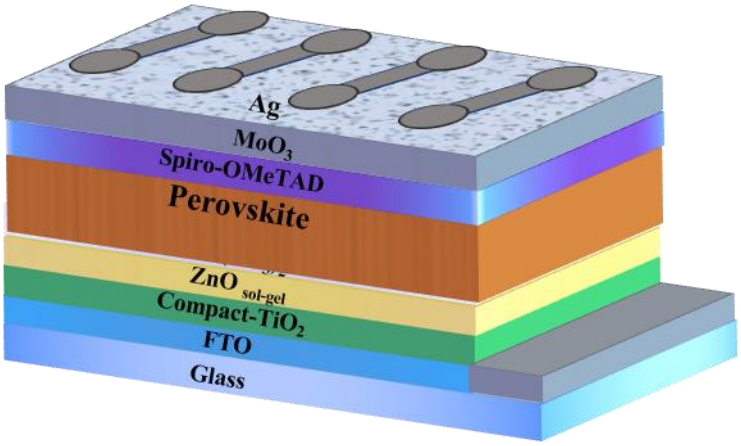


**Figure 8**: Schematic structure of the completely sequentially dip-coated processed perovskite layers fabricated perovskite solar cells device architecture

### 3.5 Measurements and Instruments

The absorption spectra were recorded on a PerkinElmer Lambda 2S ultraviolet (UV)-visible spectrometer. The surface morphologies were imaged using a field emission scanning electron microscope (FESEM, Nova Nano-SEM 450, FEI, Netherlands). Elemental analysis and presence of newly formed chemical bonds with Pb, I, and Cl in perovskite compounds were performed using X-ray photoelectron spectroscopy (XPS, AXIS-NOVA, KratosInc, USA). The perovskite crystallinities of the $MAPbI_3$ layers were investigated using X-ray diffraction (XRD, D/Max2500 V/PC, Rigaku Corp, Japan). The solar cell efficiencies were characterized under simulated 100 mW $cm^{-1}$ AM 1.5G irradiation from a Xe arc lamp with an AM 1.5 global filter. The simulator irradiance was characterized using a calibrated spectrometer; the illumination intensity was set using a silicon diode with an integrated KG1 optical filter certified by the National Renewable Energy Laboratory. The spectral mismatch factors were calculated to be less than 5% for each device. The short circuit currents were also found to be within 5% of the values calculated using the integrated external quantum efficiency (EQE) spectra and solar spectrum. The applied potential and cell currents were measured using a Keithley 2400 model digital source meter. The *J–V* curves were measured at a voltage settling time of 100 ms. The EQEs were measured by under-filling the device area using a reflective microscope objective to focus the light output from a 75 W Xe lamp, monochromator, and optical chopper; the

photocurrent was measured using a lock-in amplifier; and the absolute photon flux was determined using a calibrated silicon photodiode and was recorded for 5 s per point (80 points) from 360 to 900 nm. In the *J–V* curves hysteresis tests, a forward scan indicates the measurement of the sweeping voltage from short circuit to forward bias, whereas a backward scan indicates a sweep in the opposite direction. To explore the active area of the device and avoid the scatter effects of the edges, a non-reflective metal plate mask with an aperture of 4.5 $mm^2$ was used for the solar cells.

# Chapter 3

## *Dip-Coating Processed Perovskite Layers from an Aqueous Lead Precursor for High Efficiency Perovskite Solar Cells*

## 1. Introduction

Currently, organic-inorganic lead halide perovskite solar cells (PrSCs) have established significant attention because of their excellent breakthrough power conversion efficiencies (PCEs) of ~21%, making them potential surrogates for conventional silicon-based solar cells [1–10]. Most of the organo-metallic halides, particularly alkylammonium lead halides, (RNH3) PbX3 (R = alkyl, X = Cl, Br, I), bears a direct-band-gap material which is specifically used as hybrid organic-inorganic perovskite cores with excellent electron and hole conduction and photo-sensitizer performance [11,12]. The surface topology, uniform crystallinity, and smoothness of perovskite materials on substrate are crucial factors for improving the PCEs of PrSCs devices. Hereafter, a noteworthy consideration has been dedicated to develop an effective fabrication approaches to prepare perovskite layers. A variety of approaches have been employed to enhance the PCEs with lead sources of $PbX_2$, $Pb(OAc)_2$, or $Pb(NO_3)_2$ [13,14]. Therefore, the projected methods include: (1) the film deposition by spin-coating of a lead source followed by reaction with methylammonium iodide ($CH_3NH_3I$, MAI), by vertically dipping the substrates into this solution, spin-coating, or vacuum deposition [2–15]; and (2) by the direct spin-coating of a perovskite materials in combination with, adduct, heat treatment, interfacial engineering, solvent-engineering, or by adding additives [16–25]. These approaches have already ensured improved PCEs; however, there are size limitations because the fabricated PrSCs normally have small active areas. Therefore, it is interesting, yet important for marketable applications, to develop cost-effective engineering processes that simplify large area production of perovskite morphologies, via effective routes such as dip-coating, doctor-blade methods, and inkjet or roll-to-roll printing [1–26].

It is important to know that most of the investigations have been done with toxic high-polarity aprotic organic solvents, such as dimethylformamide (DMF, DMSO), because of quite poor solubility of lead precursors in other green solvents. Therefore, non-halide lead precursors, such as $Pb(OAc)_2$ and $Pb(NO_3)_2$, have recently got huge attention and are under intense research due to their specific compatibility with non-toxic green solvents such as water. Heish et al. described a $MAPbI_3$ perovskite film morphology prepared with sequential deposition method [27]. For this, an aqueous $Pb(NO_3)_2$ precursor solution was spin-coated onto UV/ozone mesoscopic $TiO_2$ (m-$TiO_2$)/compact $TiO_2$ (c-$TiO_2$) layers, followed by another two-step

reaction in the MAI to prepare perovskite films. In the first, a layer of $PbI_2$ was established through ion-exchange reaction in between $Pb(NO_3)_2$ and MAI, while, the second step is the formation of perovskite layer (from $PbI_2$ and MAI). Though, they successfully applied $Pb(NO_3)_2$ layer by spin-casting approach over m- $TiO_2$ film, but the surface morphology and the surface coverage of $PbI_2$ was significantly poor. This surface distortion is because of various ionic radii of the used materials i.e. the reaction between $I^-$ and $NO_3^-$. Therefore, in next step, there were a very poor surface crystallinity and coverages of $MAPbI_3$ perovskite films have been observed as compared with those prepared with spin-coating of $PbI_2$. In order to tackle these problems, we have planned a novel, facile and an efficient strategy to prepare perovskite film morphologies. The synthesis of perovskite layers with halide free lead precursor solution without using spin-casting method is our proposed strategy for an environmentally friendly, cost-effective large surface area device preparation.

In recent days, an attractive strategy has been employed with the implementation of ionic layer adsorption over ZnO film by the reaction of aqueous $Pb(NO_3)_2$, dissolved in water/EtOH green solvents to form PbS based quantum dot layers [28,29]. Therefore, we are interested to synthesize such a unique perovskite surface morphology of $MAPbI_3$ perovskite film by this ionic adsorption from an aqueous $Pb(NO_3)_2$ over a m-$TiO_2$ underneath ZnO interfacial film, and then immersed in MAI solution. We hope that this proposed successive sequential deposition (SSD) approach applied through facile dip-coating method may improve the possibilities of the production of large area perovskite layers from halide-free lead precursor in an aqueous green solvent.

In this study, we demonstrate a facile, low cost, and environmentally friendly method to synthesize efficient perovskite films by simple dip-coating deposition. This was confirmed by successive dipping of a ZnO-covered underneath m-$TiO_2$ film in an aqueous halide-free lead precursor solution and then immersed in MAI solution. This method differs with previously employed spin-coating approach that needs detrimental organic solvents.

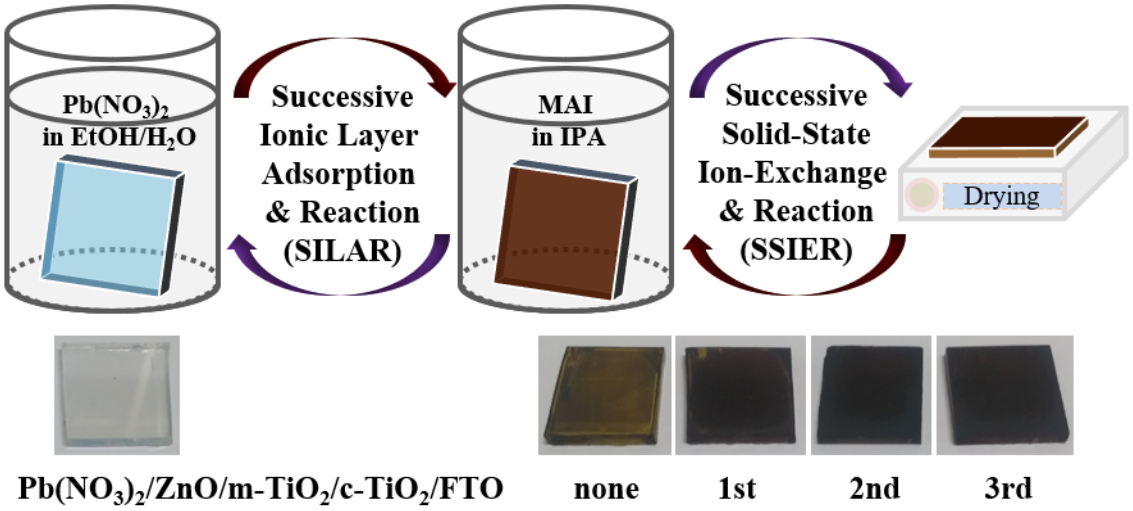


**Figure 1:** Basic scheme to prepare $MAPbI_3$ perovskite layers by successive dipping of ZnO covered m-$TiO_2$/c-$TiO_2$/FTO substrates in aqueous halide-free $Pb(NO_3)_2$ precursor solution, followed by dipping in MAI solution. The as-prepared electrodes pictures are also added after sequential SSIER repetitions, and annealing for 10 mints at room temperature.

Here, we realize that the ZnO interfacial layer rapidly shows substantial adsorption of $Pb(NO_3)_2$. The $MAPbI_3$ perovskite layers was also prepared via $Pb(NO_3)_2$ and $PbI_2$ endures further ion-exchange reactions with the amount of lead nitrate which didn't take part in any reaction, leading towards decomposition to $PbI_2$. Particularly, the successive solid-state ion-exchange and reaction (SSIER) by employing $Pb(NO_3)_2$ layer, helped to improve crystallinity, surface topology, coverage and stability of $MAPbI_3$ layers in-contrast with relatively long-time dipping in MAI solution. Furthermore, the perovskite layers prepared with the collective SSD and SSIER approaches presented superior crystallinity, surface morphology, and coverage related to any approach alone. The PrSCs prepared with sequential deposition of a $MAPbI_3$ perovskite films using an aqueous halide-free $Pb(NO_3)_2$ precursor solution showed PCEs of 12.41%, comparable to those fabricated with conventional spin-coating of halide or non-halide lead precursors. Figure 1 shows a basic scheme for the preparation of the $MAPbI_3$ perovskite films in aqueous halide-free $Pb(NO_3)_2$ and MAI solutions.

## 2. Results and Discussion

### 2.1 Perovskite film formation

To prepare perovskites films, we initially prepared Pb layer, via dipping the substrate into a

$Pb(NO_3)_2$ precursor solution. The SEM images after the adsorption of $Pb(NO_3)_2$, with and with-out a ZnO layer, are shown in figure 2 (a,c), while, in Fig. 2 (b,d) the as-prepared $MAPbI_3$ perovskite films prepared when the ZnO-free and ZnO-coated substrates were immersed into MAI solution. We selected $Pb(NO_3)_2$ as the halide-free lead source due to its recovering ionic layer adsorption on ZnO surfaces with an aqueous (green solvent) solutions. A thin ZnO films-underneath m-$TiO_2$ layers were employed because these can be readily synthesized by spin-coating or spraying of the sol-gel solution after annealing at 300 °C. Remarkably, a substantial layer adsorption of $Pb(NO_3)_2$ was experienced over ZnO-coated substrate after successive dip-coating approach in an aqueous haide-free $Pb(NO_3)_2$ precursor solution, but insignificant layer adsorption over m-$TiO_2$ films was seen with-out ZnO layer (Fig. 2(a) and (b)).

This extraordinary $Pb(NO_3)_2$ layer adsorption seen on ZnO surface within a quite short time, which can be further modified by altering the lead precursor solution, particularly the employed co-solvent of $H_2O$/ethanol. The uniform adsorption was realized over hydro-phobic ZnO surface compared to those with water-only solvent [30,31]. The adsorption behavior can also be altered by changing the dipping duration. For $MAPbI_3$ perovskite layers prepared by reaction with MAI, and a $Pb(NO_3)_2$ layer was initially synthesized by dipiing in a 0.1 M $Pb(NO_3)_2$ precursor solution, dissolved in $H_2O$/ethanol (1:1, v/v), for 30 s. Fig. 1c and d shows the transparent deposited $Pb(NO_3)_2$ films prepared on ZnO film. These films quickly transformed to dark brown-colored layers when exposure to MAI solution, demonstrating a $MAPbI_3$ perovskite film formation with improved surface morphology and poor surface coverage comparable to those prepared by spin-coating of $MAPbI_3$ precursor solution without any further treatment. Nevertheless, the transparently prepared $Pb(NO_3)_2$ morphologies, which showed minimal adsorption over pristine m-$TiO_2$ film, transformed to pale orange-colored layers with $MAPbI_3$ perovskite crystal lumps grownup sparsely over the substrate.

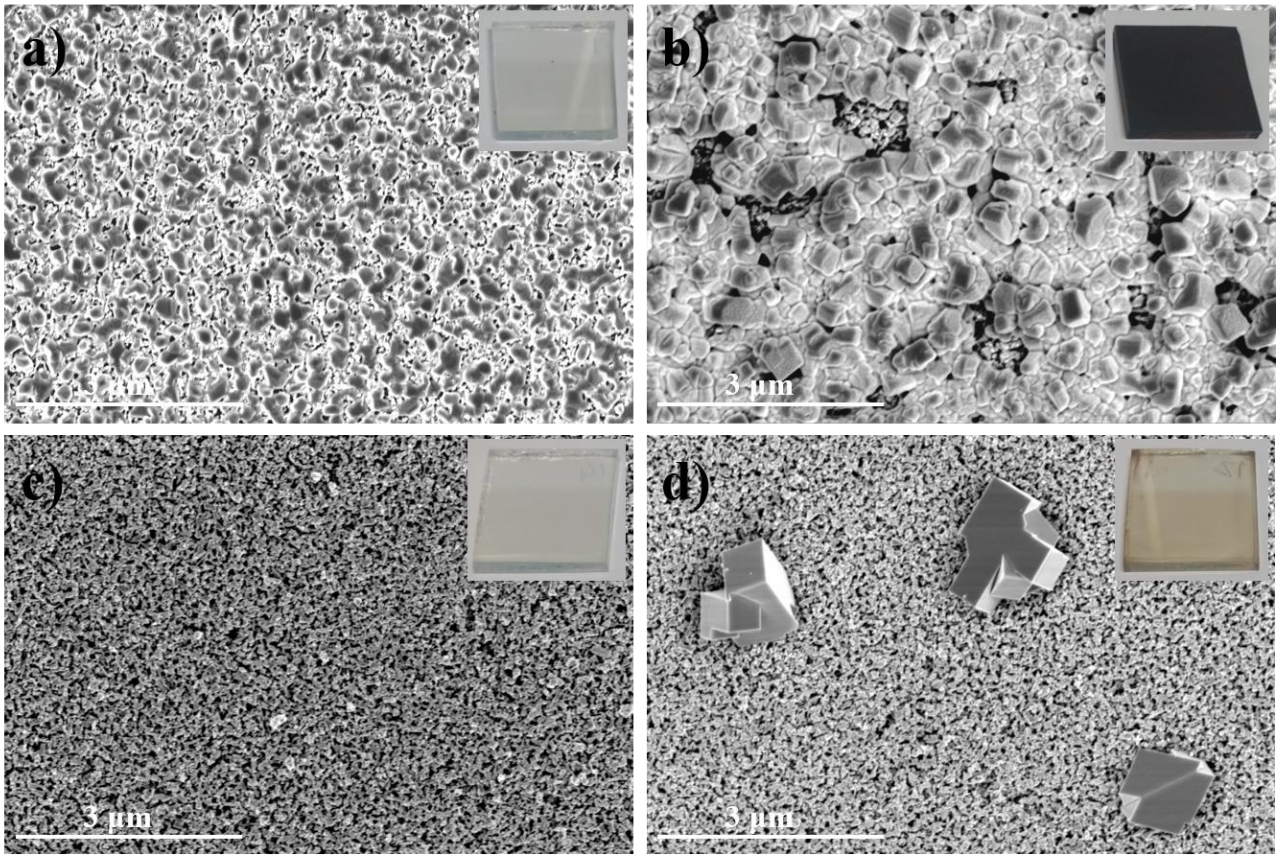


**Figure 2:** SEM images (**a**,**c**) the ionic layer adsorption of $Pb(NO_3)_2$ and (**b**,**d**) the as-prepared $MAPbI_3$ perovskite films prepared after the MAI exposure of the (**a**,**b**) ZnO-coated and (**c**,**d**) ZnO free m-$TiO_2$/c-$TiO_2$/FTO substrates.

These investigations ensures that the sequential strategy based on ZnO adsorption from an aqueous halide-free $Pb(NO_3)_2$ precursor, and the reaction in MAI precursor may facilitates perovskite formation with a cost-effective, simple and unique dip-coating deposition approach. Nevertheless, the $MAPbI_3$ perovskite layers prepared with this method quickly decomposed while, solvent drying process at 80 °C, even less than 20% relative-humidity conditions, the formed appearances into a yellowish colored film leading towards a $PbI_2$ crystalline morphology.

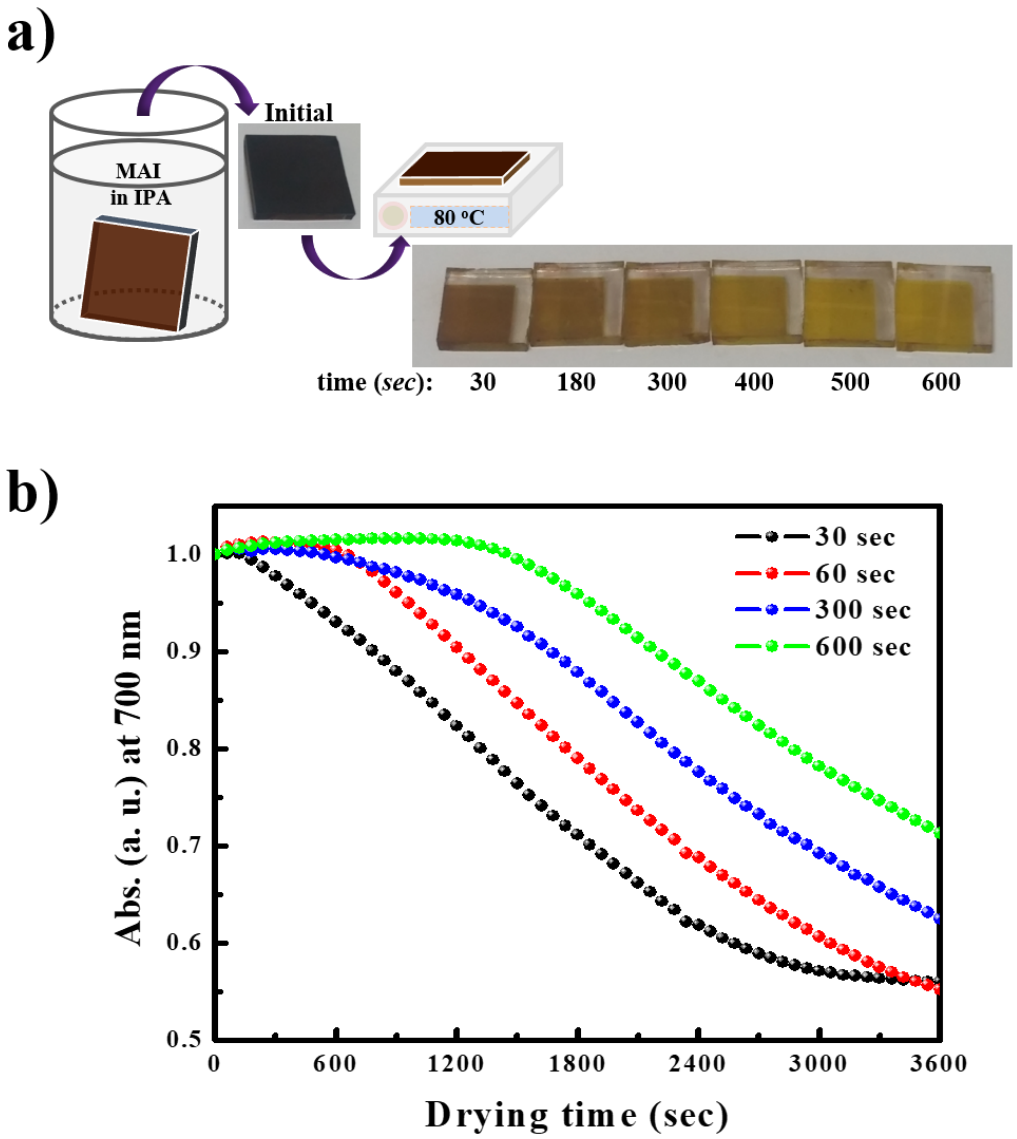


**Figure 3:** Decomposition behavior (**a**) while solvent drying of a $MAPbI_3$ film, prepared with dipping deposition with an aqueous halide-free $Pb(NO_3)_2$ and MAI precursors. The decrease of absorbance (**b**) at 700 nm over 1 h after various MAI solution dipping times (30 (black), 60 (red), 300 (blue), and 600 s (green)).

### 2.2 Decomposition behavior of perovskite film

Figure 3 shows the decomposition behavior while solvent drying of $MAPbI_3$ perovskite morphologies synthesized with successive dipping deposition process. Fig. 3b shows the the decrease of absorbance at 700 nm over 1 h for the $MAPbI_3$ films prepared with numerous MAI precursors after various dipping times (30, 60, 300, and 600 s). Fig. 3a, the film decomposition phenomenon was realized within a quite short interval of time of 30 s and completed after 10

min of constant annealing process at 80 °C. This film degradation was also somewhat seen even in films prepared with a long exposure (600 s) to the MAI solution (Fig. 1).

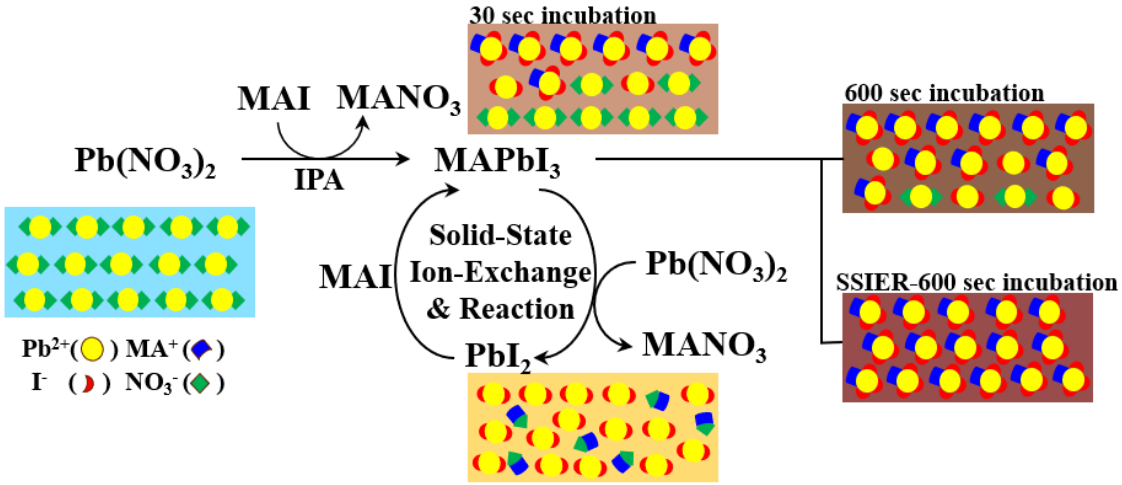


Figure 4: Schematic representation of the designed SSIER methodology for $MAPbI_3$ formation on pre-deposited $Pb(NO_3)_2$ ionic layer.

Therefore, we realized the film degradation behavior rate of the formed morphologies with different dip-coating times by subsequent decrease in absorbance at 700 nm. Though the freshly synthesized $MAPbI_3$ perovskite layers had a quite similar dark brown-color films upon removal from the MAI precursor irrespective of the reaction intervals, the degradation rates were strangely affected with the reaction intervals in MAI precursor solution (Fig. 3b). This directs that the presence of un-reacted $Pb(NO_3)_2$ likely to brings the decomposition behavior for $MAPbI_3$ perovskite layers, and the degree of non-reacted $Pb(NO_3)_2$ should affect the film degradation rates. In view of these results, we venture that the $MAPbI_3$ crystals lattice obtained by $Pb(NO_3)_2$ and MAI precursors can took part in an additional ion-exchange reactions between the non-reacted $Pb(NO_3)_2$, even in the solid state, ensuring degradation to $PbI_2$. Consequently, we established an effective approach, represented as SSIER. This technique avoids the disintegration of $MAPbI_3$ perovskite layers into $PbI_2$ by extra ion-exchange reaction in the solid state in between non-reacted $Pb(NO_3)_2$ and the as-prepared $MAPbI_3$.

Figure 4 depicted the schematic illustration of the designed mechanism of SSIER for $MAPbI_3$

perovskite film formation. Firstly, the $PbI_2$ formed by the reaction of $Pb(NO_3)_2$ and MAI at the solid-liquid junction is transformed quickly into $MAPbI_3$, which suffers further reactions with MAI. Though, the continuing diffusion of MAI into the crystalline layer is stuffy from the bulky $MAPbI_3$ perovskite crystals prepared on the film surface, hindering the reaction rate of $Pb(NO_3)_2$ and MAI. Therefore, though the $Pb(NO_3)_2$ layer is uncovered to the MAI solution for a long time, non-reacted $Pb(NO_3)_2$ expected to remains and can persuade the decay of the $MAPbI_3$ perovskite structure. In the meantime, the $Pb(NO_3)_2$ presence inside the layer might be vanished, as shown in Fig. 4. We tried to proficiently achieve highly stable $MAPbI_3$ films without non-reacted $Pb(NO_3)_2$ layers by applying the SSIER process by exposure to 30 s into MAI precursor, and annealed at 80 °C. This signified a single SSIER cycle. With this, no superficial degradation of the $MAPbI_3$ film was seen even after the 3rd SSIER cycle after a total MAI immersing time of 90 s. The $MAPbI_3$ crystal structures obtained with and with-out SSIER repetition were also specifically compared.

**2.3 Characterization of perovskite film**

The specific investigations regarding the SSIER process was successfully achieved as shown in Fig. 5. The SEM surface topologies images are shown in fig. 5 (a-d) with their conforming pictures (inset) and Fig. 5b shows XDR spectrum for MAPbI3 perovskite films prepared by SSIER repetitions for a total MAI exposure time of 690 s. The co-relation between the perovskite materials conversion and SSIER reiteration time is depicted in Fig. 5f. These perovskite layers were annealed at 80 °C for 10 min to completely eliminate the solvent. We employed a $Pb(NO_3)_2$ ionic morphology deposited by dipping in an aqueous halide-free $Pb(NO_3)_2$ solution for 30 s and annealed at 120 °C to dry the deposited film.

Fig. 5a, depicted that even yet these $Pb(NO_3)_2$ layers were exposed for 690 s to MAI precursor with various SSIER cycles, followed by one long dipping, the surface morphologies of the formed $MAPbI_3$ layers was expressively affected by increasing the number of SSIER cycles. The degradation of $MAPbI_3$ layers was moderately realized after the first repetition, and the morphologies synthesized with no SSIER cycles. The $MAPbI_3$ perovskite layers prepared after 2 SSIER repetitions presented improved stability (inset of Fig. 5a) compared to the 0 and 1 cycle perovskite layers. Furthermore, with more successive SSIER repetitions, the surface morphology, coverage and crystallinity of the $MAPbI_3$ perovskite layers significantly

improved, as shown by the SEM images and XRD patterns (Fig. 5a and b), respectively. Similarly, on the basis of XRD patterns, the conversion rate of $MAPbI_3$ ($CMAPbI_3$) could be qualitatively defined employing the specific peak intensities of $PbI_2$ and $MAPbI_3$ at $2\theta = 12.7°$ and 14.2°, respectively [7,31,32].

$$C_{MAPbI3} = I_{12.7°}/(I_{12.7°} + I_{14.2°}) \quad (1)$$

As shown in Fig. 5c, by increasing the number of SSIER cycles, a higher conversion ratio for $MAPbI_3$ perovskite films achieved by the transformation of $PbI_2$. These features are quite closely associated to the $PbI_2$ resulting from the ion-exchange reactions with the $MAPbI_3$ materials and the non-reacted $Pb(NO_3)_2$ in the solid-state. It should be cleared that the SSIER process can provide improved stability and also enhanced the surface coverage and crystallinity of $MAPbI_3$ perovskite morphologies.

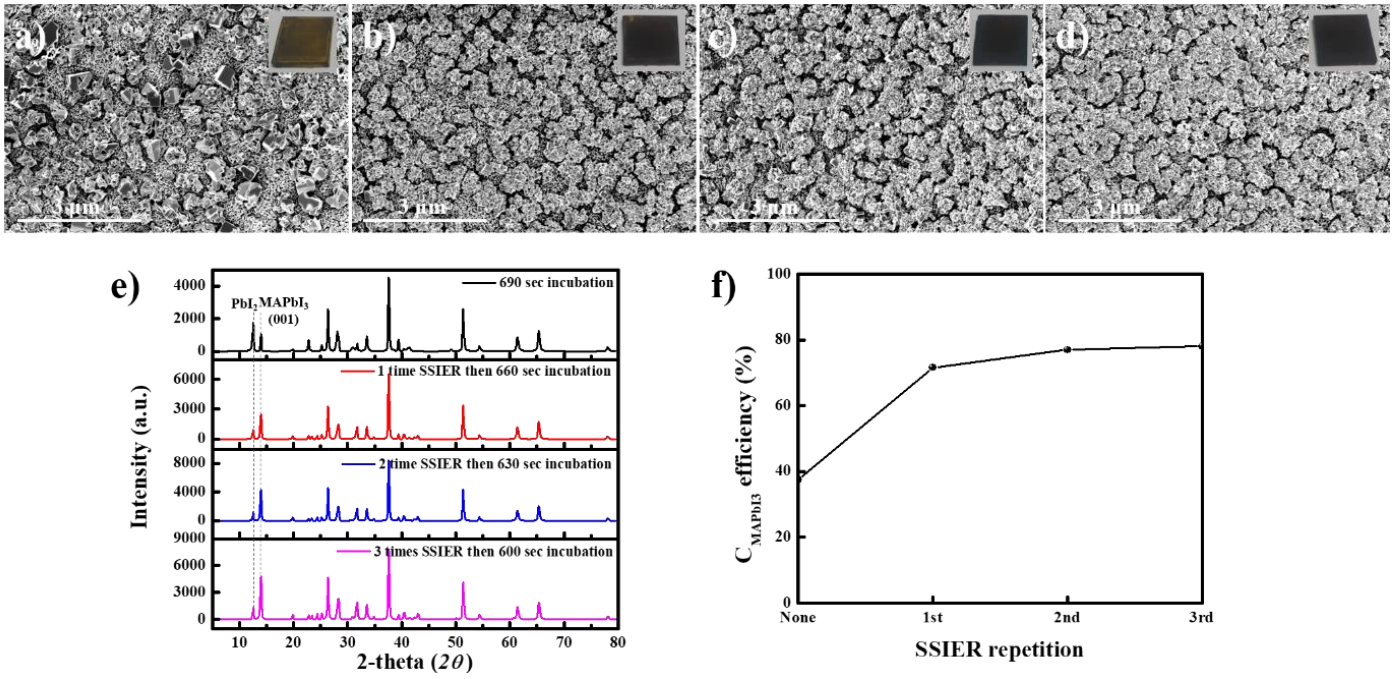


**Figure 5:** (a–d) The SEM images with corresponding pictures (inset) and (**e**) XDR patterns of the $MAPbI_3$ perovskite films prepared by successive SSIER cycles for a total MAI contact time of 690 s. (**f**) The relationship between the perovskite conversion and various SSIER cycles.

Even though the SSIER cycles presented a well-developed and an organized surface coverage,

morphology, crystallinity, and stability, rather sparse surface morphologies on the ZnO/m-$TiO_2$/c-$TiO_2$/FTO glass substrates, as shown in Fig. 5a. Insufficient surface morphologies can lead towards an interfacial recombination happened between metal oxides and hole transporting materials (HTMs), resultant in the poor photo-voltaic performances of PrSC devices. Therefore, a denser surface crystallinity with the $MAPbI_3$ perovskite layers was tried by presenting the SSD approach in addition to the SSIER process. Subsequently, the SSD approach has been employed for the step-by-step progress of nano-scale quantum dot layers [9], we anticipated that the $MAPbI_3$ perovskite formation synthesized via SSD cycles could efficiently enhance the sparse surface coverages. Herein, the $Pb(NO_3)_2$ films was synthesized by dipping an halide-free aqueous solution for 30 s, and then drying the solvent at 120 °C. Then, the prepared films were immersed into MAI precursor solution for a 30 s to initiate the $MAPbI_3$ perovskite formation by annealing the substrates at 80 °C. The above-mentioned process denoted as single SSD cycle.

Therefore, the surface images of the $MAPbI_3$ perovskite films prepared with conventional SSD approaches by (a–c) ionic-layer adsorption of $Pb(NO_3)_2$ from an aqueous halide-free precursor and (d–f) reaction in MAI precursor solution, shown in Fig. 6. The XRD patterns of the $MAPbI_3$ perovskite films and the correlation pattern in between the perovskite materials conversion and various SSD cycles are also shown in Fig. 6g.

Fig. 6a–c, shows when freshly prepared $MAPbI_3$ electrodes were immersed into an aqueous $Pb(NO_3)_2$ solution, the water quickly dissolved and completely removed the MAI materials from the $MAPbI_3$ perovskite structure, leaving a pure $PbI_2$ morphology. Therefore, due to this process a new layer of $Pb(NO_3)_2$ was instantly adsorbed on the surface of the ZnO. Stimulatingly, more obvious platelet morphologies of $PbI_2$ were seen by increasing the numbers of SSD repetitions. In addition, there is a little increase in adsorption layer thickness was realized with the addition of $Pb(NO_3)_2$, even when relating the layers after several SSD cycles to those with only the first adsorption film. This specifies that the extra $Pb(NO_3)_2$ is mainly adsorbed over ZnO/m-TiO2/FTO substrate, due to hydro-phobicity of the $PbI_2$ layers appeared while diminishing MAI in an aqueous precursor solution.

The $MAPbI_3$ perovskite layers were specifically synthesized via 3 SSIER repetitions followed by a final one long time incubation for 600 s in MAI precursor solution after each repetition of

$Pb(NO_3)_2$ ionic-layer adsorption (Fig. S4). Fig. 6(d–f) shows the higher numbers of SSD cycles results in improved surface morphology, crystallinity and coverage of the $MAPbI_3$ perovskite layers formed on the FTO glass substrate. After the 3rd successive SSD repetitions, there were quite less pin-holes appearances found in the $MAPbI_3$ perovskite morphologies in-contrast with those prepared with two or fewer repetitions. It is obvious that the $MAPbI_3$ perovskite layers formed by the successive SSD cycles can efficiently enhance the sparse surface coverages on the ZnO/m-$TiO_2$/c-$TiO_2$/FTO. With respect to XRD patterns, the conversio of $MAPbI_3$ (*C*$MAPbI_3$) is self-determining of the 1st to 3rd SSD cycles, but expressively decreased after the 4th SSD cycle, as shown in Fig. 6h. These outcomes show that the crystallinity of the $MAPbI_3$ perovskite layers is greatly affected by the SSIER approach, not the SSD approach. Moreover, SSIER process might not be an efficient for perovskite materials crystal growth process after the 4th SSD cycle.

**2.4 Photovoltaic performance**

Figure 7a displays the current–voltage (*J*–*V*) curves for PrSCs based on $MAPbI_3$ perovskite films prepared with chosen number of SSD cycles followed by SSIER repetitions along-with one long final dipping for 600 s in MAI solution. Furthermore, the hysteresis phenomenon of PrSCs prepared under fully optimized environments (3 SSD and 3 SSIER cycles, 600 s MAI incubation) are shown in Fig. 7b. The PrSCs were prepared with an n-i-p device structure of FTO/c-$TiO_2$/m-$TiO_2$/ZnO/$MAPbI_3$/HTM/$MoO_3$/Ag. The specific conductivity of spiro-MeOTAD and the effectiveness of the HTM was enhanced by adding different doping additives such as 4-tert-butylpyridine (t-BPy) and lithium bis(trifluoromethanesulfonyl) imide (Li-TFSI). The specific optimization of the fabricated perovskite device performance is shown in Figs S5–9.

Fig. 7a shows the optimized PrSC devices showed the most competent PCE (maximum/average) of 12.41/11.58% with a short-circuit current density (*J*sc) of 21.53 mA/cm−2, an open-circuit voltage (*V*oc) of 0.93 V, and a fill factor (*FF*) of 0.62. The PCEs of the devices based on MAPbI3 perovskite layers fabricated with different numbers of SSD cycles were not as high. One SSD cycle gave PCEs (maximum/average) of 8.73/7.01% with *J*sc = 14.66 mA·cm−2, *V*oc = 0.98 V, and *FF* = 0.61; two cycles gave PCEs of 9.07/8.05% with *J*sc = 15.00 mA·cm−2, *V*oc = 0.96 V, and *FF* = 0.63; and four cycles gave PCEs of 10.16/8.05% with *J*sc = 17.00

mA·cm−2, *V*oc = 0.98 V, and *FF* = 0.61. These outcomes can be described with enhanced surface morphologies, coverages and crystallinity of the perovskite layers prepared with sequential deposition with 3 SSD and 3 SSIER repetitions, as shown in Fig. 4. Furthermore, the optimized PrSCs presented much higher device performances as compared with those based on non-halide solutions such as $Pb(OAc)_2$ and $Pb(ClO_4)_2$ (Fig. S10).

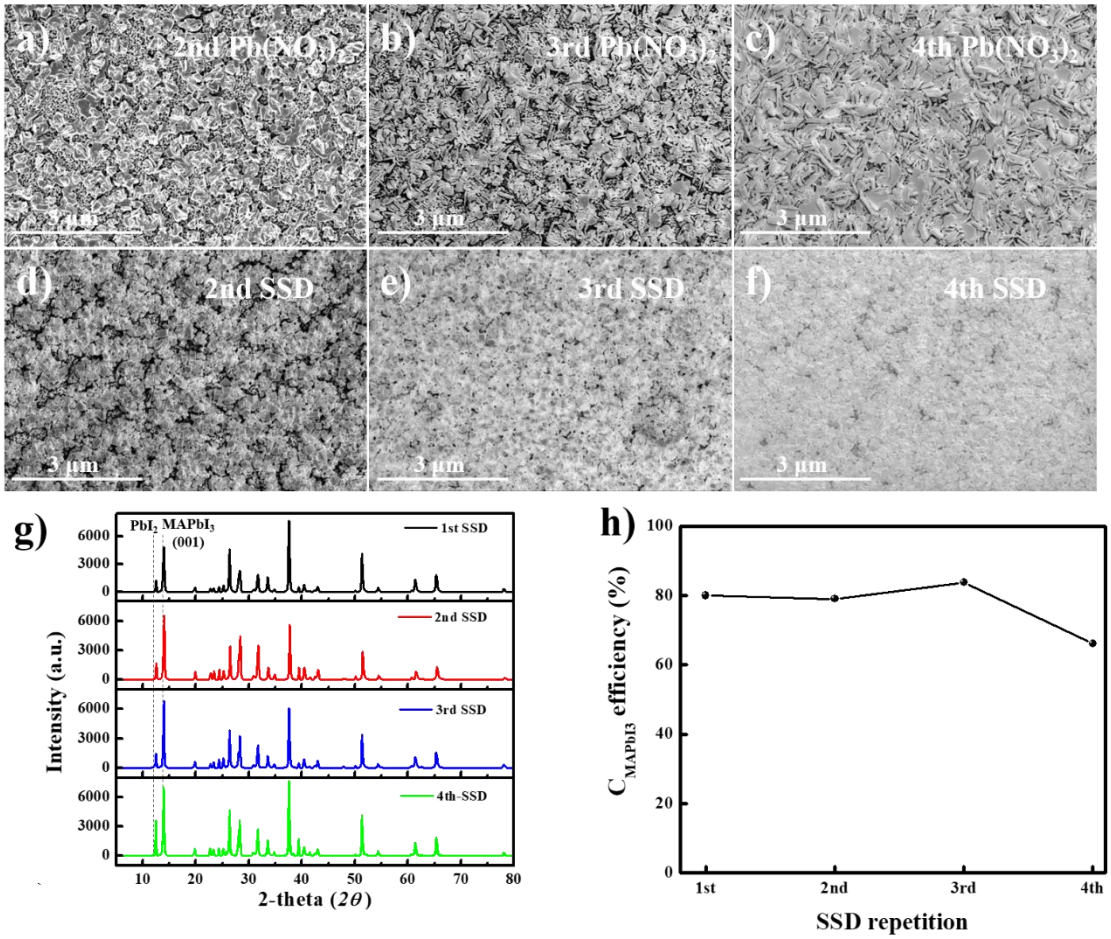


**Figure 6:** (a–f) The SEM images of the MAPbI3 morphologies prepared with conventional SSD approach via (a–c) ionic layer adsorption of $Pb(NO_3)_2$ from an aqueous precursor solution followed by (d–f) the exposure in MAI. (**g**) The XDR patterns of the $MAPbI_3$ perovskite films and (h) the correlation between the perovskite materials conversion and SSD repetition time.

Particularly, the typical n-i-p PrSCs films synthesized with the m-$TiO_2$ electrode frequently shows hysteretic *J-V* phenomenon which mainly depends upon scan direction (reverse or forward) because of various charge extraction or transference rates of holes and electrons

detached from excitons [10]. Fig. 7b depicted the hysteresis behavior of the *J-V* curves in both scan directions for the fabricated champion PrSCs device. The hysteresis phenomenon of the PrSCs are depicted in Fig. 7b and the related values are concise in Fig. S11 and Table S1. Most of the fabricated perovskite devices displayed insignificant alterations in *J*sc and *V*oc values in both scan directions, but the *FF* values were knowingly condensed in the forward scan direction. However, the average of the PCE values gained in both the scan directions was around 6% lower than the PCE value in the reverse scan direction, ensuring good external quantum efficiency (EQEs) in the light absorption region (Fig. S12).

**2.5 Large surface area perovskite films**

Subsequently, we specifically prepared and characterize the cross-sectional surface morphology of the most optimized PrSC device (under the best optimized condition). Figure 8a depicts the SEM surface morphology of a cross-sectional image of the PrSC device prepared with 3 SSD and 3 SSIER repetitions with a one long final dipping for 600 s in MAI precursor solution. For this, a ∼100 nm thin section was characterized with the focused ion beam (FIB) technique to realize the vertically aligned perovskite morphologies and various interfacial hetero-junction's layers between the $MAPbI_3$ perovskite material, ZnO, and m-$TiO_2$/c-$TiO_2$ electrodes.

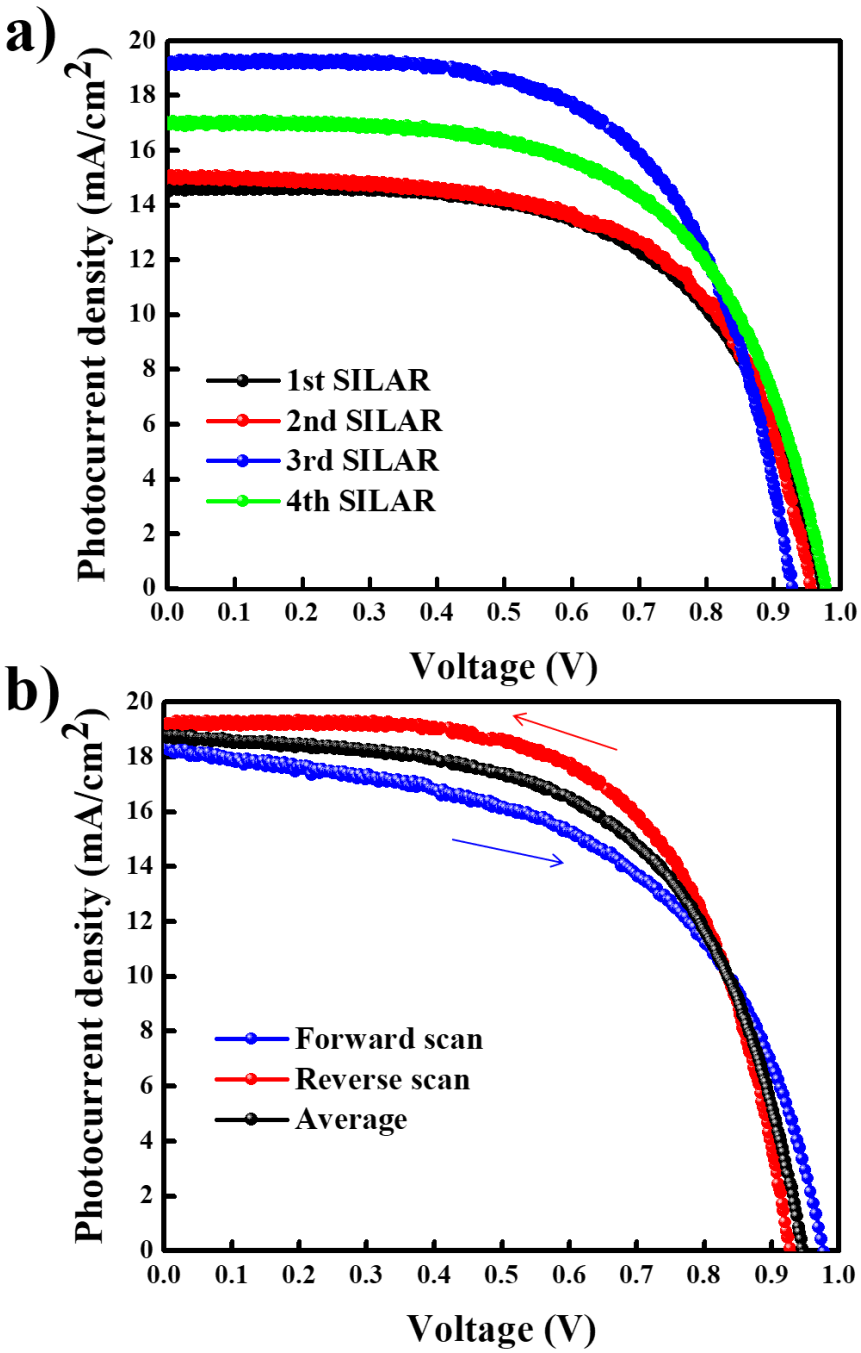


**Figure 7:** (a) Current-voltage (*J-V*) curves for PrSCs based on $MAPbI_3$ perovskite films synthesized with an optimized number of SSD cycles followed by 3 SSIER repetitions, with a one long final dipping for 600 s in MAI precursor solution. (b) The hysteresis phenomenon of the PrSCs prepared under the best optimized conditions (3 SSD and 3 SSIER processes, 600 s MAI incubation).

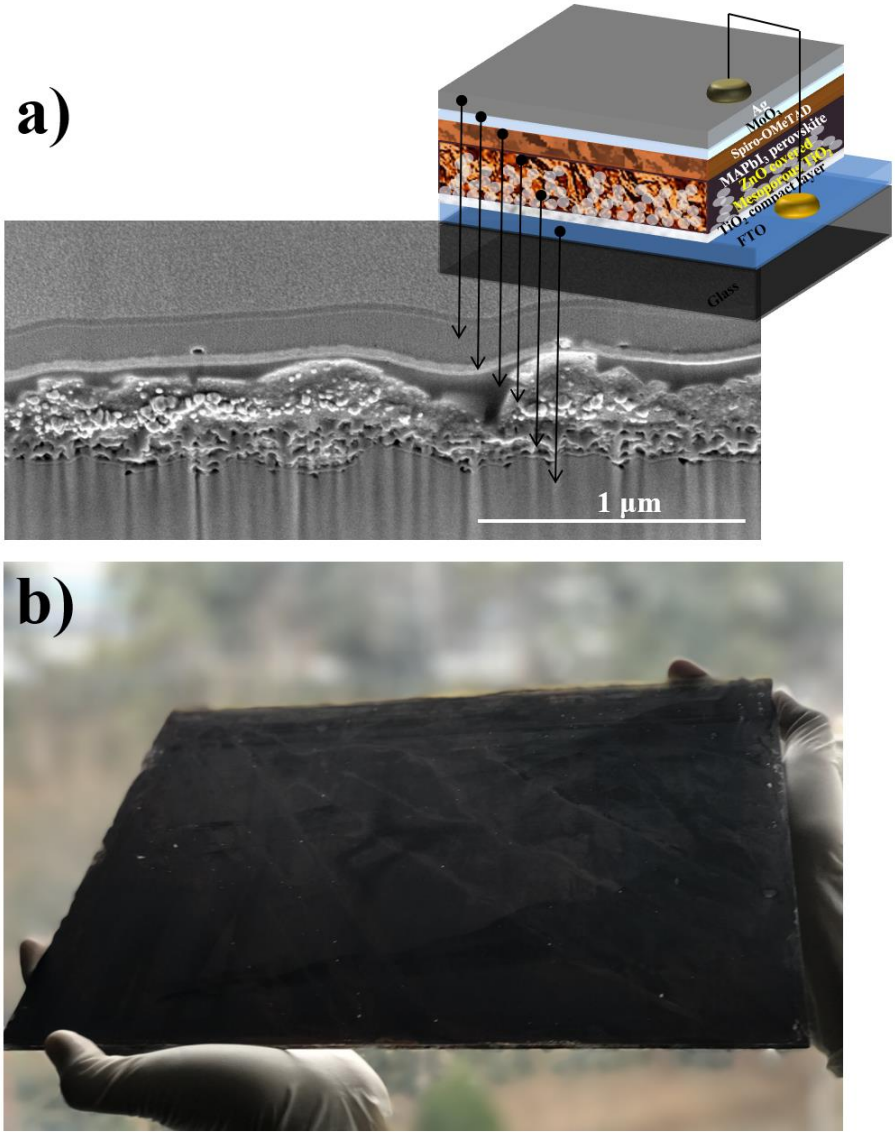


**Figure 8:** (a) The SEM cross-sectional image of the fabricated perovskite device using 3 SSDs and 3 SSIER cycles with a one long final dipping of 600 s in the MAI precursor solution. (**b**) Photograph of a specially prepared large area $MAPbI_3$ perovskite layers synthesized with sequential SSD and SSIER deposition on large area glass substrate of 780 cm2 (30 cm (width) × 26 cm (height)).

Fig. 8a shows the $MAPbI_3$ perovskite films was well prepared between the spiro-MeOTAD HTM and ZnO/m-$TiO_2$/c-$TiO_2$/FTO glass substrate without any interfacial dead spaces. Nevertheless, the layer was non-uniform and quite thin with a thickness of approximately 250 nm, as compared with the high efficiency PrSCs reported earlier. Here, we synthesize a large

area perovskite layer with a sequential dipping deposition process with a halide-free lead precursor in an aqueous precursor solution to simplify a green and cost-effective manufacturing approach. The photograph in Fig. 8b depicts the $MAPbI_3$ perovskite layers prepared with a sequential SSD and SSIER deposition process on large area glass substrates. To establish a large area $MAPbI_3$ perovskite layer, we synthesize a thin ZnO layer on a bare FTO substrate of 780 cm2 (30 cm × 26 cm, width × height) by employing the dipping approach. After that, the $MAPbI_3$ perovskite layers were deposited with the sequential SSD and SSIER process. Beside this that the large area production of $MAPbI_3$ perovskite layers was not a so smooth because of the uneven surface coverages of the ZnO under layer, we efficiently investigated a large area perovskite layer formation by employing the sequential dipping deposition process with a halide-free lead precursor solution in an aqueous solution (green solvents). This signifies significant development towards environmentally friendly and cost-effective manufacturing approach for large area PrSCs formation.

**3. Conclusion**

We have established an effective process to prepare large area $MAPbI_3$ perovskite layers by employing sequential dipping deposition process with ionic-layer adsorption of $Pb(NO_3)_2$ in aqueous halide-free solvent along-with the reaction of MAI. This denotes momentous development toward an environmentally benevolent and cost-effective engineering approach for the preparation of large area PrSCs. Particularly, the ZnO interfacial layer persuaded substantial adsorption of $Pb(NO_3)_2$ from an aqueous solution within a very short interval of time. For this, a modified SSIER process was established to avoid the disintegration of $MAPbI_3$ perovskite materials designed from $Pb(NO_3)_2$ and MAI, which was quickly captured the route of ion-exchange reactions with non-reacted $Pb(NO_3)_2$ even in the solid-state. The technique established herein afforded improved stability, surface crystallinity, coverage, and morphology of $MAPbI_3$ perovskite layers in-contrast with those fabricated without the SSIER approach. Furthermore, the introduction of the SSD approach to the SSIER process led towards more complete and adhere surface coverage with the $MAPbI_3$ perovskite layers affording enhanced surface morphology, device stability, and crystallinity of the perovskite layers. The PrSCs based on these sequential depositions of the $MAPbI_3$ perovskite films by employing an aqueous halide-free $Pb(NO_3)_2$ precursor solution presented outstanding PCEs of 12.41%, which is

equivalent to films prepared from spin-coating approach of halide or non-halide lead solutions. The outcomes of this study lay the foundation for the progress of environmentally friendly and cost-effective manufacturing process of highly efficient and large area PrSCs devices.

# Chapter 4

## *Dip-coating deposition of highly-efficient (CH3)3NPbI3_xClx based perovskite materials*

## 1. Introduction

Recently, the use of organic–inorganic lead halide perovskite materials has attracted signi cant attention owing to the excellent power conversion efficiencies (PCEs) of perovskite solar cells (PrSCs), which have been proposed as potential alternatives for conventional silicon solar cells.1,2 Particularly, alkylammonium lead halides such as (RNH3)PbX3 (R ¼ alkyl, X ¼ Cl, Br, I), when used as direct-band-gap materials, manifest exceptional electron/hole conduction and photosensitizer performances by occupying the hybrid organic–inorganic perovskite cores to provide promising high PCEs in PrSCs.3,4 These perovskite materials have been developed extensively using a variety of deposition strategies listed as follows: (1) the spin casting of the lead source PbX2 followed by reaction with an alkylammonium halide such as an methylammonium iodide (CH3NH3I, MAI) by dipping in a solution, spin casting, or vacuum deposition5,6 and (2) direct spin-casting of a perovskite precursor solution with thermal annealing, interfacial engineering, solvent engineering, or adducts.7,8 However, the spin casting deposition techniques of perovskite materials frequently limit the substrate size, causing a reduction in the active area. Toxicity due to high-polar aprotic organic solvents, e.g., dimethyl formamide and dimethyl sulfoxide, which are used due to the poor solubility of lead halide precursors is also an important issue.

Very recently, we developed a simple sequential dip-coating (SDC) deposition approach applicable for large areas to fabricate an efficient (CH3NH3)PbI3 (MAPbI3) perovskite film using an aqueous non-halide lead precursor such as Pb(NO3)2, which was employed owing to its good compatibility with environmentally

benign and low-cost non-toxic solvents such as water.9,10 The Pb(NO3)2 layer adsorbed spontaneously on the ZnO substrate by the SDC process leads to a stable and efficient MAPbI3 perovskite crystalline structure from the successive solid-state ion-exchange and reaction (SSIER) with MAI. The MAPbI3 perovskite layers fabricated by this approach have satisfactorily high PCEs in PrSCs. However, it is challenging yet essential for commercial applications to achieve better performances than those obtained by spin-casting deposition. Therefore, we aim to develop a simple dip-coating deposition method for mixed halide-based perovskite materials, especially MAPbI3_xClx, which increased the PCEs to above 20% of that of PrSCs.11 The MAPbI3_xClx perovskite materials bare more attractive owing to their

higher charge carrier mobility and longer charge carrier diffusion length than MAPbI3.3,5,12 These have hitherto been prepared by the reaction of PbI2 and MACl (or PbCl2 and MAI), but currently, the preparation is done by inserting a small amount of Cl in the MAPbI3 perovskite lattice.7,13,14

In this study, we demonstrate a facile, cost-effective, and environmentally benign approach to prepare efficient MAPbI3_xClx perovskite films from aqueous non-halide lead precursors by a simple all-dip-coating deposition process for the first time. This was readily demonstrated by sequentially dipping a thin ZnO/TiO2 bilayer deposited substrate in an aqueous Pb(NO3)2 solution and subsequently, in an MAI and MACl mixed solution. Interestingly, we found that the MAPbI3_xClx perovskite layers deposited via a simple dip-coating process were constructed with a Cl/I ratio below ~3%, indicating the partial insertion of

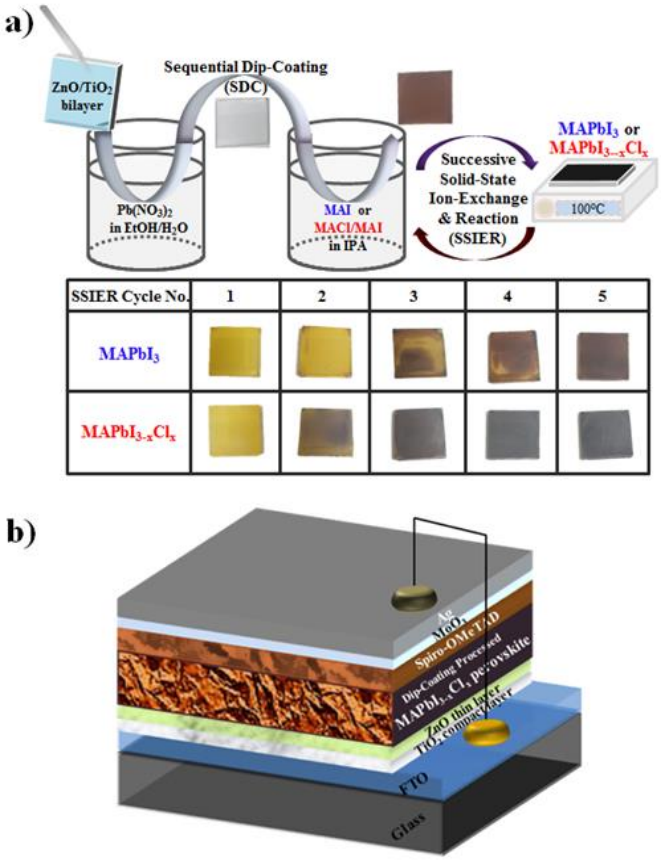


**Figure 1:** Scheme Caption(a) Schematic description of $MAPbI_3$ and $MAPbI_{3-x}Cl_x$ perovskite material deposited by sequentially all-dip-coating in aqueous $Pb(NO_3)_2$ and MAI and MACl/MAI mixed solutions, respectively, followed by repetition of the SSIER process and (b) a PrSC architecture used in this study.

Cl into the MAPbI3 perovskite lattice. The inserted amounts of Cl could be readily modulated by varying the MACl concentration in the MAI and MACl mixed solution. Despite the small amount of Cl incorporation, this might lead to signi cant improvements in the surface morphology and crystallinity of the MAPbI3_xClx perovskite layers compared to those of MAPbI3 fabricated under the same conditions.12,15,16 Consequently, this SDC approach enables the fabrication of the most efficient MAPbI3_xClx perovskite materials with an aqueous non-halide lead precursor, in contrast to the conventional spin-casting approach that uses detrimental organic solvents (DMF and DMSO). The main purpose behind this work is to avoid the toxicity of hazardous DMF and DMSO solvents to dissolve the lead halide precursor and to focus on the usage of aqueous non-halide lead precursor to prepare an efficient perovskite films which didn't obey the restrictions of substrate size.9–19 The PrSC devices with these perovskite films exhibited superior device performances and stabilities, resulting in an outstanding PCE of ~15.3%. Fig. 1 shows (a) a schematic description of MAPbI3_xClx perovskite material deposited by sequentially dipping a ZnO-covered TiO2/fluorine-doped tin oxide (FTO) substrate in aqueous Pb(NO3)2 and MACl/MAI mixed solutions followed by repetition of the SSIER process between annealing at 100 °C and dipping in MACl/MAI mixed solutions and Fig. 1(b) a PrSC architecture used in this study. These are also compared to those of MAPbI3.

## 2. Results and Discussion

For the deposition of the $MAPbI_{3-x}Cl_x$ perovskite layer by a simple dip-coating process, as shown in Scheme 1a, we first fabricated a Pb precursor layer by dipping the substrate in an aqueous $Pb(NO_3)_2$ solution. The $Pb(NO_3)_2$ was unprecedently adsorbed on the ZnO surface and then rapidly changed to dark brown-colored films upon exposure to the MAI solution and MACl/MAI mixed solution even in a very short time of 30 s, indicating the formation of $MAPbI_3$ and $MAPbI_{3-x}Cl_x$ perovskite materials, respectively. However, these perovskite films rapidly decomposed, showing a change to a yellowish film corresponding to the crystalline morphology of $PbI_2$ during solvent drying at 100°C, even below 20% relative humidity. We have speculated that $MAPbI_3$ and $MAPbI_{3-x}Cl_x$ perovskite materials could participate in ion-exchange reactions between the unreacted $Pb(NO_3)_2$ even in the solid state, and this is defined

as the SSIER process.[9,10] We attempted to efficiently achieve more stable perovskite layers by applying SSIER cycles. Interestingly, we found that the perovskite film fabricated via repetitive SSIERs in MACl/MAI mixed solution exhibited much darker blackish color compared to that in MAI solution, as shown in Scheme 1. This seemed to be a different perovskite material with the $MAPbI_3$ perovskite structure that forms upon exposure to the MAI solution of the $Pb(NO_3)_2$ layer. Therefore, in this study, we prepared three types of MACl and MAI mixture solutions: 0.45-MACl/MAI, 0.75-MACl/MAI, and 0.90-MACl/MAI by adding MACl of 0.045, 0.075, and 0.090 M, respectively, in MAI solution of 0.1 M, which were compared to those in MAI solution without MACl. The perovskite material layers fabricated by a simple dip-coating process using these MACl/MAI mixed solutions presented much better stability without decomposing into $PbI_2$ as of five SSIER cycles, as shown in Figure S1-S4.

Figure 1 shows the (a, b) ultraviolet (UV)-vis absorption and (c) photoluminescence (PL) spectra for $MAPbI_3$ and $MAPbI_{3-x}Cl_x$ perovskite material films deposited on ZnO/c-TiO2/FTO, in which simple all-dip-coating approaches were used under the five SSIER cycles. These films show the typical absorption behaviors of $MAPbI_3$ and $MAPbI_{3-x}Cl_x$ perovskite materials with onset points in the vicinity of 790 nm (optical band gap < 1.5 eV). The higher MACl concentration in the MACl/MAI mixture led to darker blackish-colored and turbid perovskite films, thereby providing nonuniform absorption behavior by light scattering in the UV-vis spectra shown in Figure 1a. All $MAPbI_{3-x}Cl_x$ perovskite materials prepared in the MACl/MAI mixed solution seemed to exhibit a higher light-absorption efficiency at a wavelength of 750 nm than MAPbI3 subjected to the MAI solution when their baselines were adjusted to a ~850 nm. (Figure 1b), indicating better crystalline morphology of perovskite films. Also, all $MAPbI_{3-x}Cl_x$ perovskite materials prepared in the MACl/MAI mixed solution exhibited the lower PL intensities than $MAPbI_3$ subjected to the MAI solution as shown in Figure 1b. This indicates that perovskite materials prepared in the MACl/MAI mixed solutions show better charge transfer into the ZnO/c-$TiO_2$ ETL layer than those in the MAI solution.

Meanwhile, the PL intensities of their perovskite films were significantly affected by the MACl concentration of the MACl/MAI mixed solution. Interestingly, it was observed that the perovskite materials prepared in 0.75-MACl/MAI presented lower PL intensities compared to those prepared with 0.45-MACl/MAI and 0.90-MACl/MAI. These results indicate that the

perovskite materials deposited by a simple all-dip-coating process in aqueous $Pb(NO_3)_2$ solution and MACl/MAI mixed solution might have the characteristics of $MAPbI_{3-x}Cl_x$ perovskite structure in which the Cl composition is closely related to the MACl concentration. Therefore, we investigated the surface morphologies, crsytallinity, and atomic compositions of these perovskite material films. Figure 2 shows field emission scanning electron microscope (FESEM) images of the surface morphologies of $MAPbI_3$ prepared in (a) MAI and $MAPbI_{3-x}Cl_x$ perovskite materials prepared in (b) 0.45-MACl/MAI, (c) 0.75-MACl/MAI, and (d) 0.90-MACl/MAI, respectively, under the same conditions. They could be compared with those of the (e) $Pb(NO_3)_2$ layer adsorbed on (f) ZnO/c-$TiO_2$/FTO substrat

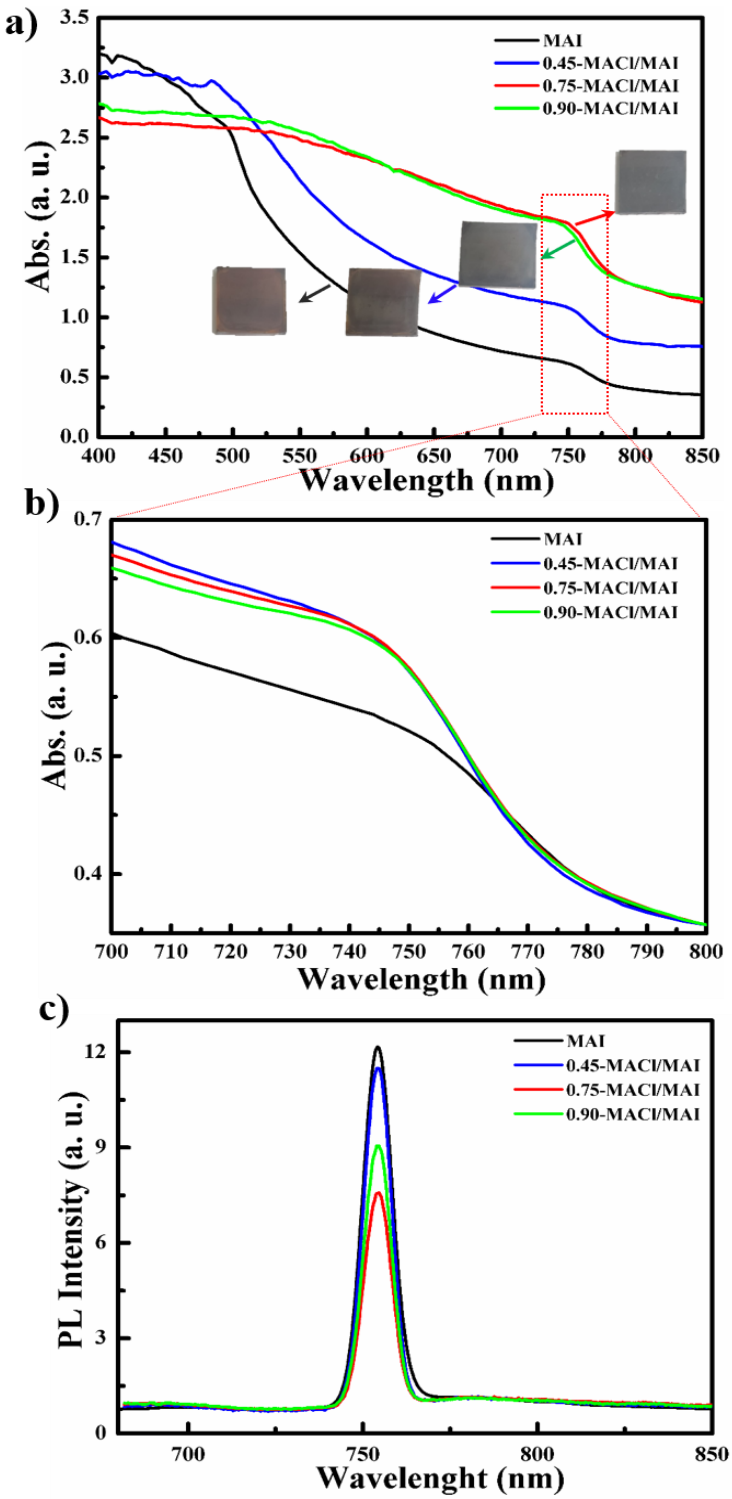


**Figure 2:** (a, b) UV-vis absorption and (c) photoluminescence (PL) spectra for $MAPbI_3$ and $MAPbI_{3-x}Cl_x$ perovskite material films deposited on ZnO/c-$TiO_2$/FTO, in which simple all-dip-coating approaches were used under the five SSIER cycles.

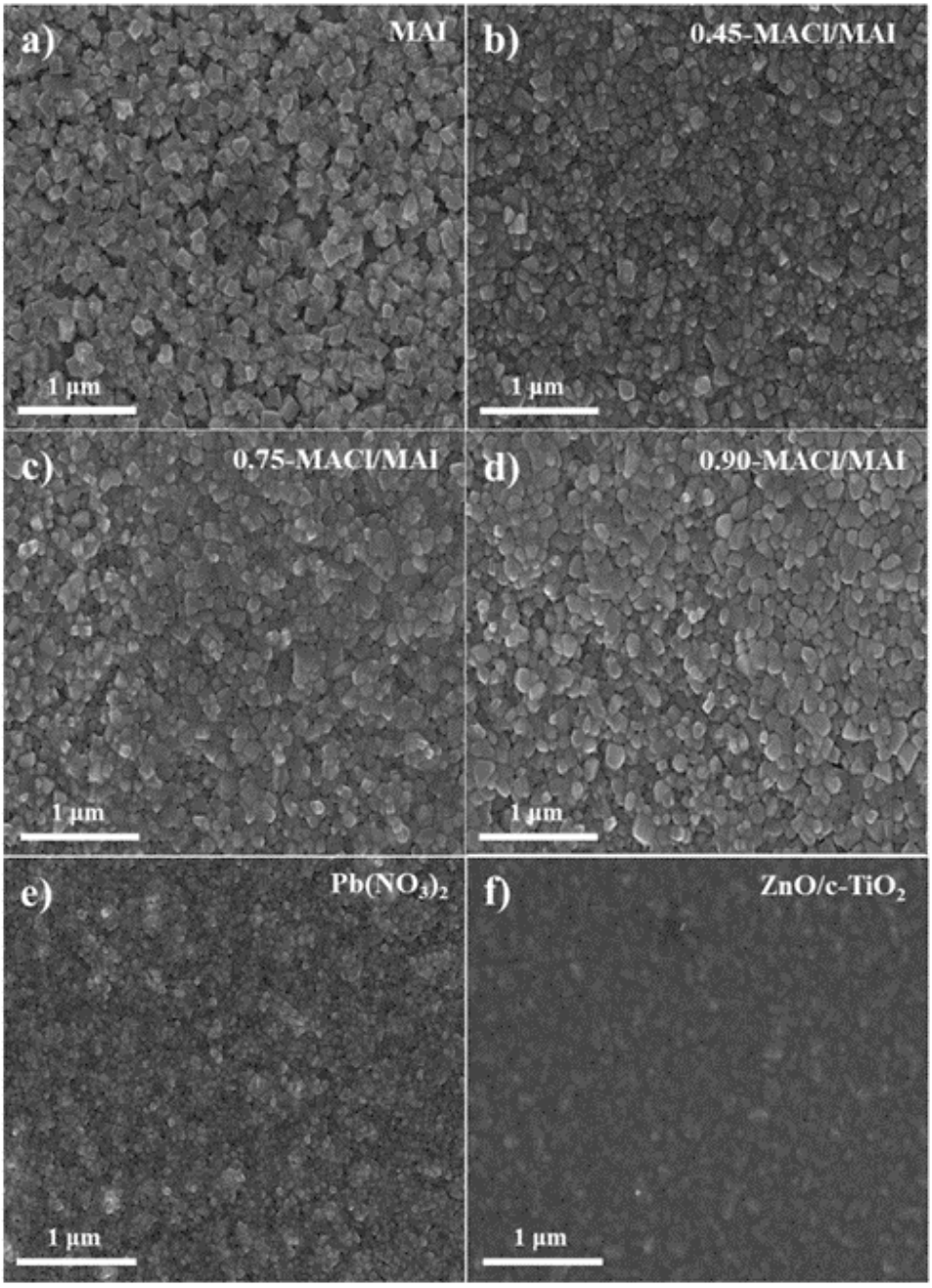


**Figure 3:** FESEM images of the surface morphologies of $MAPbI_3$ prepared in (a) MAI and $MAPbI_{3-x}Cl_x$ perovskite materials prepared in (b) 0.45-MACl/MAI, (c) 0.75-MACl/MAI, and (d) 0.90-MACl/MAI, respectively, under the same conditions, and (e) $Pb(NO_3)_2$ layer adsorbed on (f) ZnO/c-$TiO_2$/FTO substrate.

The $Pb(NO_3)_2$ deposited by dipping into an aqueous $Pb(NO_3)_2$ solution presented well surface coverage with a particulate morphology on the ZnO/c-$TiO_2$/FTO substrate (Figure 2e). As shown in Figure 2a, the $MAPbI_3$ perovskite film fabricated via SDC of this $Pb(NO_3)_2$ layer in MAI solution followed by five SSIER cycles exhibited a structural morphology with submicron-sized cubic-like crystal lumps grown from $Pb(NO_3)_2$, but it shows distinct grain boundaries and rather sparse surface coverages on ZnO/c-$TiO_2$/FTO substrates. The grain boundaries can interrupt efficient charge transport, and inadequate surface coverage can lead to interfacial recombination between the metal oxides and and hole transporting material (HTM), resulting in the poor performance of PrSC devices.

Meanwhile, the $MAPbI_{3-x}Cl_x$ perovskite materials fabricated with 0.45-MACl/MAI, 0.75-MACl/MAI, and 0.90-MACl/MAI exhibited a more-blunt structural morphology with a well-adhering grain boundary and much better complete surface coverage than $MAPbI_3$ prepared under the same conditions as shown in Figure 2, thereby providing better performance of PrSC devices.

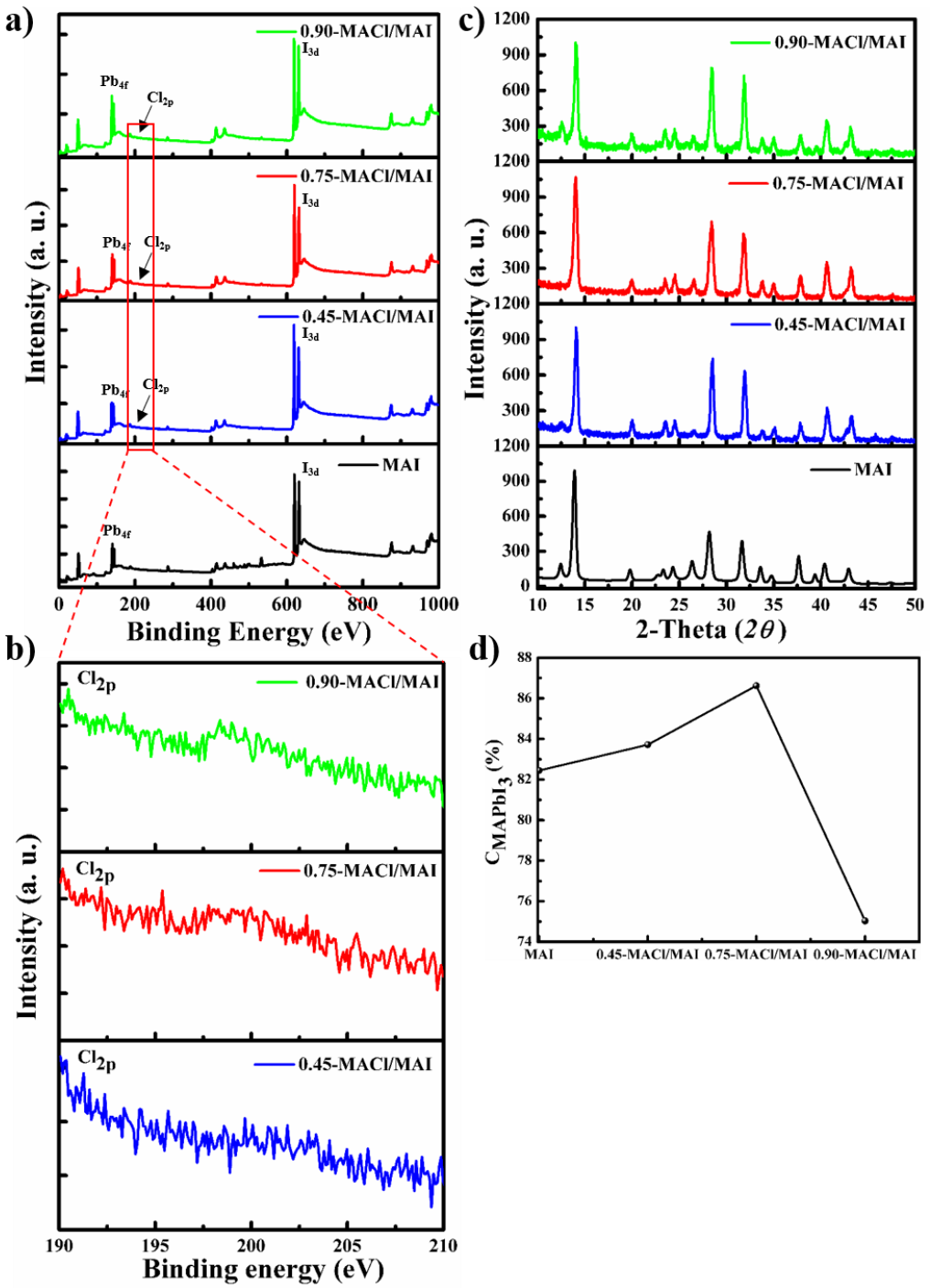


**Figure 4:** (a) XPS spectra and (b) XRD patterns of $MAPbI_3$ prepared with MAI (black line) and $MAPbI_{3-x}Cl_x$ perovskite materials prepared with 0.45-MACl/MAI (blue line), 0.75-MACl/MAI (red line), and 0.90-MACl/MAI (green line), respectively and (c) Cl 2p spectra in $MAPbI_{3-x}Cl_x$ perovskite materials (b) correlated their perovskite conversions.

To clarify the origin of these variation in the surface morphology, X-ray photoelectron spectroscopy (XPS) and X-ray diffraction (XRD) analyses were carried out to investigate the superficial chemical composition and crystallinity. (Figure 3) Figure 3a shows the XPS spectra of $MAPbI_3$ prepared in MAI (black line) and MAPbI3-xClx perovskite materials prepared in 0.45-MACl/MAI (blue line), 0.75-MACl/MAI (red line), and 0.90-MACl/MAI (green line), respectively. All the perovskite materials show common peaks at 143 (and 138) and 616 eV, which correspond to the peak Pb 4f5/2 (4f7/2) and I 3d.[4,16,18] Interestingly, in the case of $MAPbI_{3-x}Cl_x$ perovskite materials, an additional signal was detected at 198~202 eV for Cl 2p, as clearly seen even at very low intensities from the XPS, as shown in Figure 3c. Furthermore, the elemental quantitative data of Pb, I, and Cl were obtained from XPS, which is summarized in Table S1. The Cl-contents in $MAPbI_{3-x}Cl_x$ perovskite materials were determined to b 0.63, 1.18, and 3.14% (%ratio of Cl/I) in 0.45-MACl/MAI, 0.75-MACl/MAI, and 0.90-MACl/MAI, respectively. Although a similar concentration of MACl to that of MAI was adapted in a mixed solution, the low content of Cl in $MAPbI_{3-x}Cl_x$ perovskite materials might be caused by the formation kinetics of $MAPbI_3$ perovskite structure being much higher than that of $MAPbI_{3-x}Cl_x$ perovskite structure.

This might lead to Cl incorporation into $MAPbI_3$ at relatively low concentrations. Additionally, the $MAPbI_{3-x}Cl_x$ perovskite structure fabricated by this SDC approach might be readily modulated using the incorporated Cl content by varying the concentration of MACl in solution mixed with MAI, even as the maximum concentration of Cl that can be introduced into $MAPbI_3$ perovskite through conventional spin-casting method has been limited to below 4% (Cl/I) because of the significant differences in the ionic radii of Cl and I.[19,20]

The XRD patterns of $MAPbI_3$ prepared with MAI (black line) and $MAPbI_{3-x}Cl_x$ perovskite materials prepared with 0.45-MACl/MAI (blue line), 0.75-MACl/MAI (red line), and 0.90-MACl/MAI (green line), respectively and correlated their perovskite conversions. (Figure 3b and 3d) All the XRD patterns of these perovskite materials indicated typical $MAPbI_3$ crystalline structures with an intense peak of (100) at $2\theta = 14.2°$[21] and no peaks related to the $MAPbCl_3$ perovskite crystal structure at $2\theta = 15.4°$[16] as shown in Figure 3b. This indicates that the $MAPbI_{3-x}Cl_x$ materials fabricated via SDC in aqueous $Pb(NO_3)_2$ solution and in MACl/MAI mixed solution might have perovskite structures inserted partially into the $MAPbI_3$ perovskite

lattice of Cl, like a dopant. Based on the XRD patterns, the conversion of $MAPbI_3$ ($C_{MAPbI3}$) could be qualitatively defined using the peak intensities of $PbI_2$ and $MAPbI_3$ at $2\theta = 12.7°$ and 14.2°, respectively. [21]

$$C_{MAPbI3} = I_{12.7°}/(I_{12.7°} + I_{14.2°}) \quad (1)$$

As shown in Figure 3d, the $C_{MAPbI3}$ values could be dependent on the concentrations of MACl in the MACl/MAI mixed solution. The $MAPbI_{3-x}Cl_x$ perovskite materials prepared in 0.75-MACl/MAI gave higher conversion values for $MAPbI_3$ perovskite generated from $PbI_2$ compared to those in MAI, 0.45-MACl/MAI and 0.90-MACl/MAI. This indicates that a high concentration of MACl in the 0.90-MACl/MAI mixed solution might interrupt the $MAPbI_3$ perovskite formation by retarding the reaction between $PbI_2$ and MAI. From these results, despite the existence of a very small amount of Cl in the perovskite film, we found that Cl incorporation can induce a significant improvement in the surface morphologies and crystallinities, as
shown in Figure 2 and Figure 3, which can ultimately lead to improved device performance of the PrSCs.

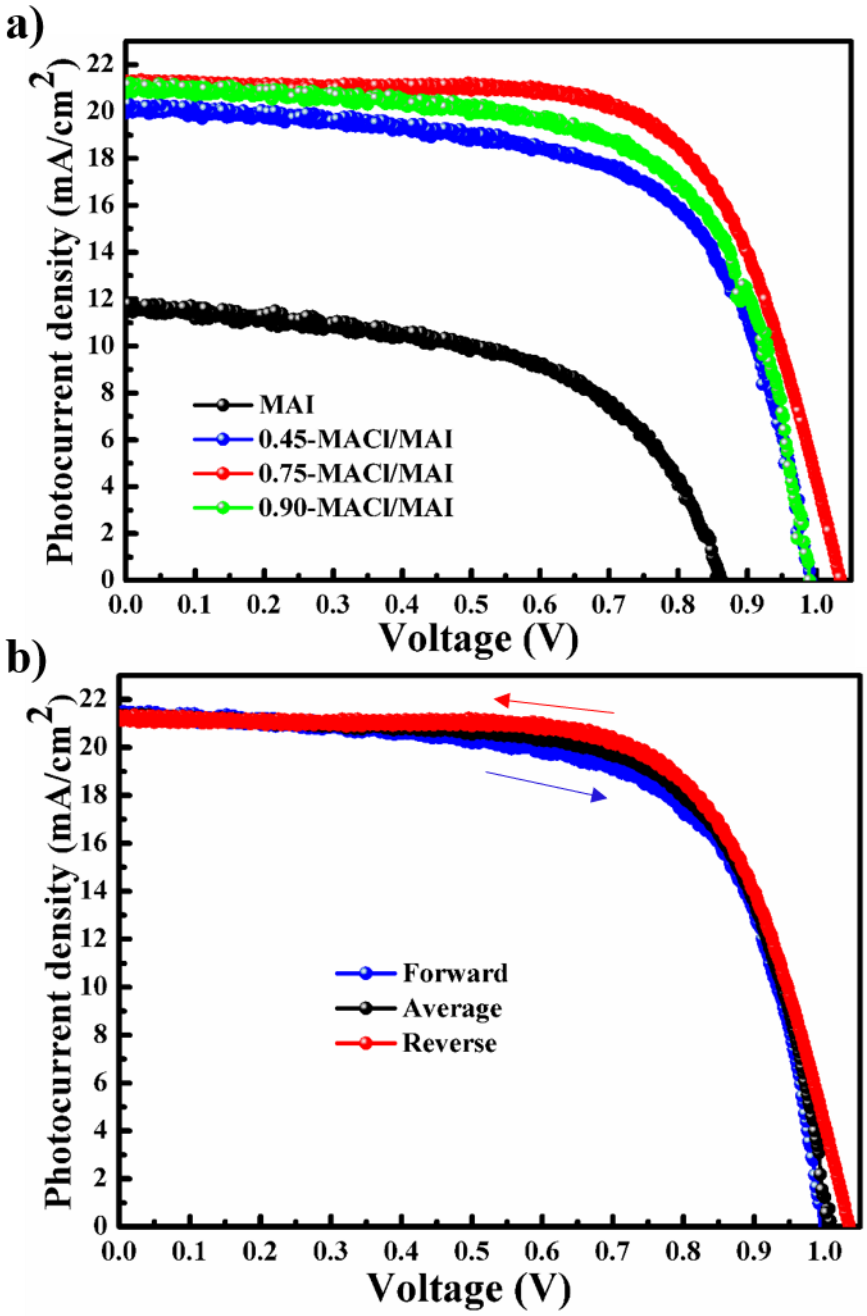


**Figure 5:** (a) the current–voltage (J–V) curves for most efficient PrSCs based on $MAPbI_3$ (black dotted line) in MAI and $MAPbI_{3-x}Cl_x$ perovskite layers fabricated via a simple all-dip-coating approach in 0.45-MACl/MAI (blue dotted line), 0.75-MACl/MAI (red dotted line), and 0.90-MACl/MAI (green dotted line) under the optimized conditions and (b) the hysteresis of

the *J-V* curves in both scan directions for the PrSC devices with the $MAPbI_{3-x}Cl_x$ perovskite layer prepared in 0.75-MACl/MAI.

Subsequently, we evaluated the photovoltaic performances of PrSCs with $MAPbI_3$ and $MAPbI_{3-x}Cl_x$ perovskite material films deposited on the thin ZnO/c-$TiO_2$ bilayer ETL by a simple all-dip-coating approach in MAI and MACl/MAI mixed solutions, respectively, and an aqueous $Pb(NO_3)_2$ solution. The PrSC devices were constructed with an n-i-p configuration of FTO/c-$TiO_2$/ZnO/$MAPbI_3$ (or $MAPbI_{3-x}Cl_x$)/HTM/$MoO_3$/Ag. The conductivity and efficiency of 2,2',7,7'-Tetrakis(N,N-di-4-methoxyphenylamino)-9,9'-spirobifluorene (spiro-OMeTAD) used as the HTM were improved after doping with additives such as 4-*tert*-butylpyridine (*t*-BPy) and lithium bis(trifluoromethanesulfonyl)imide (Li-TFSI).[5,9] We determined the optimum photovoltaic performance by comparing more than 200 individual PrSC devices. Figure 4a shows the current–voltage (*J–V*) curves under an AM 1.5 irradiation (100 $mW \cdot cm^{-1}$) for most efficient PrSCs based on $MAPbI_{3-x}Cl_x$ perovskite layers fabricated via a simple all-dip-coating approach in 0.45-MACl/MAI (blue dotted line), 0.75-MACl/MAI (red dotted line), and 0.90-MACl/MAI (green dotted line) under the optimized conditions, alongside a comparison with $MAPbI_3$ in MAI (black dotted line). The results obtained during the optimization of the device performances are also shown in Figure S5-S7.

As shown in Figure 4a, the PrSC devices with an $MAPbI_{3-x}Cl_x$ perovskite layer prepared in MACl/MAI exhibited much better performance than that of $MAPbI_3$ in MAI carried out under the same conditions. The most efficient device performances are observed in the PrSC devices with the $MAPbI_{3-x}Cl_x$ perovskite layer prepared in 0.75-MACl/MAI; the PCEs are quite notable with a maximum/average of 15.29%/15.18% with a short-circuit current density ($J_{sc}$) of 21.31 $mA \cdot cm^{-2}$, open-circuit voltage ($V_{oc}$) of 1.04 V, and fill factor (*F.F*) of 0.69. The PrSC devices with the $MAPbI_{3-x}Cl_x$ perovskite layer prepared in 0.45-MACl/MAI and 0.90-MACl/MAI also presented distinguished PCEs of 12.93%/12.78% (with $J_{sc}$ = 20.09 $mA \cdot cm^{-2}$, $V_{oc}$ = 0.99 V, and *F.F* = 0.65) and 13.79%/13.67% (with $J_{sc}$ = 21.11 $mA \cdot cm^{-2}$, $V_{oc}$ = 0.99 V, and *F.F* = 0.66), respectively, while the PrSC devices with the $MAPbI_3$ perovskite layer prepared in MAI exhibited PCEs of 5.51/4.98% with $J_{sc}$ = 11.64 $mA \cdot cm^{-2}$, $V_{oc}$ = 0.86 V, and *F.F* = 0.55. These results may have been caused by the better surface coverage and crystallinity of the $MAPbI_{3-}$

$_xCl_x$ perovskite films because Cl insertion into the $MAPbI_3$ perovskite lattice often demonstrates the passivation of surface defects, interfaces, and grain boundaries, thereby reducing the risk of parasitic non-radiative recombination and improving the carrier diffusion and charge separation. In contrast, the typical n-i-p PrSCs fabricated with the $TiO_2$ electrode often show hysteretic *J-V* behavior depending on the scan direction (reverse or forward) due to varying charge extraction or transportation rates of holes and electrons separated from excitons.[22] Figure 4b shows the hysteresis of the *J-V* curves in both scan directions under AM 1.5 irradiation (100 $mW \cdot cm^{-1}$) for the best-performing PrSC devices with the $MAPbI_{3-x}Cl_x$ perovskite layer prepared in 0.75-MACl/MAI. These values are summarized in Table S2.

Most of the PrSCs exhibited negligible differences in $J_{sc}$ values in both directions, but the $V_{oc}$ and *F.F* values were slightly reduced in the forward direction. Nonetheless, the average PCE value obtained in both directions is approximately 4% lower than the PCE value in the reverse direction. Figure 5 shows (a) EQE spectra and (b) stability for the most efficient PrSC devices with the $MAPbI_{3-x}Cl_x$ perovskite layer prepared in 0.75-MACl/MAI. As shown in Figure 5, these PrSC devices also present good external quantum efficiencies (EQEs) in the light-absorption region, in which the integrated photocurrents are well correlated with the $J_{sc}$ values, and good operational stability is obtained without a significant lowering of photovoltaic performance for 400 h under 1 sun light intensity.

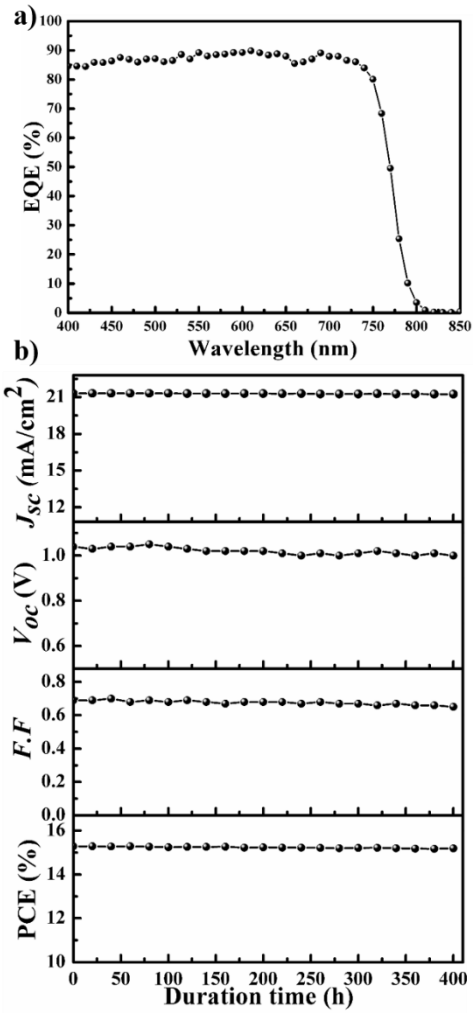


**Figure 6:** (a) EQE spectra and (b) stability for the most efficient PrSC devices with the $MAPbI_{3-x}Cl_x$ perovskite layer prepared in 0.75-MACl/MAI

## 3. Conclusion

We have demonstrated the preparation of highly efficient $MAPbI_{3-x}Cl_x$ perovskite materials using a simple, sequential all-dip-coating deposition in an aqueous nonhalide lead precursor solution and MACl/MAI mixed solution toward a facile, cost-effective, and environmentally benign manufacturing processe for high-efficiency PrSCs. The $MAPbI_{3-x}Cl_x$ perovskite layers deposited via this dip-coating process were constructed with a Cl/I ratio below ~3%, indicating

the partial insertion of Cl into the MAPbI3 perovskite lattice. The inserted amounts of Cl were readily modulated by varying the MACl concentration in the MAI and MACl mixed solution. A slight Cl incorporation led to significant improvements in the surface morphology and crystallinity of the $MAPbI_{3-x}Cl_x$ perovskite layer compared to those of $MAPbI_3$ fabricated under the same conditions. PrSC devices fabricated with these perovskite films exhibited superior device performances and stabilities, resulting in an outstanding PCE of ~15.3%. Thus, we successfully realized highly efficient $MAPbI_{3-x}Cl_x$ perovskite materials with an aqueous nonhalide lead precursor, in contrast to the conventional spin-casting approach that requires toxic organic solvents. The results of this study lay the groundwork for environmentally benign and low-cost manufacture of high-efficiency PrSCs.

# Chapter 5

# *Conclusion of the Study*

## Conclusion

We have demonstrated the preparation of highly efficient $MAPbI_3$ and $MAPbI_{3-x}Cl_x$ perovskite materials using a simple, sequential all-dip-coating deposition in an aqueous nonhalide lead precursor solution and in pure MAI and MACl/MAI mixed solution toward a facile, cost-effective, and environmentally benign manufacturing processe for high-efficiency PrSCs. The $MAPbI_3$ and $MAPbI_{3-x}Cl_x$ perovskite layers deposited via this dip-coating process were constructed with a Cl/I ratio below ~3%, indicating the partial insertion of Cl into the $MAPbI_3$ perovskite lattice. The inserted amounts of Cl were readily modulated by varying the MACl concentration in the MAI and MACl mixed solution. A slight Cl incorporation led to significant improvements in the surface morphology and crystallinity of the $MAPbI_{3-x}Cl_x$ perovskite layer compared to those of $MAPbI_3$ fabricated under the same conditions. PrSC devices fabricated with these perovskite films exhibited superior device performances and stabilities, resulting in an outstanding PCE of ~15.3%. Thus, we successfully realized highly efficient $MAPbI_{3-x}Cl_x$ perovskite materials with an aqueous nonhalide lead precursor, in contrast to the conventional spin-casting approach that requires toxic organic solvents. The results of this study lay the groundwork for environmentally benign and low-cost manufacture of high-efficiency PrSCs.

## References

(1) https://www.nrel.gov/news/features/2018/text-perovskites.html

(2) Frecker, T., et al., *Review—Quantum Dots and Their Application in Lighting, Displays, and Biology*. ECS Journal of Solid-State Science and Technology, 2016**. 5**: p. R3019–R3031.

(3) Zong, Y., et al., *Homogenous Alloys of Formamidinium Lead Triiodide and Cesium Tin Triiodide for Efficient Ideal-Bandgap Perovskite Solar Cells*. Angewandte Chemie International Edition, 2017**. 56** (41): p. 12658–12662.

(4) Tavakoli, M.M., et al., *Large-Grain Tin-Rich Perovskite Films for Efficient Solar Cells via Metal Alloying Technique*. Advanced Materials, 2018**. 30** (11): p. 1705998.

(5) Zhu, H.L., et al., *Controllable Crystallization of CH3NH3Sn0.25Pb0.75I3 Perovskites for Hysteresis-Free Solar Cells with Efficiency Reaching 15.2%*. Advanced Functional Materials, 2017**. 27** (11): p. 1605469.

(6) Chen, C., et al., *Efficient Perovskite Solar Cells Based on Low-Temperature Solution-Processed (CH3NH3) PbI3 Perovskite/CuInS2 Planar Heterojunctions*. Nanoscale research letters, 2014**. 9**: p. 457.

(7) Hao, F., et al., *Lead-Free Solid-State Organic–Inorganic Halide Perovskite Solar Cells*. Nature Photonics, 2014**. 8** (6): p. 489–494.

(8) Tenuta, E., et al., *Thermodynamic Origin of Instability in Hybrid Halide Perovskites*. Scientific Reports, 2016**. 6** (1): p. 37654.

(9) Noel, N.K., et al., *Lead-Free Organic–Inorganic Tin Halide Perovskites for Photovoltaic Applications*. Energy & Environmental Science, 2014**. 7** (9): p. 3061–3068.

(10) Niu, G., et al., *Study on the Stability of CH3NH3PbI3 Films and the Effect of Post-Modification by Aluminum Oxide in All-Solid-State Hybrid Solar Cells*. Journal of Materials Chemistry A, 2014**. 2** (3): p. 705–710.

(11) Hao, F., et al., *Anomalous Band Gap Behavior in Mixed Sn and Pb Perovskites Enables Broadening of Absorption Spectrum in Solar Cells*. Journal of the American Chemical Society, 2014**. 136** (22): p. 8094–8099.

(12) You, J., et al., *Low-Temperature Solution-Processed Perovskite Solar Cells with High Efficiency and Flexibility*. ACS Nano, 2014**. 8** (2): p. 1674–1680.

(13) Pellet, N., et al., *Mixed-Organic-Cation Perovskite Photovoltaics for Enhanced Solar-Light Harvesting*. Angewandte Chemie International Edition, 2014**. 53** (12): p. 3151–3157.

(14) Tidhar, Y., et al., *Crystallization of Methyl Ammonium Lead Halide Perovskites: Implications for Photovoltaic Applications*. Journal of the American Chemical Society, 2014**. 136** (38): p. 13249–13256.

(15) Wang, D., et al., *Reproducible One-Step Fabrication of Compact MAPbI3–XClx Thin Films Derived from Mixed-Lead-Halide Precursors*. Chemistry of Materials, 2014**. 26** (24): p. 7145–7150.

(16) Colella, S., et al., *MAPbI3-XClx Mixed Halide Perovskite for Hybrid Solar Cells: The Role of Chloride as Dopant on the Transport and Structural Properties*. Chemistry of Materials, 2013**. 25** (22): p. 4613–4618.

(17) Im, J.-H., et al., *Morphology-Photovoltaic Property Correlation in Perovskite Solar Cells: One-Step versus Two-Step Deposition of CH3NH3PbI3*. APL Materials, 2014**. 2** (8): p. 81510.

(18) Chen, C.-W., et al., *Efficient and Uniform Planar-Type Perovskite Solar Cells by Simple Sequential Vacuum Deposition.* Advanced materials (Deerfield Beach, Fla.), 2014**. 26** (38): p. 6647–6652.

(19) Wehrenfennig, C., et al., *High Charge Carrier Mobilities and Lifetimes in Organolead Trihalide Perovskites*. Advanced Materials, 2014**. 26** (10): p. 1584–1589.

(20) Dharani, S., et al., *High Efficiency Electrospun TiO2 Nanofiber Based Hybrid Organic–Inorganic Perovskite Solar Cell*. Nanoscale, 2014**. 6** (3): p. 1675–1679.

(21) Hu, L., et al., *Sequential Deposition of CH3NH3PbI3 on Planar NiO Film for Efficient Planar Perovskite Solar Cells*. ACS Photonics, 2014**. 1** (7): p. 547–553.

(22) Chen, Q., et al., *Planar Heterojunction Perovskite Solar Cells via Vapor-Assisted Solution Process*. Journal of the American Chemical Society, 2014**. 136** (2): p. 622–625.

(23) McGehee, M.D., *Continuing to Soar*. Nature Materials, 2014**. 13** (9): p. 845–846.

(24) Eperon, G.E., et al., *Morphological Control for High Performance, Solution-Processed Planar Heterojunction Perovskite Solar Cells*. Advanced Functional Materials, 2014**. 24** (1): p. 151–157.

(25) Pang, S., et al., *NH2CH═NH2PbI3: An Alternative Organolead Iodide Perovskite Sensitizer for Mesoscopic Solar Cells*. Chemistry of Materials, 2014**. 26** (3): p. 1485–1491.

(26) Chen, H.-W., et al., *Emergence of Hysteresis and Transient Ferroelectric Response in Organo-Lead Halide Perovskite Solar Cells*. The Journal of Physical Chemistry Letters, 2015**. 6** (1): p. 164–169.

(27) Wei, J., et al., *Hysteresis Analysis Based on the Ferroelectric Effect in Hybrid Perovskite Solar Cells*. The Journal of Physical Chemistry Letters, 2014**. 5** (21): p. 3937–3945.

(28) Eames, C., et al., *Ionic Transport in Hybrid Lead Iodide Perovskite Solar Cells*. Nature Communications, 2015**. 6** (1): p. 7497.

(29) Arora, N., et al., *Perovskite Solar Cells with CuSCN Hole Extraction Layers Yield Stabilized Efficiencies Greater than 20.* Science (New York, N.Y.), 2017**. 358** (6364): p. 768–771.

(30) Grancini, G., et al., *One-Year Stable Perovskite Solar Cells by 2D/3D Interface Engineering*. Nature Communications, 2017**. 8** (1): p. 15684.

(31) Christians, J.A., et al., *Best Practices in Perovskite Solar Cell Efficiency Measurements. Avoiding the Error of Making Bad Cells Look Good*. The Journal of Physical Chemistry Letters, 2015**. 6** (5): p. 852–857.

(32) Gong, J., et al., *Perovskite Photovoltaics: Life-Cycle Assessment of Energy and Environmental Impacts*. Energy & Environmental Science, 2015**. 8** (7): p. 1953–1968.

(33) Sepalage, G.A., et al., *Copper(I) Iodide as Hole-Conductor in Planar Perovskite Solar Cells: Probing the Origin of J–V Hysteresis*. Advanced Functional Materials, 2015**. 25** (35): p. 5650–5661.

(34) Ono, L.K., et al., *Temperature-Dependent Hysteresis Effects in Perovskite-Based Solar Cells*. Journal of Materials Chemistry A, 2015**. 3** (17): p. 9074–9080.

(35) Kim, H.-S., et al., *Parameters Affecting I-V Hysteresis of CH3NH3PbI3 Perovskite Solar Cells: Effects of Perovskite Crystal Size and Mesoporous TiO2 Layer*. The journal of physical chemistry letters, 2014**. 5** (17): p. 2927–2934.

(36) Li, C., et al., *Iodine Migration and Its Effect on Hysteresis in Perovskite Solar Cells*. Advanced Materials, 2016**. 28** (12): p. 2446–2454.

(37) Chapin, D.M., et al., *A New Silicon P-n Junction Photocell for Converting Solar Radiation into Electrical Power*. Journal of Applied Physics, 1954**. 25** (5): p. 676–677.

(38) Zhao, C., et al., *Revealing Underlying Processes Involved in Light Soaking Effects and Hysteresis Phenomena in Perovskite Solar Cells*. Advanced Energy Materials, 2015**. 5** (14): p. 1500279.

(39) Calado, P., et al., *Evidence for Ion Migration in Hybrid Perovskite Solar Cells with Minimal Hysteresis*. Nature Communications, 2016**. 7** (1): p. 13831.

(40) Meloni, S., et al., *Ionic Polarization-Induced Current–Voltage Hysteresis in CH3NH3PbX3 Perovskite Solar Cells*. Nature Communications, 2016**. 7** (1): p. 10334.

(41) Becquerel, A.E., *Recherches Sur Les Effets de La Radiation Chimique de La Lumiere Solaire Au Moyen Des Courants Electriques*. Comptes Rendus de L{\textasciiacute}Academie des Sciences, 1839**. 9**: p. 145–149.

(42) Sum, T.C., et al., *Advancements in Perovskite Solar Cells: Photophysics behind the Photovoltaics*. Energy Environ. Sci., 2014**. 7** (8): p. 2518–2534.

(43) Cheng, Y.-J., et al., *Synthesis of Conjugated Polymers for Organic Solar Cell Applications*. Chemical Reviews, 2009**. 109** (11): p. 5868–5923.

(44) Islam, M.B., et al., *Highly Stable Semi-Transparent MAPbI3 Perovskite Solar Cells with Operational Output for 4000 H*. Solar Energy Materials and Solar Cells, 2019**. 195**: p. 323–329.

(45) Wu, X., *High-Efficiency Polycrystalline CdTe Thin-Film Solar Cells*. Solar Energy, 2004**. 77**: p. 803–814.

(46) Sommeling, P.M., et al., *Long-Term Stability Testing of Dye-Sensitized Solar Cells*. Journal of Photochemistry and Photobiology A: Chemistry, 2004**. 164**: p. 137–144.

(47) Conibeer, G., *Third-Generation Photovoltaics*. Materials Today, 2007**. 10** (11): p. 42–50.

(48) Mathew, S., et al., *Dye-Sensitized Solar Cells with 13% Efficiency Achieved through the Molecular Engineering of Porphyrin Sensitizers.* Nature chemistry, 2014**. 6** (3): p. 242–247.

(49) Gong, J., et al., *Review on Dye-Sensitized Solar Cells (DSSCs): Advanced Techniques and Research Trends*. Renewable and Sustainable Energy Reviews, 2017**. 68**: p. 234–246.

(50) Snaith, H.J., *Perovskites: The Emergence of a New Era for Low-Cost, High-Efficiency Solar Cells*. The Journal of Physical Chemistry Letters, 2013**. 4** (21): p. 3623–3630.

(51) Grätzel, M., *Photoelectrochemical Cells.* Nature, 2001**. 414** (6861): p. 338–344.

(52) Dette, C., et al., *TiO2 Anatase with a Bandgap in the Visible Region.* Nano letters, 2014**. 14** (11): p. 6533–6538.

(53) Grossiord, N., et al., *Degradation Mechanisms in Organic Photovoltaic Devices*. Organic Electronics, 2012**. 13** (3): p. 432–456.

(54) Im, J.-H., et al., *6.5% Efficient Perovskite Quantum-Dot-Sensitized Solar Cell.* Nanoscale, 2011**. 3** (10): p. 4088–4093.

(55) Li, C., et al., *Formability of {\its ABX} ${\sb 3} $ ({\it X} = F, Cl, Br, I) Halide Perovskites*. Acta Crystallographica Section B, 2008**. 64** (6): p. 702–707.

(56) Park, N.-G., *Perovskite Solar Cells: An Emerging Photovoltaic Technology*. Materials Today, 2015**. 18** (2): p. 65–72.

(57) Upadhyaya, H.M., et al., *Recent Progress and the Status of Dye-Sensitised Solar Cell (DSSC) Technology with State-of-the-Art Conversion Efficiencies*. Solar Energy Materials and Solar Cells, 2013**. 119**: p. 291–295.

(58) Etgar, L., *Mesoscopic CH3NH3PbI3/TiO2 Heterojunction Solar Cells*. J. Am. Chem. Soc., 2012**. 134**: .

(59) Fabregat-Santiago, F., et al., *Electron Transport and Recombination in Solid-State Dye Solar Cell with Spiro-OMeTAD as Hole Conductor*. Journal of the American Chemical Society, 2009**. 131** (2): p. 558–562.

(60) Snaith, H.J., et al., *Efficiency Enhancements in Solid-State Hybrid Solar Cells via Reduced Charge Recombination and Increased Light Capture.* Nano letters, 2007**. 7** (11): p. 3372–3376.

(61) Liu, M., *Efficient Planar Heterojunction Perovskite Solar Cells by Vapour Deposition*. Nature., 2013**. 501**:

(62) Liang, P., *Additive Enhanced Crystallization of Solution-Processed Perovskite for Highly Efficient Planar-Heterojunction Solar Cells*. Adv. Mater., 2014**. 26**.

(63) Snaith, H.J., *Anomalous Hysteresis in Perovskite Solar Cells*. J. Phys. Chem. Lett., 2014**. 5**.

(64) Lee, M.M., *Efficient Hybrid Solar Cells Based on Meso-Superstructured Organometal Halide Perovskites*. Science., 2012**. 338**.

(65) Kojima, A., *Organometal Halide Perovskites as Visible-Light Sensitizers for Photovoltaic Cells*. J. Am. Chem. Soc., 2009**. 131**.

(66) Juárez-Pérez, E.J., et al., *Perovskite Solar Cells Take a Step Forward*. Science, 2020**. 368**: p. 1309.

(67) Xiao, Z., et al., *Efficient {,} High Yield Perovskite Photovoltaic Devices Grown by Interdiffusion of Solution-Processed Precursor Stacking Layers*. Energy Environ. Sci., 2014**. 7** (8): p. 2619–2623.

(68) Saliba, M., et al., *Cesium-Containing Triple Cation Perovskite Solar Cells: Improved Stability, Reproducibility and High Efficiency*. Energy and Environmental Science, 2016**. 9** (6): p. 1989–1997.

(69) Jeon, N.J., et al., *Solvent Engineering for High-Performance Inorganic-Organic Hybrid Perovskite Solar Cells*. Nature Materials, 2014**. 13** (9): p. 897–903.

(70) Unger, E.L., et al., *Hysteresis and Transient Behavior in Current-Voltage Measurements of Hybrid-Perovskite Absorber Solar Cells*. Energy and Environmental Science, 2014**. 7** (11): p. 3690–3698.

(71) Alcocer, M.J.P., et al., *Electron-Hole Diffusion Lengths Exceeding Trihalide Perovskite Absorber*. Science, 2013**. 342** (October): p. 341–344.

(72) Jäger-Waldau, A., et al., *{PV} Status Report 2017 Study.*; 2017.

(73) Khenkin, M. V., et al., *Consensus Statement for Stability Assessment and Reporting for Perovskite Photovoltaics Based on ISOS Procedures*. Nature Energy, 2020**. 5** (1): p. 35–49.

(74) Cheacharoen, R., et al., *Encapsulating Perovskite Solar Cells to Withstand Damp Heat and Thermal Cycling*. Sustainable Energy and Fuels, 2018**. 2** (11): p. 2398–2406.

(75) Bin, H., et al., *11.4% Efficiency Non-Fullerene Polymer Solar Cells with Trialkylsilyl Substituted 2D-Conjugated Polymer as Donor*. Nature Communications, 2016**. 7** (May): p. 1–11.

(76) GREEN, M., et al., *Solar Cell Efficiency Tables (Version 40)*. Ieee Trans Fuzzy Syst, 2012**. 20** (6): p. 1114–1129.

(77) Fthenakis, V., *Sustainability of Photovoltaics: The Case for Thin-Film Solar Cells*. Renewable and Sustainable Energy Reviews, 2009**. 13** (9): p. 2746–2750.

(78) Kazim, S., et al., *Perovskite as Light Harvester: A Game Changer in Photovoltaics*. Angewandte Chemie - International Edition, 2014**. 53** (11): p. 2812–2824.

(79) Green, M.A., et al., *Solar Cell Efficiency Tables (Version 51)*. Progress in Photovoltaics: Research and Applications, 2018**. 26** (1): p. 3–12.

(80) Sanehira, E.M., et al., *Enhanced Mobility CsPbI3 Quantum Dot Arrays for Record-Efficiency, High-Voltage Photovoltaic Cells*. Science Advances, 2017**. 3** (10).

(81) Snaith, H.J., et al., *Advances in Liquid-Electrolyte and Solid-State Dye-Sensitized Solar Cells*. Advanced Materials, 2007**. 19** (20): p. 3187–3200.

(82) Bisquert, J., et al., *The Causes of Degradation of Perovskite Solar Cells*. Journal of Physical Chemistry Letters, 2019**. 10** (19): p. 5889–5891.

(83) EPKI, *Perovskite-Based Photovoltaics: A Unique Chance for European PV-Industry*. White Paper from the EPKI, 2019**.** No. September.

(84) Shi, L., et al., *Gas Chromatography-Mass Spectrometry Analyses of Encapsulated Stable Perovskite Solar Cells*. Science, 2020**. 368** (6497).

(85) Kim, H.S., et al., *Lead Iodide Perovskite Sensitized All-Solid-State Submicron Thin Film Mesoscopic Solar Cell with Efficiency Exceeding 9%*. Scientific Reports, 2012**. 2**: p. 1–7.

(86) Burschka, J., et al., *Sequential Deposition as a Route to High-Performance Perovskite-Sensitized Solar Cells*. Nature, 2013**. 499** (7458): p. 316–319.

(87) Xiao, Z., et al., *Efficient {,} High Yield Perovskite Photovoltaic Devices Grown by Interdiffusion of Solution-Processed Precursor Stacking Layers*. Energy Environ. Sci., 2014**. 7** (8): p. 2619–2623.

(88) Unger, E.L., et al., *Hysteresis and Transient Behavior in Current-Voltage Measurements of Hybrid-Perovskite Absorber Solar Cells*. Energy and Environmental Science, 2014**. 7** (11): p. 3690–3698.

(89) Song, X., et al., *Additive to Regulate the Perovskite Crystal Film Growth in Planar Heterojunction Solar Cells*. Applied Physics Letters, 2015**. 106** (3): p. 33901.

(90) Li, H., et al., *Tunable Growth of PbS Quantum Dot–ZnO Heterostructure and Mechanism Analysis*. CrystEngComm, 2015**. 17** (25): p. 4722–4728.

(91) Hsu, H.-L., et al., *Two-Step Thermal Annealing Improves the Morphology of Spin-Coated Films for Highly Efficient Perovskite Hybrid Photovoltaics*. Nanoscale, 2014**. 6** (17): p. 10281–10288.

(92) Aldibaja, F.K., et al., *Effect of Different Lead Precursors on Perovskite Solar Cell Performance and Stability*. J. Mater. Chem. A, 2015**. 3** (17): p. 9194–9200.

(93) Li, H., et al., *Reaction Mechanism of a PbS-on-ZnO Heterostructure and Enhanced Photovoltaic Diode Performance with an Interface-Modulated Heterojunction Energy Band Structure*. Phys. Chem. Chem. Phys., 2016**. 18** (5): p. 4144–4153.

(94) Chueh, C.C., et al., *The Roles of Alkyl Halide Additives in Enhancing Perovskite Solar Cell Performance*. Journal of Materials Chemistry A, 2015**. 3** (17): p. 9058–9062.

(95) Hsieh, T.-Y., et al., *Efficient Perovskite Solar Cells Fabricated Using an Aqueous Lead Nitrate Precursor*. Chem. Commun., 2015**. 51** (68): p. 13294–13297.

(96) Malinkiewicz, O., et al., *Perovskite Solar Cells Employing Organic Charge-Transport Layers*. Nature Photonics, 2014**. 8** (2): p. 128–132.

(97) Heo, J.H., et al., *Efficient Inorganic–Organic Hybrid Heterojunction Solar Cells Containing Perovskite Compound and Polymeric Hole Conductors*. Nature Photonics, 2013**. 7** (6): p. 486–491.

(98) Zhang, W., et al., *Ultrasmooth Organic-Inorganic Perovskite Thin-Film Formation and Crystallization for Efficient Planar Heterojunction Solar Cells*. Nature Communications, 2015**. 6**.

(99) Lee, J.W., et al., *Lewis Acid-Base Adduct Approach for High Efficiency Perovskite Solar Cells*. Accounts of Chemical Research, 2016**. 49** (2): p. 311–319.

(100) Podolsky, B., et al., *References and Notes 1*. 2012**. 338** (November): p. 643–648.

(101) Sun, Y., et al., *Inverted Polymer Solar Cells Integrated with a Low-Temperature-Annealed Sol-Gel-Derived ZnO Film as an Electron Transport Layer*. Advanced Materials, 2011**. 23** (14): p. 1679–1683.

(102) Colella, S., et al., *MAPbI3-XClx Mixed Halide Perovskite for Hybrid Solar Cells: The Role of Chloride as Dopant on the Transport and Structural Properties*. Chemistry of Materials, 2013**. 25** (22): p. 4613–4618.

(103) Matthews, J.A., *Environmental Science*. Encyclopedia of Environmental Change, 2014**.**

(104) Nicolau, Y.F., *Solution Deposition of Thin Solid Compound Films by a Successive Ionic-Layer Adsorption and Reaction Process*. Applications of Surface Science, 1985**. 22**–**23** (PART 2): p. 1061–1074.

(105) Jeng, J.Y., et al., *CH3NH3PbI3 Perovskite/Fullerene Planar-Heterojunction Hybrid Solar Cells*. Advanced Materials, 2013**. 25** (27): p. 3727–3732.

(106) Sun, S., et al., *The Origin of High Efficiency in Low-Temperature Solution-Processable Bilayer Organometal Halide Hybrid Solar Cells*. Energy and Environmental Science, 2014**. 7** (1): p. 399–407.

(107) Etgar, L., et al., *Mesoscopic CH 3NH 3PbI 3/TiO 2 Heterojunction Solar Cells*. Journal of the American Chemical Society, 2012**. 134** (42): p. 17396–17399.

(108) Snaith, H.J., et al., *Anomalous Hysteresis in Perovskite Solar Cells*. Journal of Physical Chemistry Letters, 2014**. 5** (9): p. 1511–1515.

(109) Kim, H.S., et al., *Lead Iodide Perovskite Sensitized All-Solid-State Submicron Thin Film Mesoscopic Solar Cell with Efficiency Exceeding 9%*. Scientific Reports, 2012**. 2**: p. 1–7.

(110) Burschka, J., et al., *Sequential Deposition as a Route to High-Performance Perovskite-Sensitized Solar Cells*. Nature, 2013**. 499** (7458): p. 316–319.

(111) Meng, L., et al., *Recent Advances in the Inverted Planar Structure of Perovskite Solar Cells*. Accounts of Chemical Research, 2016**. 49** (1): p. 155–165.

(112) Noh, J.H., et al., *Chemical Management for Colorful, Efficient, and Stable Inorganic-Organic Hybrid Nanostructured Solar Cells*. Nano Letters, 2013**. 13** (4): p. 1764–1769.

(113) Ahn, N., et al., *Highly Reproducible Perovskite Solar Cells with Average Efficiency of 18.3% and Best Efficiency of 19.7% Fabricated via Lewis Base Adduct of Lead (II) Iodide*. Journal of the American Chemical Society, 2015**. 137** (27): p. 8696–8699.

(114) Liu, M., et al., *Efficient Planar Heterojunction Perovskite Solar Cells by Vapour Deposition*. Nature, 2013**. 501** (7467): p. 395–398.

(114) Xiao, M., et al., *A Fast Deposition-Crystallization Procedure for Highly Efficient Lead Iodide Perovskite Thin-Film Solar Cells*. Angewandte Chemie, 2014**. 126** (37): p. 10056–10061.

(115) Liang, P.W., et al., *Additive Enhanced Crystallization of Solution-Processed Perovskite for Highly Efficient Planar-Heterojunction Solar Cells*. Advanced Materials, 2014**. 26** (22): p. 3748–3754.

(116) Abrusci, A., et al., *High-Performance Perovskite-Polymer Hybrid Solar Cells via Electronic Coupling with Fullerene Monolayers*. Nano Letters, 2013**. 13** (7): p. 3124–3128.

(117) Kojima, A., et al., *Organometal Halide Perovskites as Visible-Light Sensitizers for Photovoltaic Cells*. Journal of the American Chemical Society, 2009**. 131** (17): p. 6050–6051.

(118) Saliba, M., et al., *Cesium-Containing Triple Cation Perovskite Solar Cells: Improved*

*Stability, Reproducibility and High Efficiency*. Energy and Environmental Science, 2016**. 9** (6): p. 1989–1997.

(119) Xu, R.P., et al., *In Situ Observation of Light Illumination-Induced Degradation in Organometal Mixed-Halide Perovskite Films*. ACS Applied Materials and Interfaces, 2018**. 10** (7): p. 6737–6746.

(120) Saliba, M., et al., *Cesium-Containing Triple Cation Perovskite Solar Cells: Improved Stability, Reproducibility and High Efficiency*. Energy and Environmental Science, 2016**. 9** (6): p. 1989–1997.

(121) Jeon, N.J., et al., *A Fluorene-Terminated Hole-Transporting Material for Highly Efficient and Stable Perovskite Solar Cells*. Nature Energy, 2018**. 3** (8): p. 682–689.

(122) Wang, J.F., et al., *Surface Engineering of Perovskite Films for Efficient Solar Cells*. Scientific Reports, 2017**. 7** (1): p. 1–9.

(123) Hsieh, T.-Y., et al., *Efficient Perovskite Solar Cells Fabricated Using an Aqueous Lead Nitrate Precursor*. Chem. Commun., 2015**. 51** (68): p. 13294–13297.

(124) Tan, H., et al., *Efficient and Stable Solution-Processed Planar Perovskite Solar Cells via Contact Passivation*. Science, 2017**. 355** (6326): p. 722–726

(125) Unger, E.L., et al., *Chloride in Lead Chloride-Derived Organo-Metal Halides for Perovskite-Absorber Solar Cells*. Chemistry of Materials, 2014**. 26** (24): p. 7158–7165.

(126) Philippe, B., et al., *Chemical and Electronic Structure Characterization of Lead Halide Perovskites and Stability Behavior under Different Exposures-A Photoelectron Spectroscopy Investigation*. Chemistry of Materials, 2015**. 27** (5): p. 1720–1731.

(127) Dong, Q., et al., *Abnormal Crystal Growth in CH3NH3PbI3-XClx Using a Multi-Cycle Solution Coating Process*. Energy and Environmental Science, 2015**. 8** (8): p. 2464–2470.

(128) Shinde, D. V., et al., *Enhanced Efficiency and Stability of an Aqueous Lead-Nitrate-Based Organometallic Perovskite Solar Cell*. ACS Applied Materials and Interfaces, 2017**. 9** (16): p. 14023–14030.

(129) Adnan, M., et al., *All Sequential Dip-Coating Processed Perovskite Layers from an Aqueous Lead Precursor for High Efficiency Perovskite Solar Cells*. Scientific Reports, 2018**. 8** (1): p. 1–10.

(130) Heo, J.H., et al., *Highly Efficient CH3NH3PbI3−xClx Mixed Halide Perovskite Solar Cells Prepared by Re-Dissolution and Crystal Grain Growth via Spray Coating*. Journal of Materials Chemistry A, 2016**. 4** (45): p. 17636–17642.

(131) Jiang, M., et al., *Enhancing the Performance of Planar Organo-Lead Halide Perovskite Solar Cells by Using a Mixed Halide Source*. Journal of Materials Chemistry A, 2015**. 3** (3): p. 963–967.

(132) Zhao, Y., et al., *CH3NH3Cl-Assisted One-Step Solution Growth of CH 3NH3PbI3: Structure, Charge-Carrier Dynamics, and Photovoltaic Properties of Perovskite Solar Cells*. Journal of Physical Chemistry C, 2014**. 118** (18): p. 9412–9418.

(133) Maniarasu, S., et al., *Hole-Conductor Free Ambient Processed Mixed Halide Perovskite Solar Cells*. Materials Letters, 2019**. 245**: p. 226–229.

(134) Hwang, T., et al., *Investigation of Chlorine-Mediated Microstructural Evolution of CH3NH3PbI3(Cl) Grains for High Optoelectronic Responses*. Nano Energy, 2016**. 25**: p. 91–99.

(135) Ahmadian-Yazdi, M.R., et al., *Effects of Process Parameters on the Characteristics of Mixed-Halide Perovskite Solar Cells Fabricated by One-Step and Two-Step Sequential Coating*. Nanoscale Research Letters, 2016**. 11** (1).

(136) Hsieh, T.Y., et al., *Exceptional Long Electron Lifetime in Methylammonium Lead Iodide Perovskite Solar Cell Made from Aqueous Lead Nitrate Precursor*. Advanced Functional Materials, 2020**. 30** (10): p. 1–8.

(137) Jeon, N.J., et al., *Solvent Engineering for High-Performance Inorganic-Organic Hybrid Perovskite Solar Cells*. Nature Materials, 2014**. 13** (9): p. 897–903.

(138) Sun, Y., et al., *Inverted Polymer Solar Cells Integrated with a Low-Temperature-Annealed Sol-Gel-Derived ZnO Film as an Electron Transport Layer*. Advanced Materials, 2011**. 23** (14): p. 1679–1683.

(139) Adnan, M., et al., *Highly Efficient Planar Heterojunction Perovskite Solar Cells with Sequentially Dip-Coated Deposited Perovskite Layers from a Non-Halide Aqueous Lead Precursor*. RSC Advances, 2020**. 10** (9): p. 5454–5461.

(140) Adnan, M., et al., *Facile All-Dip-Coating Deposition of Highly Efficient (CH3)3NPbI3-: XClxperovskite Materials from Aqueous Non-Halide Lead Precursor*. RSC Advances, 2020**. 10** (48): p. 29010–29017.

(141) Colella, S., et al., *MAPbI3-XClx Mixed Halide Perovskite for Hybrid Solar Cells: The Role of Chloride as Dopant on the Transport and Structural Properties*. Chemistry of Materials, 2013**. 25** (22): p. 4613–4618.

(142) Malinkiewicz, O., et al., *Perovskite Solar Cells Employing Organic Charge-Transport Layers*. Nature Photonics, 2014**. 8** (2): p. 128–132

(143) Unger, E.L., et al., *Hysteresis and Transient Behavior in Current-Voltage Measurements of Hybrid-Perovskite Absorber Solar Cells*. Energy and Environmental Science, 2014**. 7** (11): p. 3690–3698.

## Appendix A

## Acknowledgement

First and foremost, I would like to express my sincere gratitude to my advisor **Prof. Jae Kwan Lee** for his guidance and motivation. I can't thank him enough for providing me the great opportunity to pursue my Ph.D. under his supervision. He has been a marvelous mentor to me. I'm grateful for his continuous support, patience and sharing of his immense research knowledge and ideas with me. I always enjoyed the lab meetings and the discussion time with him and have learned a lot from him. His teaching and expertise have made my Ph.D. experience productive and interesting. As my advisor, his understanding and care for me made my tough times in the Ph.D. manageable. His advice on both research as well as on my career have been priceless. Throughout my Ph.D., he gave me the moral support and the freedom to pursue the research I wanted to do. Without his guidance and constant feedback, this Ph.D. would not have been possible.

My sincere thanks to the thesis committee members: **Prof. Sohn, Hong-Lae**, **Prof. Koh Moon Joo**, **Prof. Kim, Ho Joong** and **Prof. Sung Cho** for evaluating my thesis. Their insightful comments and questions have made my defense enjoyable and memorable.

I owe my gratitude to Chosun University International office team for their academic help in various stages of my Ph.D. They took us on field trips to various parts of Korea which helped me to understand and embrace the culture of Korea and warm gesture of Korean people. I thank the former coordinator **Yushin Jeong** and current coordinator **Mr. Ji Hongbum** for all their help and kindness and constant feedback throughout my Ph.D. study.

Words cannot express my thankfulness to **my parents**. They raised me independently and allowed to decide my career and pursue towards it. I also thank my sisters **Saba Ramzan**, my daughter **Miraal Adnan** and my wife **Zobia Irshad** for all their encouragement and support.

My deep appreciation goes to my co-guide and senior **Mr. Hanbin Jeong** and my senior **Mr. Kyeong Kuk Koh** who have been supportive in many ways. There are innumerable situations we discussed our research and worked together all night to keep up with deadline. I

am also grateful to my lab mate **Zobia Irshad** for her help and wonderful fun lab time. The time we spent together will always be remembered and cherished.

Besides my lab members, I extend my sincere gratitude to my all **Chosun University** friends (**Mr. Umar Afzaal, Mr. Waqas Elahi, Mr. Waleed Hussain Siddique, Mr. Usman Afzal, Zahid Hussain, Dr. Swapnil Bhujbal, Mr. Chris henry, Mr. Ijaz Ahmed, Mr. Hasanul Banna** and **Dr. He Weijie**) for their help and moral support.

Last but not least, I would like to thank all of my friends from France and Pakistan for their constant encouragement. My special thanks to my uncles **Mr. Altaf Hussain** and **Dr. Riaz Hussain** for their constant support, this journey was not possible without their kind attention. Following this, my special gratitude to my ex-professor **Dr. Javed Iqbal** for his countless help and guiding throughout my Master to Ph.D. journey. Also, my special thanks to **Mr. Tahir Gill, Mr. Khizer Qureshi, Shahab Afridi, Mr. Zubair Ahmed, Muhammad Yasir Mehboob, Dr. Hammad Majeed** and **Ms. Iram Rafique**.

I thank everyone who helped directly and indirectly to complete my doctoral study successfully.

## Appendix B

## List of publications

1. **Adnan, M**., & Lee, J. K. (2018). All sequential dip-coating processed perovskite layers from an aqueous lead precursor for high efficiency perovskite solar cells. Scientific reports, 8(1), 1–10.

2. **Adnan, M**., Irshad, Z., & Lee, J. K. (2020). Facile all-dip-coating deposition of highly efficient (ch 3) 3 npbi3- x cl x perovskite materials from aqueous non-halide lead precursor. RSC Advances, 10(48), 29010–29017.

3. **Adnan, M**., & Lee, J. K. (2020). Highly efficient planar heterojunction perovskite solar cells with sequentially dip-coated deposited perovskite layers from a non-halide aqueous lead precursor. RSC Advances, 10(9), 5454–5461.

4. **Adnan, M**., Kim, H. S., Jeong, H., Ko, H. M., Woo, S. K., & Lee, J. K. (2017). Efficient Synthesis and Characterization of Solvatochromic Fluorophore. Bulletin of the Korean Chemical Society, 38(9), 1052–1057.

5. Irshad, Z., **Adnan, M**., & Lee, J. K. (2020). Efficient Planar Heterojunction Inverted Perovskite Solar Cells with Perovskite Materials Deposited Using an Aqueous Non-Halide Lead Precursor. Bulletin of the Korean Chemical Society, 41(9), 937-942.

6. **Adnan, M**., Iqbal, J., BiBi, S., Hussain, R., Akhtar, M. N., Rashid, M. A., Eliasson, B., & Ayub, K. (2017). Fine Tuning the Optoelectronic Properties of Triphenylamine Based DonorMolecules for Organic Solar Cells. Zeitschrift für Physikalische Chemie, 231(6), 1127.

7. Hussain, S.,Hussain, R.,Mehboob, M. Y., Chatha, S. A. S.,Hussain, A. I.,Umar, A., Khan, M.U., Ahmed, M., **Adnan, M**., & Ayub, K. (2020). Adsorption of Phosgene Gas on Pristine and Copper-Decorated B12N12 Nanocages: A Comparative DFT Study. ACS omega, 5(13), 7641–7650.

8. Hussain, R., Saeed, M., Mehboob, M. Y., Khan, S. U., Khan, M. U., **Adnan, M**., Ahmed, M., Iqbal, J., & Ayub, K. (2020). Density functional theory study of palladium

cluster adsorption on a graphene support. RSC Advances, 10(35), 20595–20607.

9. Afzal, Z., Hussain, R., Khan, M. U., Khalid, M., Iqbal, J., Alvi, M. U., **Adnan, M**., Ahmed, M., Mehboob, M. Y., Hussain, M. Et al. (2020). Designing indenothiophene-based acceptor materials with efficient photovoltaic parameters for fullerene-free organic solar cells. Journal of Molecular Modeling, 26(6), 137–137.

10. Hussain, R., Khan, M. U., Mehboob, M. Y., Khalid, M., Iqbal, J., Ayub, K., **Adnan, M**., Ahmed, M., Atiq, K., & Mahmood, K. (2020). Enhancement in photovoltaic properties of n, n-diethylaniline based donor materials by bridging core modifications for efficient solar cells. Chemistry Select, 5(17), 5022–5034.

11. Bilal Ahmed Siddique, M., Hussain, R., Ali Siddique, S., Yasir Mehboob, M., Irshad, Z., Iqbal, J., & **Adnan, M***. (2020a). Enhancement in photovoltaic properties of n, n-diethylaniline based donor materials by bridging core modifications for efficient solar cells. Chemistry Select, 5(25), 7358–7369.

12. Mehboob, M. Y.,Hussain, R., Khan, M.U.,**Adnan, M**.,Umar, A., Alvi, M.U., Ahmed, M., Khalid, M., Iqbal, J., & Akhtar, M.N. (2020). Designing n-phenylaniline-triazol configured donor materials with promising optoelectronic properties for high-efficiency solar cells. Computational and Theoretical Chemistry, 112908.

13. Khan, M. U., Mehboob, M. Y., Hussain, R., Afzal, Z., Khalid, M., & **Adnan, M**. (2020). Designing spirobifullerene core based three-dimensional cross shape acceptor materials with promising photovoltaic properties for high-efficiency organic solar cells. International Journal of Quantum Chemistry, e26377.

14. Mehboob, M. Y., Khan, M. U., Hussain, R., Ayub, K., Sattar, A., Ahmad, M. K., Irshad, Z., & **Adnan, M***. (2020). Designing of benzodithiophene core-based small molecular acceptors for efficient non-fullerene organic solar cells. Spectrochimica Acta Part A: Molecular and Biomolecular Spectroscopy, 118873.

15. Siddique, S. A., Siddique, M. B. A., Hussain, R., Liu, X., Mehboob, Z., Muhammad Yasir and Irshad, & **Adnan, M***. (2020). Efficient tuning of triphenylamine-based donor materials for high-efficiency organic solar cells. Computational and Theoretical

Chemistry, 113045.

16. Younas, F., Mehboob, M. Y., Ayub, K., Hussain, R., Umar, A., Khan, M. U., Irshad, Z., & **Adnan, M***. (2020). Efficient cu decorated inorganic b12p12 nanoclusters for sensing toxic cocl2 gas: A detailed DFT study. Journal of Computational Biophysics and Chemistry.

17. Hussain, R., Yasir Mehboob, M., Usman Khan, M., Khalid, M., Irshad, Z., Fatima, R., Anwar, A., Nawab, S., & **Adnan, M***. (2020). Efficient designing of triphenylamine based hole transport materials with outstanding photovoltaic characteristics for organic solar cells. Journal of Materials Science, 1–19.

18. Bilal Ahmed Siddique, M., Hussain, R., Ali Siddique, S., Yasir Mehboob, M., Irshad, Z., Iqbal, J., & **Adnan, M***. (2020b). Designing triphenylamine-configured donor materials with promising photovoltaic properties for highly efficient organic solar cells. Chemistry Select, 5(25), 7358–7369.

**I dedicate this thesis to my family and friends who believed in me to achieve my dream.**

**Their unconditional love, constant support and grace has always kept me going.**